Deciphering the Diversified Metabolic Behavior of Hydroxyalkyl Ferrocidiphenols as Anticancer Complexes

Hui Wang, Xuejing Fan, Pei-Pei Xie, Shuang Yang, Pascal Pigeon, Ying Xiong, Susu Gai, Xin Qi, Jing Wang, Qianer Zhang, et al.

Deciphering the Diversified Metabolic Behaviour of Hydroxyalkyl Ferrocidiphenols as Anticancer Complexes

Hui Wang,[a]# Xuejing Fan,[a]# Pei-Pei Xie,[b]# Shuang Yang,[a]# Pascal Pigeon,[c,d] Ying Xiong,[e] Susu Gai,[a] Xin Qi,[a] Jing Wang,[a] Qianer Zhang,[a] Wei Li,[a] Huimei Qian,[a] Michael J. McGlinchey,[f] Gérard Jaouen,[c,d], Chao Zheng,[b]* and Yong Wang[a]*

[a] Key Laboratory of Marine Drugs, Chinese Ministry of Education; School of Medicine and Pharmacy, Ocean University of China, Qingdao 266003, Shandong, P. R. China; Laboratory for Marine Drugs and Bioproducts, Pilot National Laboratory for Marine Science and Technology, Qingdao 266200, P. R. China

E-mail: wangyong8866@ouc.edu.cn

[b] State Key Laboratory of Organometallic Chemistry, Shanghai Institute of Organic Chemistry, Chinese Academy of Sciences, 345 Lingling Lu, Shanghai 200032, P. R. China

E-mail: zhengchao@sioc.ac.cn

[c] PSL, Chimie ParisTech, 11 rue Pierre et Marie Curie, F-75005 Paris, France

[d] Sorbonne Université, UMR 8232 CNRS, IPCM, 4 place Jussieu, F-75005 Paris, France

[e] School of Pharmacy, Fudan University, Shanghai, 201203, China.

[f] UCD School of Chemistry, University College Dublin, Belfield, Dublin 4, D04 C1P1, Ireland

# These authors contributed equally.

Keywords antitumour agents; bioorganometallic chemistry; density functional theory; ferrocene; quinone methides.

Abstract: Ferrocidiphenols possessing appropriate substituents in the aliphatic chain have very promising anticancer properties, but a systematic approach to deciphering their diversified metabolic behaviour has so far been lacking. Herein we show that a series of novel ferrocidiphenols bearing different hydroxyalkyl substituents exhibit strong anticancer activity as revealed in a range of *in vitro* and *in vivo* experiments. Moreover, they display diversified oxidative transformation profiles very distinct from those of previous complexes, shown by use of chemical and enzymatic methods, *in-cellulo* and *in vivo* metabolism studies. In view of this phenomenon, unprecedented chemo-evolutionary sequences that connect all the ferrocidiphenol-related intermediates and analogues have been established. In addition, a comprehensive density functional theory (DFT) study has been performed to decipher the metabolic diversification profiles of these complexes and demonstrate the delicate modulation of carbenium ions by the ferrocenyl moiety, *via* either α- or β-positional participation.

Introduction

Platinum complexes represent one of the great successes in the area of anticancer drugs, although the emerging drug-resistance and systemic toxicity have hampered somewhat their clinical applications and efficacy. Recently a new direction in the development of metallodrugs to circumvent the drawbacks[1-6] associated with the platinum complexes, and linked to the rise of transition metal bioorganometallic chemistry, has gradually come to the fore.[7-19] Amongst the organometallic complexes that can be used as antitumoral agents, those of iron, an earth-abundant and inexpensive metal, occupy a privileged position, mostly featuring ferrocene, a compact, stable, non-toxic metallocene showing reversible redox properties.[20-29]

We have established the effective use of ferrocenes in oncology based on the so-called ferrocifen family (Fig. 1), in which a phenyl group in tamoxifen, the current first-line treatment for hormone-dependent breast cancer, has been replaced by ferrocenyl, as in **1a** and **1b**, whose IC_{50} values against triple negative breast cancer (TNBC) cell lines (MDA-MB-231) are 0.5 and 0.6 μM respectively.[30] These singular entities possess a redox motif of the [ferrocenyl-ene-phenol] type, which can not only give rise to reactive oxygen species (ROS) in cancer cells, but also lead to selective electrophilic quinone methides (QMs, see below) upon the initial reversible oxidation of the ferrocenyl antenna.[31-32] Both of these approaches enable cancer cells to suffer senescence and/or apoptosis depending on their particular parameters.[20] These antitumorals leave healthy cells quasi untouched and exhibit antiproliferative effects on a wide range of cancer cells, including some that are resistant to standard chemotherapy.[31-36]

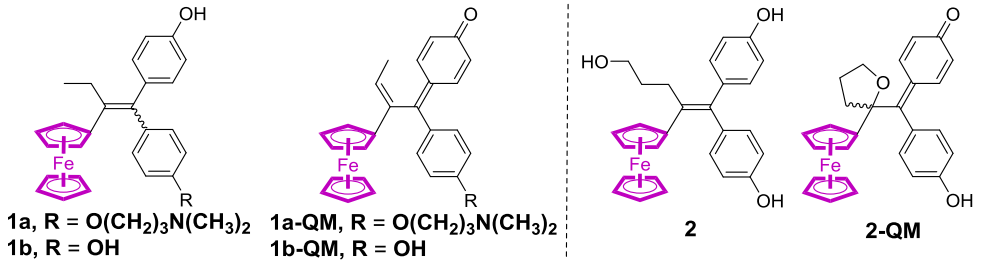

Fig. 1. Structures of selected ferrocidiphenols and their derived quinone methides.

In the particular case of the hydroxylpropyl-ferrocidiphenol, **2**, that we reported previously, it displayed particularly low IC_{50} values (0.11 and 0.30 μM respectively) on TNBC cell lines (MDA-MB-231) and cisplatin-resistant ovarian A2780*cis*R cancer cells.[37-38] Moreover, a wide diversity of reactive metabolites of **2**, via transformations of the unique

tetrahydrofuran-QM **2-QM**, have also been identified. Although the vital role of the ferrocenyl unit as both an intramolecular reversible redox ″antenna‟ and stabilized carbenium ion ″modulator‟ has been proposed by us previously, the theoretical underpinnings to rationalize such a wide range of behaviour have yet to be explored. This prompted us to probe the effect of the length of the alkyl chain on the metabolism and the antitumor activity of ferrocidiphenols, and we here report the behaviour of the hydroxyethyl-, hydroxybutyl- and hydroxypentyl-ferrocidiphenols, **3, 4** and **5,** respectively (Scheme 1), exhibiting strong antiproliferative activity evidenced by a range of *in vitro* and *in vivo* experiments. More interestingly, these complexes, in which the length of the hydroxyalkyl chain has been modified, displayed diversified oxidative metabolic behaviour very distinct from that of their hydroxypropyl counterpart, **2**, as evidenced from chemical, liver microsomal, *in-cellulo* and *in vivo* metabolism studies. Furthermore, benefitting from the chemo-selective annulation of the terminal hydroxyl with a variety of carbenium ions at positions α-, β1-, or β2- relative to the ferrocenyl group, a proof-of-concept density functional theory (DFT) study has been carried out to decipher the metabolic diversification profiles of these complexes, and also to demonstrate the subtle modulation of carbenium ions by a neighbouring ferrocenyl unit. This work consummates our mechanistic understanding of the ferrocifen family and enables us to propose a comprehensive chemo-evolutionary sequence mediated by the versatile ferrocenyl group.

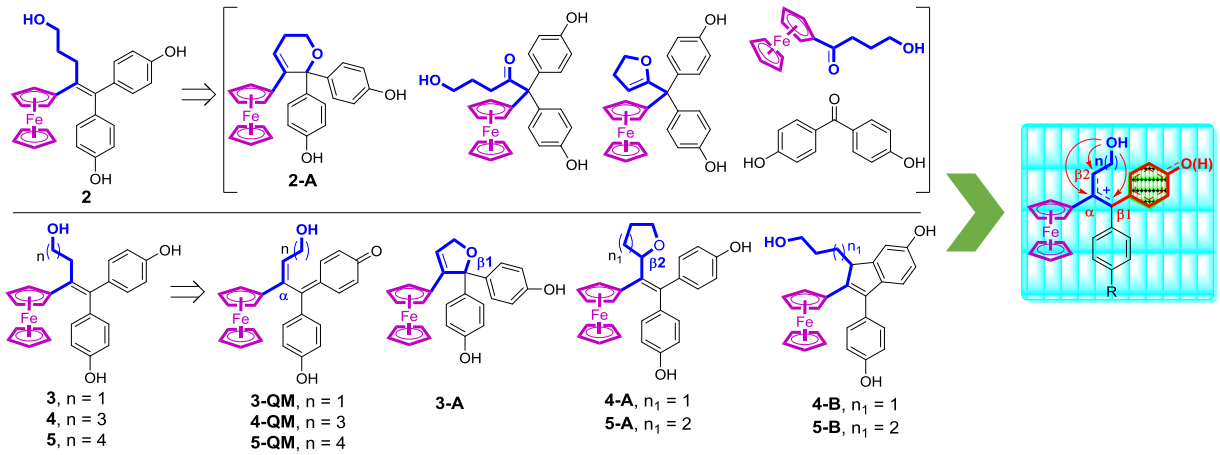

Scheme 1. Illustration of the diversified metabolic behaviour of a series of hydroxyalkyl ferrocidiphenol anticancer complexes.

Results and Discussion

Chemical Transformations of Ferrocidiphenols

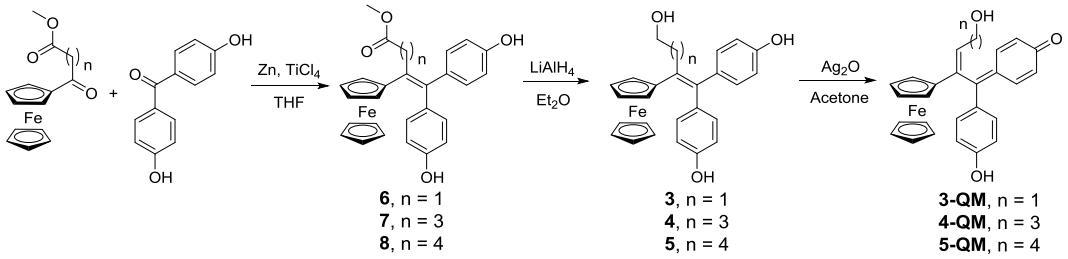

Scheme 2. Syntheses of the ferrocenyl compounds **3-5**, and of their corresponding QMs.

Efficient syntheses of the designed hydroxyalkyl ferrocidiphenols **3** - **5** proceeded via a McMurry coupling of the appropriate ferrocenyl keto-ester with 4,4´-dihydroxy-benzophenone, followed by $LiAlH_4$ reduction of the esters **6** – **8** (Scheme 2). It is interesting to note that an unexpected cyclohexanone major byproduct, **9**, was obtained in the synthesis of the propyl ester **7** (Scheme S1). To monitor the oxidative behaviour of these complexes, Ag_2O/acetone-*d6* was used initially as the oxidant system, and it was gratifying to find that these complexes yielded diverse final products depending on the length of the alkyl chain. In the case of the hydroxyethyl complex **3**, bearing only a two-carbon alkyl chain, oxidation with four equivalents of Ag_2O led almost quantitatively in 30 mins to the novel 2,5-dihydrofuran derivative **3-A**, whose X-ray crystal structure is shown in Fig. 2. A trace amount of **(*Z*)-3-QM** was detected by NMR, even after two hours (Fig. S3), and one can speculate that, if the carbons and their attached groups at positions α, β1 and β2 maintain coplanarity in the allyl cation intermediate, then ring closure of the hydroxyethyl chain to form the dihydrofuran **3-A** would be favoured starting from **(*E*)-3-QM**, thus causing its more rapid disappearance.

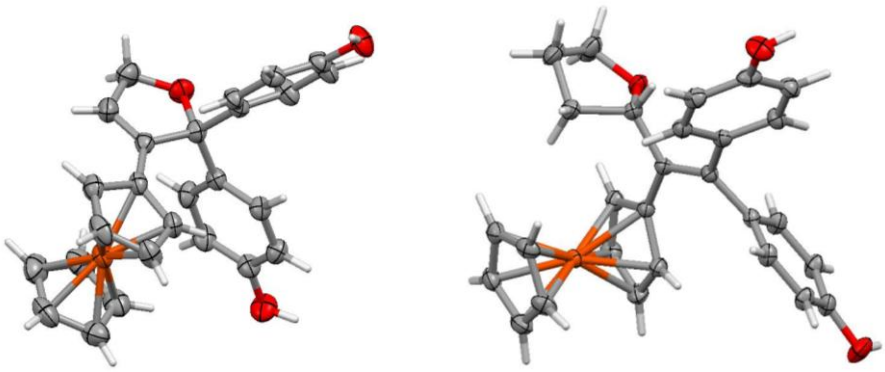

3-A **4-A**

Fig. 2. Molecular structures of the dihydrofuran **3-A** (left), and of the tetrahydrofuran **4-A** (right), with thermal ellipsoids shown at 50% probability.

In contrast, the oxidation of ferrocidiphenols **4** and **5** with the longer alkyl chains proceeded slightly more slowly than that of **2** or **3** (Table 1) and exhibited entirely different

behaviour when oxidized with Ag_2O. NMR spectroscopic (Fig. S4) and X-ray crystallographic data (Fig. 2) confirmed the identity of the tetrahydrofuran-substituted ferrocidiphenol, **4-A**, as the final product in the gradual evolution of the hydroxybutyl precursor **4**. It is evident from monitoring the course of the reaction by NMR that this transformation begins with the formation of **4-QM** which, over a period of many hours, gradually undergoes intramolecular cyclization to generate a five-membered ring at position β2 relative to the ferrocenyl fragment. Turning now to the hydroxypentyl-ferrocidiphenol, **5**, possessing the longest alkyl chain in this series, oxidation led first to the acyclic **5-QM**; however, we note that **5-QM** is more stable than **4-QM**, and the two final products are formed only when left in acetone-*d6* for more than a week (see Fig. S5). After subsequent isolation and separation, the first product was identified as the **5-A** (the ring-enlarged analogue of **4-A**) whereby cyclization of the hydroxylpentyl chain yielded a tetrahydropyran ring, and the second as **5-B**, in which acid-catalyzed cyclization of **5-QM** brought about indene formation, a phenomenon we have discussed previously.[38] One might venture to suggest that, although the formation of **5-A** is obviously faster than that of **5-B**, the yields of these complexes are ultimately approximately the same, **5-A** may be the kinetically favoured product, and **5-B** may be the result of thermodynamic control.

Electrochemical (Cyclic Voltammetry) Studies

The conversion of a precursor ferrocidiphenol to a quinone methide requires the overall loss of two hydrogens (as two electrons and two protons) and, as shown in an earlier cyclic voltammetry/EPR study, this proceeds in a stepwise manner (Scheme S2).[39] The electrochemical profiles of the new compounds have now also been investigated in acetonitrile using $[Bu_4N]BF_4$ as the supporting electrolyte, and their cyclic voltammograms are shown in Fig. 3. In each case, compounds **2 - 5** gave rise to an oxidation process for the $Cp_2Fe^{0/+}$ couple and a more positive irreversible phenol oxidation wave, as already established for other ferrocidiphenols. In the absence of imidazole, compounds **2** and **3** with their hydroxypropyl and hydroxyethyl chains exhibit reversible mono-electronic oxidations, at 0.48 V and 0.50 V respectively, ascribed to ferrocenyl oxidation. However, under the same conditions it was found that the ferrocene oxidation waves of the longer chain complexes **4** and **5** were less reversible than those of **2** and **3**. This suggests that the longer and more flexible hydroxyalkyl chains of **4** and **5** may be involved in the deprotonation of the phenol after the initial oxidation, with subsequent somewhat reduced capacity for intramolecular electron transfer between the latter and the electrochemically generated ferrocenium cation

through the π-conjugated system. Nevertheless, upon addition of five equivalents of base, they showed very similar irreversible electrochemical behaviour to that previously reported, whereupon base-promoted intramolecular electron transfer between the phenol and the ferrocenium cation gave a quinone methide.[39]

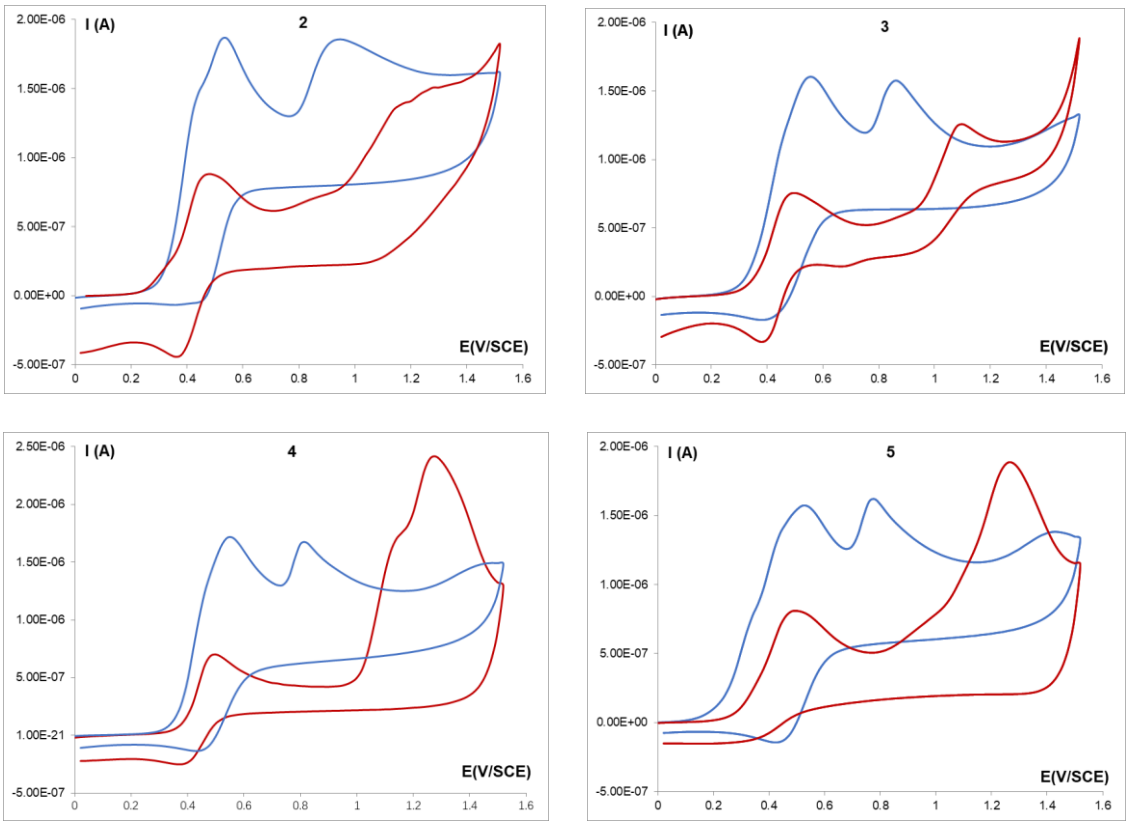

Fig. 3. Cyclic voltammograms of **2** through **5** (approximately 1 mM, scan rate 200 mV/s) in the absence of base (red curve) and in the presence of 20 mM imidazole (blue curve).

In Vitro Metabolism Studies of Ferrocidiphenols

Ferrocidiphenols can be considered as prodrugs that give rise to their corresponding quinone methides which may covalently react with proteins, such as thioredoxin reductase (TrxR) which, as we have discussed previously, is part of the cell's defense mechanism against ROS.[35-36] Thus the *in vitro* metabolic transformation of ferrocidiphenols to QMs is the basis for their efficacy and an important component of their drug-like properties. A preliminary *in vitro* metabolic stability assessment of the ferrocidiphenols **2** through **5** was conducted, and selected data are shown in Table 1 and in Fig. S6. These compounds had relatively desirable metabolic stabilities in both human and rat plasma with a half-life more than 5 hours. However, incubation of **2** - **5** with rat liver microsomes in the presence of nicotinamide adenine dinucleotide phosphate (NADPH), the reducing agent necessary for the activity of microsomal monooxygenases, revealed that these compounds can be completely

cleaved in few minutes, even faster than their oxidation by Ag_2O. Likewise, incubation with human liver microsomes under identical conditions led to very similar results, indicating that liver microsomes are responsible for their oxidative transformation to QMs.

Table 1. Stability of ferrocidiphenols **2~5** under oxidative condition and the resulted metabolites by incubation with liver microsomes.

Compounds	$t_{1/2}$ (min) [a] Ag_2O	$t_{1/2}$ (min) [b] LM	**QM** [c]	**A** [c]	**B** [c]
2	3.0	0.9	trace	+	trace
3	1.7	1.4	+	++++	trace
4	4.3	1.3	trace	++++	++
5	4.4	2.1	trace	++++	++

(a) In acetone-d_6, in the presence of freshly prepared Ag_2O. (b) Incubation of compounds (2 μM) with rat liver microsomes (LM, 0.8645 nmol P450/mg protein, 0.2 mg protein/mL) in the presence of NADPH. (c) Semiquantitative analysis method was used to determine the extent of product formation according to their HPLC or LC-MS spectra: trace, < 1%; +, 1% ~ 10%; ++, 10% ~ 40%; ++++, >40%; **QM**: quinone methides of the corresponding compounds are shown in Scheme 1; **A**: the cyclic ether products of the corresponding compounds are shown in Scheme 1; **B**: the indene products of the corresponding compounds are shown in Scheme 1.

Subsequently, we carried out an *in vitro* metabolic transformation analysis of ferrocidiphenols **3** - **5**, which collated information on all the products observed upon treatment with chemical oxidants; other minor metabolites produced in very small quantities are not discussed here. All products were unambiguously characterized by comparison of their HPLC retention times, and their MS and MS/MS characteristics, with those of authentic samples obtained by chemical synthesis. None of these metabolites were observed when incubations were carried out under identical conditions, but without NADPH. In the case of the hydroxyethyl-ferrocidiphenol, **3**, the dihydrofuran, **3-A**, was observed as the major product and represented more than 40% of all metabolites, but **3-QM** was still detectable in very low quantities (Fig. S7). For its hydroxybutyl- and hydroxypentyl- counterparts, **4** and **5**, respectively, the products found were the indenes **4-B** and **5-B** and the cyclic ethers (tetrahydrofuran **4-A** and tetrahydropyran **5-A**); the proportion of the latter compounds varied from 60% to 80% relative to all metabolites (Fig. S8-9). These results were slightly different from those observed upon oxidation by Ag_2O which engendered almost full conversion of **4-QM** to tetrahydrofuran **4-A**.

To mimic the physiological liver environment [40] and to generate a realistic metabolic fingerprint of **3** and **4**, incubation with rat hepatocytes revealed that approximately 19% of **3** and 49% of **4** remained after 3 h (Fig S10-11), thus verifying the feasible metabolism of **3** and **4** as prodrugs. Furthermore, their biotransformations in rat hepatocytes were in accord with the results of enzymatic incubation discussed above, yielding **3-A** and **4-A**, respectively, as the major products. Intriguingly, a putative Phase II metabolite has been observed in the case of **3**, which refers to the glucuronide conjugates of **3-A** (M613, Fig S10). Both the enzymatic and the cell-based metabolites detection and characterization reported here afford comprehensive data for the prediction of *in vivo* metabolites of ferrocidiphenols.

In Vivo Metabolism Studies of Ferrocidiphenols

Furthermore, the *in vivo* metabolic transformations of **2** and **3** have been performed to explore the mammalian oxidative behavior of ferrocidiphenols. The plausible metabolic pathways and relative MS abundances of the metabolites found, in terms of UHPLC-MS, have been presented in Fig. S12-13. From the analysis of plasma, faeces and urine samples after treatment with **2** and **3**, a variety of metabolites have been identified including both Phase I and Phase II biotransformation. The primary bioactivation pathway of **2** and **3** involves oxidation of ferrocidiphenols to the corresponding dehydrogenated products which refers to the QM pathway mentioned above. Subsequently, the electrophilic dehydrogenated metabolites can be conjugated with cysteine and glucuronide to give Phase II conjugates. These results can be rationalized in terms of the previous enzymatic and the cell-based metabolism studies. To the best of our knowledge, this is the first comprehensive study to investigate the in *vivo* metabolic profiles of ferrocidiphenols.

Table 2. Pharmacokinetic parameters of **2** *in vivo*.

PK parameters	Values
Dose (mg/kg)	30
$t_{1/2}$ (h)	4.73 ± 0.13
C_{max} (ng/mL)	10819 ± 1887
AUC_{0-t} (h*ng/mL)	11197 ± 263
MRT_{0-t} (h)	3.27 ± 0.65
Cl (mL/min/kg)	44.1 ± 0.98

(a) $t_{1/2}$, half-life; C_{max}, maximum concentration detected after intravenous dose; AUC, area under the concentration curve; MRT, mean residence time; Cl, clearance.

To explore the drug-like properties of hydroxyalkyl-ferrocidiphenols, the *in vivo* pharmacokinetic profiles of **2** have been investigated and the results are presented in Table 2. A moderate pharmacokinetic parameter was observed in the case of **2** with the terminal half-life time of 4.7 h, the area under the concentration-time curve (AUC_{0-t}) of 11197 h*ng/mL and the plasma clearance rate (Cl) of 44.1 mL/min/kg. These results revealed that ferrocidiphenols possess acceptable pharmacokinetic behavior for antitumor evaluation *in vivo*.

In Vitro Anticancer Evaluations

Table 3. IC_{50} values for selected ferrocenyl compounds towards MDA-MB-231 cells.

Compounds	IC_{50} (μM) [a]	logPo/w	Compounds	IC_{50} (μM) [a]
2	0.11 ± 0.02 [b]	4.2 [b]	**8**	1.1 ± 0.02
3	0.20 ± 0.08	4.4	**3-A**	9.98 ± 0.19
4	0.25 ± 0.04	4.5	**4-A**	0.70 ± 0.08
5	0.35 ± 0.05	4.8	**5-A**	1.11 ± 0.13
6	0.39 ± 0.07	4.5	**5-B**	4.62 ± 0.32
7	0.22 ± 0.03	--	**4-OH TAM**	> 30

(a) Measured in 24-well plates after 5 days of culture (mean of three independent experiments ± SD); (b) Values taken from ref. 35.

In this laboratory, preliminary in-house antiproliferative activities against triple negative breast cancer MDA-MB-231 cells have been routinely used to evaluate the anticancer activity of our molecules, such as for the ferrocidiphenols **2 - 8**, and for the products formed after oxidation (as shown in Table 3). The hydroxyethyl, **3**, hydroxybutyl, **4**, and hydroxypentyl, **5**, complexes exhibited similar antiproliferative activity with IC_{50} values ranging from 200 to 350 nM, and are noticeably less active than the hydroxypropyl derivative **2** (IC_{50} of 110 nM). Interestingly, these three complexes exhibited slightly higher lipophilicity whether upon chain-shortening, as in **3**, or by chain-lengthening as in **4** and **5**. Amongst the major products obtained upon chemical oxidation and their subsequent transformation, the cyclic ethers **4-A** and **5-A** exhibited better antiproliferative activity at the submicromolar level, probably attributable to the retention of the [ferrocenyl-ene-phenol] redox motif. By way of contrast, formation of the 2,5-dihydrofuran or indene rings, as in **3-A** or **5-B** respectively, resulted in a significant loss of cytotoxicity. In all cases noted above, these data are in sharp contrast with the greater activity and lower IC_{50} values of their precursor diphenols **3 - 5**. This emphasizes the aggressive role of the transient intermediate metabolites appearing during the oxidative

process, i.e. the quinone methides and the variety of carbonium cations. Evidently, one must take into account the fact that these species are being formed inside the cell, close to important cell targets, upon oxidation of their precursor ferrocidiphenols.[34] It is particularly noteworthy that the tamoxifen derivative **4-OH TAM** as a reference compound shows only limited cytotoxicity (IC_{50} > 30 μM); in light of the slower rate of oxidation of tamoxifen derivatives to give QMs mentioned earlier, this result underlines the importance of the transformation into QMs in terms of cytotoxicity on MDA-MB-231 cells.

Inspired by the above results, the cytotoxicity effects of **2**-**5** were further evaluated on other tumor cells including the TNBC cancer (4T1), the ER+ cell line (MCF-7), colorectal cancer (HCT116), leukemia (K562), melanoma (A-375), as well as the ferroptosis-sensitive fibrosarcoma (HT1080). As shown in Table 4, the hydroxypropyl- and hydroxyethyl-ferrocidiphenols, **2** and **3,** are the most active overall, displaying strong anticancer activity on all the tested cancer cells except HT1080. A decrease in the cytotoxic activity was observed in the case of the hydroxybutyl (**4**) and hydroxypentyl (**5**) derivatives on multiple cancer cells except 4T1. On the other hand, compounds **2** and **3** display weaker cytotoxicity on human normal breast cells of MCF-10A (IC_{50} > 30 μM) compared to that of **4** and **5**, and they are all less toxic than doxorubicin on MCF-10A with a selectivity factor > 150. This indicative criterion suggests them as good candidates for drug development.

Table 4. Table 4. IC_{50} (μM)[a] of selected molecules on other cell lines: TNBC cancer (4T1), ER+ cancer (MCF-7), colorectal cancer (HCT116), melanoma (A-375), leukemia (K562), fibrosarcoma (HT1080) and normal breast cells (MCF-10A).

Comps.	4T1	MCF-7	HCT 116	K-562	A-375	HT1080	MCF-10A
2	0.12 ± 0.03	0.44 ± 0.03	1.21±0.25 [b]	1.99 ± 0.52 [b]	NT	9.54 ± 0.05	> 30
3	0.15 ± 0.02	1.27 ± 0.29	0.67 ± 0.16	1.50 ± 0.19	0.19 ± 0.01	12.13 ± 0.21	> 30
4	0.10 ± 0.03	12.53 ± 0.28	> 20	1.44 ± 0.63	13.7 ± 0.04	NT	27.30 ± 0.50
5	0.17 ± 0.04	10.75 ± 0.26	10.29 ± 0.17	3.67 ± 0.33	8.51 ± 0.10	NT	26.83 ± 0.55
DXR[c]	0.25 ± 0.17	0.54 ± 0.04	0.53 ± 0.01	0.90 ± 0.01	0.16 ± 0.02	NT	0.15±0.02

(a) Measured in 96-well plates after 48 h of culture (mean of three independent experiments ± SD); (b) Values taken from ref. 33; (b) NT: Not Tested; (c) DXR: doxorubicin

Cell Migration and Invasion Studies

Tumor progression involves sequential steps, such as the coordination of cell proliferation, adhesion, migration and invasion. Firstly, the blocking of cell proliferation by ferrocidiphenols **2**, **3**, **4** was investigated by the colony-formation assay, which showed that those compounds dramatically reduced the colony numbers of MDA-MB-231 cells in a dose-dependent manner (Fig. 4A). Furthermore, the effect of **2**, **3**, **4** on the migration and invasion of cancer cells was also examined. Through a wound-healing assay, it was found that those compounds significantly attenuated the migration of MDA-MB-231 cells time-dependently, especially in the case of **2** (Fig. 4B). Similarly, transwell assays revealed that those molecules could decrease the invasion of tumor cells dose-dependently (Fig. 4C, S14-16). These observations indicated the high capacity of **2**, **3**, **4** to inhibit the migratory and invasive properties of MDA-MB-231 cells, suggesting their potential importance for the treatment of refractory cancer metastasis, considering that TNBC MDA-MB-231 cells have high invasiveness, and approximately half of TNBC patients will have distant metastasis.[41]

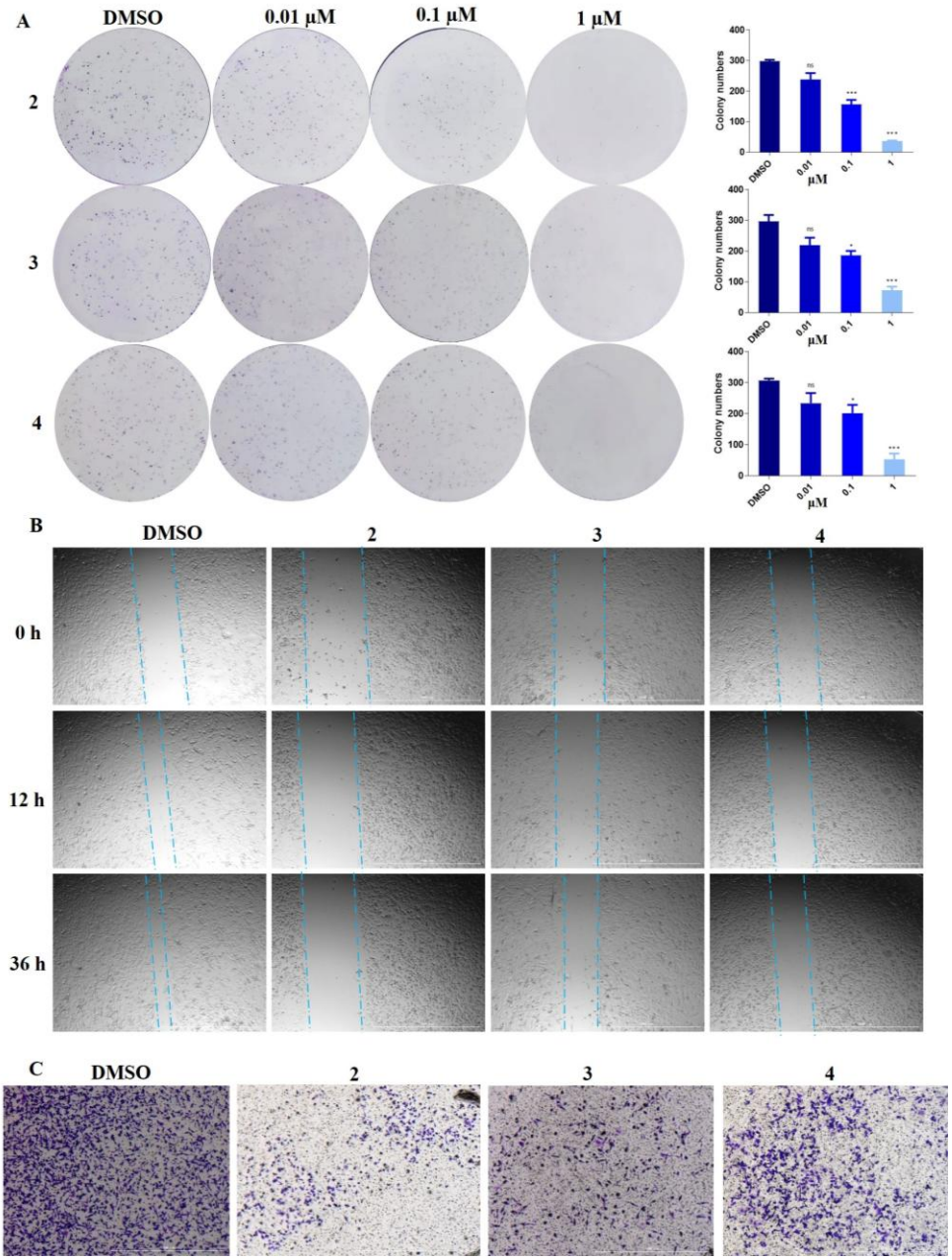

Fig. 4. A) Colony-formation assays were conducted in MDA-MB-231 cells. The colony numbers were counted by ImageJ. B) Wound-healing assays were used to detect the migration of MDA-MB-231 cells after treatment of **2**, **3**, **4** (2 μM). C) Transwell assays were used to detect the invasion of cancer cells after treatment of corresponding compounds (2 μM).

Cell Cycle Analysis and Apoptosis

The effect of the compounds on the cell cycle of MDA-MB-231 cells was further studied by flow cytometry. All three compounds (**2**, **3**, **4**) could arrest the cell progression mainly in the synthesis phase (phase S), for instance, upon treatment with 2 μM of ferrocidiphenols, the cells population in the phase S increased from 12.61% to around 30%

(Figure 5A). Moreover, it was evident that these compounds led in a dose-dependent fashion to an increase in the number of cells of phase S (Fig. S17-19). The action of **3** on the phase S arrest is slightly weaker than that of **2** and **4**.

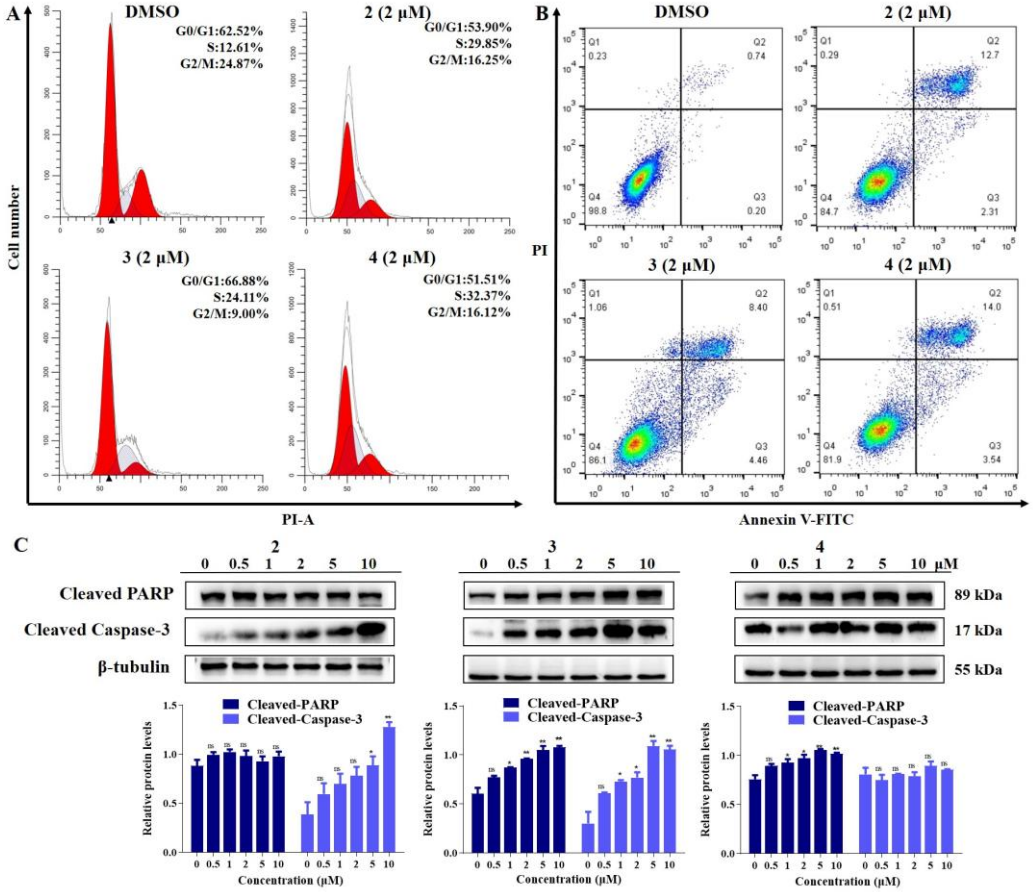

Fig. 5. A) Cell cycle changes of MDA-MB-231 cells after incubation with **2**, **3**, **4** (2 μM) for 24 h, and B) Flow cytometry analysis of MDA-MB-231 cells after incubation with **2**, **3**, **4** (2 μM) for 24 h; C) western blot analysis of cleaved-PARP and cleaved-caspase 3 levels in MDA-MB-231 cells following treatment of corresponding compounds.

The mode of cell death was investigated using the annexin V-FITC/propidium iodide (PI) double staining assay. As shown in Figure 5B, generally, ferrocidiphenols **2**, **3**, **4** induced MDA-MB-231 cells to enter late apoptosis significantly at **2** μM, thus confirming their proapoptotic ability. A dose-dependent effect of these compounds was confirmed inducing late-stage apoptosis (Fig. S20-22). Likewise, the detectable concentration to induce proapoptotic cell death can be decreased to nanomolar level on 4T1 cancer cells in the cases of **2** and **4** (Fig. S23). Subsequently, western blot studies were performed to detect the levels of key proteins involved in the apoptosis pathway affected by those compounds. Apparently, the cleavage of PARP and caspase-3 significantly increased in cells dose-dependently, providing evidence for the apoptotic response induced by ferrocidiphenol **3**.

ROS Related Bioactivity Evaluation

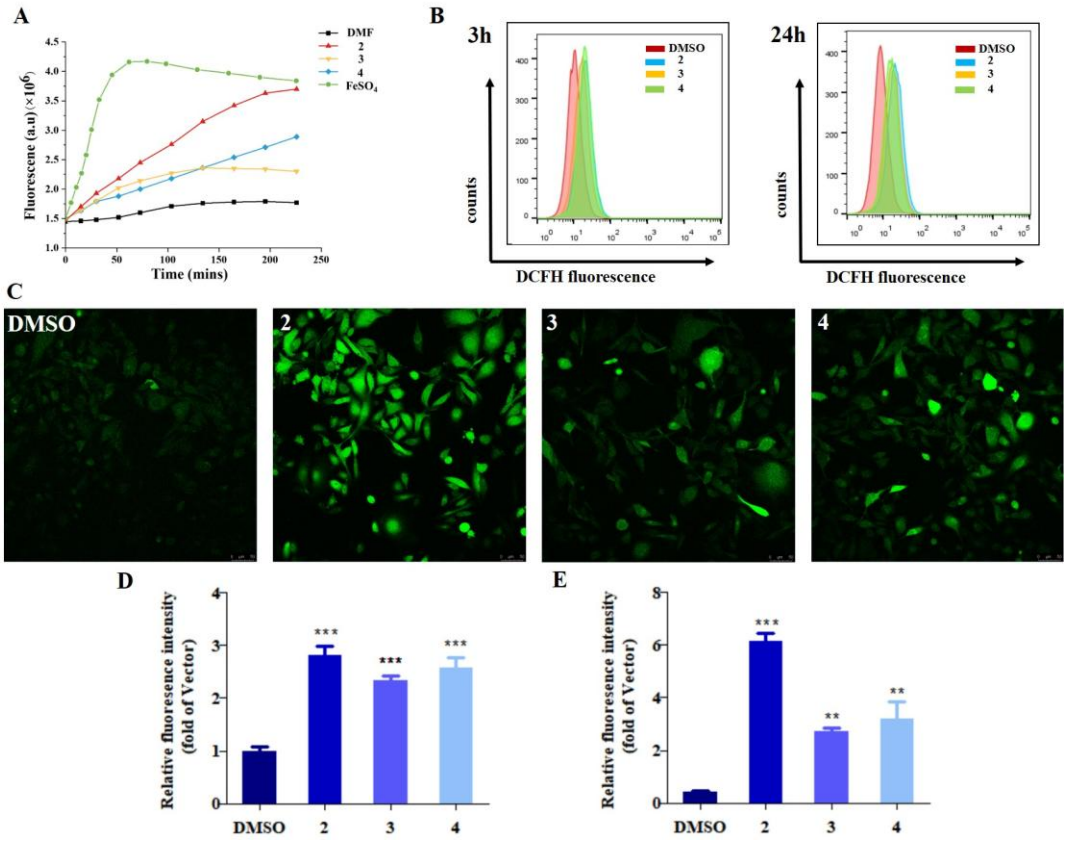

Fig. 6. A) Monitoring of the generation of ROS of corresponding compounds (100 μM) using fluorescence spectroscopy in combination with ROS-sensitive DCFH-DA (λ_{ex} =501 nm, λ_{em} =531 nm); B) Flow cytometry and C) representative confocal images of MDA-MB-231 cells after incubation with **2**, **3**, **4** (2 μM) and DCFH-DA; D) Flow cytometry data analysis and E) confocal analysis of MDA-MB-231 cells after incubation with **2**, **3**, **4** (2 μM) and DCFH-DA.

It is known that the formation of ROS, via a Fenton type reaction, plays an important role in the cytotoxicity of ferrocidiphenols. Therefore, the ability of ferrocidiphenols **2**, **3**, **4** to induce ROS formation was evaluated in physiological conditions by the widely used fluorescent ROS indicator, 2′,7′-dichlorofluorescin diacetate (DCFH-DA). As shown in Fig. 6A, a known H_2O_2-induced activation method was first used to monitor ROS generation by ferrocidiphenols in buffer.[42] All these compounds can induce the ROS generation in a time-dependent manner**,** and **2** produced much more ROS relative to **3** and **4**. To explore the relationship of ROS-inducing ability and the cell toxicity, the intracellular ROS level was measured by flow cytometry and confocal microscopy on MDA-MB-231 cells (Fig. 6B-E). According to the flow cytometry analysis, these three compounds produced significant quantities of ROS and reached a plateau phase in a short incubation time (3 h). Consistent with the ROS-producing result in buffer, the hydroxypropyl-ferrocidiphenol **2** significantly yielded a higher level of ROS in cancer cells than did of **3** and **4**. It is noteworthy that

complex **4** was observed to have the best ROS inducing ability on 4T1 cells (Fig. S24-25). This phenomenon is in complete accord with their antiproliferative activities on MDA-MB-231 and 4T1 cells, which highlighted the importance of ROS in the mechanism of action of ferrocidiphenols. Meanwhile, this is also the first time that the production of ROS by ferrocidiphenols has been measured and displayed so significantly, compared to previous reports whereby only small amounts of ROS were generated by several other ferrocidiphenols.[34, 43]

Ferroptosis is an iron-dependent form of programmed cell death whose most significant features are the accumulation of ROS and lipid peroxidation products (LPO)[44]. Considering the importance of ROS in the cytotoxicity of ferrocidiphenols, it is rational to envision the potential relationship of ferrocidiphenols and ferroptosis. Thus, the ferroptosis-inducing activities were determined on ferroptosis-sensitive HT1080 cells with or without ferrostatin-1 (fer-1), which is a specific ferroptosis inhibitor[44-45]. Primary screening was carried out for **2** and **3** at two concentrations (1 and 10 μM, see Fig. S26) as only these two compounds showed moderate anticancer activities against HT1080. Unfortunately, although **2** and **3** inhibit the proliferation of HT1080 cells at the micromolar level, these cell toxicities cannot be reversed significantly by the ferroptosis inhibitor fer-1. These results demonstrated that the anticancer effect of ferrocidiphenols may not be relevant to ferroptosis, probably the ROS formation induced by ferrocidiphenols does not occur in a lipid environment. These results correspond well to the apoptosis-type cell death we advanced earlier.

Antitumor Efficacy of 2 and 3 in 4T1 mouse Models in Vivo

Considering the outstanding activities of **2** and **3** on these two TNBC cell lines (MDA-MB-231 and 4T1), they were further assessed for their *in vivo* antitumor efficacy in a mouse 4T1 syngeneic murine model. As seen in Figure 7, both **2** and **3** exhibited significant antitumor activity *in vivo*. The tumor growth inhibition (TGI) values of **2**-treated groups were 56.1%@30 mg/kg and 64.7%@60 mg/kg, which showed that ferrocidiphenol **2** suppressed the progression of the 4T1 tumor with slight dose-dependent effect. In contrast, the hydroxyethyl compound **3** could produce typical dose-dependent suppression with TGI of 42.8 and 72.5% at 30 and 60 mg/kg, respectively. It is noteworthy that **3** displayed stronger tumor inhibition than that of **2** in the same case of delivering a high dose of drugs. Additionally, there was a slight decrease in body weight of the ferrocidiphenols treatment groups compared with the control group. Furthermore, hematoxylin and eosin (H&E) staining analysis of the major organs were investigated to evaluate the safety profile of **2** and **3**, which

demonstrated that there was no obvious toxic damage observed in major organs such as the heart, liver, spleen, lung, and kidney. These results emphasized the superior potential of ferrocidiphenols as anticancer drugs candidates for further cancer treatment.

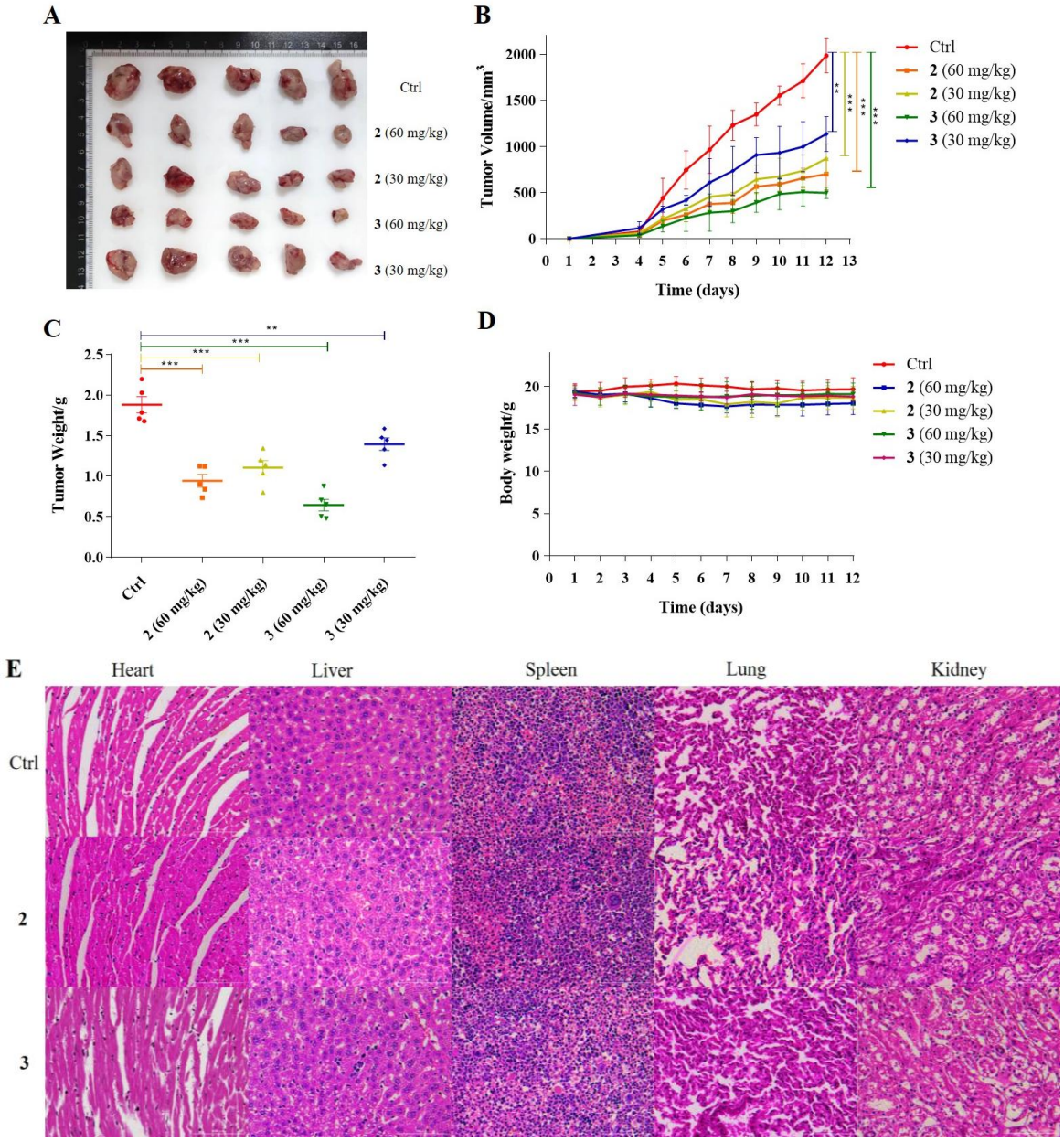

Fig. 7. *In vivo* antitumor activity of **2** and **3** in a mouse 4T1 breast carcinoma model. A) Picture of excised tumors from the different groups; B) Tumor volume curves during the treatment period; C) Tumor weights after treatment; D) Body weight curves of different groups; E) H&E staining of the major organs of mice after treatment with compounds (60 mg/kg).

DFT Calculations

Initially, DFT calculations were performed to shed light on the electronic structures of α- and β-ferrocenyl carbocations. Taking for example the case of the hydroxyethyl derivative,

where n = 1, (as shown in Scheme 1) analysis of the localized molecular orbital in the α-ferrocenyl QM cation depicted in Fig. 8a, revealed the interaction between the occupied *d* orbital of the Fe centre and the empty *p* orbital of the carbocationic centre. Likewise, protonation of the hydroxyalkenyl QM to form the β-ferrocenyl cation shown in Fig. 7b also revealed an orbital interaction between the iron and the central carbon of the allyl unit. Furthermore, the electrostatic potential diagrams confirmed the stabilization of the quinone and/or phenol rings adjacent to the carbocations.

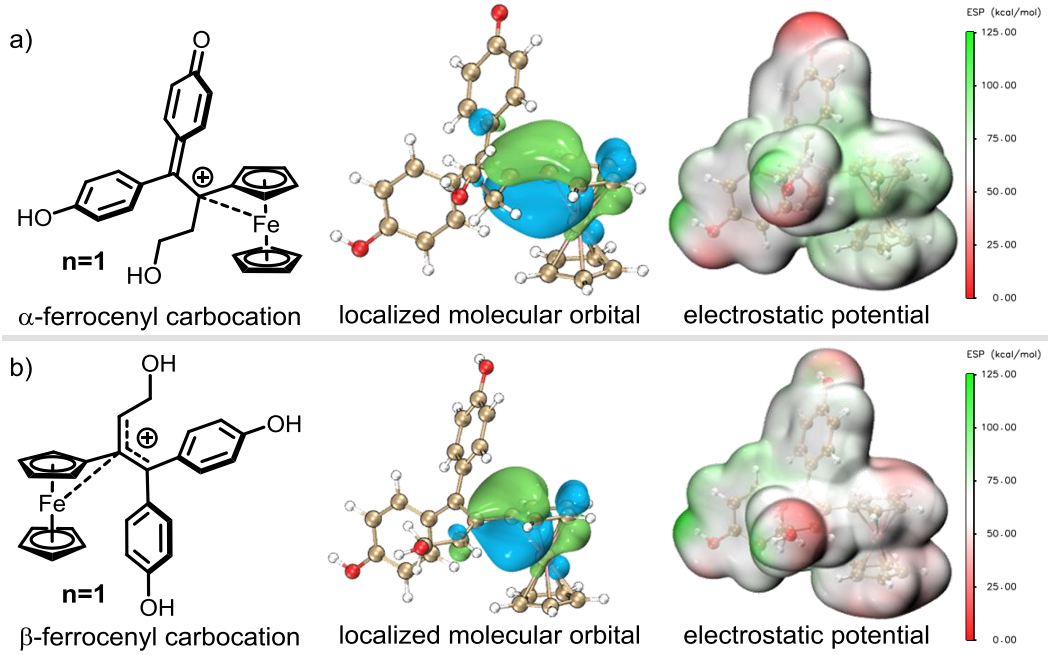

Fig. 8. DFT-computed localized molecular orbitals and electrostatic potentials for (a) the α-ferrocenyl QM carbocation and (b) β-ferrocenyl carbocation of the diphenol (n = 1).

Next, the competing reaction pathways of the ferrocidiphenols derivatives bearing a terminal hydroxy group with different chain lengths were considered. As shown in Fig. 9, for cases where n = 1, 3 and 4, the initial oxidation and deprotonation generate the corresponding hydroxyalkenyl-QM intermediates **Int1** (0.0 kcal/mol, set as the zero-points for the calculations). The protonation of such intermediates readily occurs and is highly exergonic, leading to the π-allyl cationic species **Int2** (–17.2 to –16.5 kcal/mol). The patterns of intramolecular cyclization depend on the chain lengths. The β1-etherification proceeds *via* **TS1** (–8.4 kcal/mol) for a short chain (n = 1), which delivers the dihydrofuran product **Pro1** (–16.8 kcal/mol) predominantly. In contrast, β2-etherification becomes the preferential pathway *via* **TS2** (–2.7 to –1.5 kcal/mol) for n = 3 and 4, generating the corresponding

tetrahydrofuran- or tetrahydropyran-derivatives **Pro2** (–13.3 to –10.1 kcal/mol), rather than forming seven- or eight-membered rings, respectively.

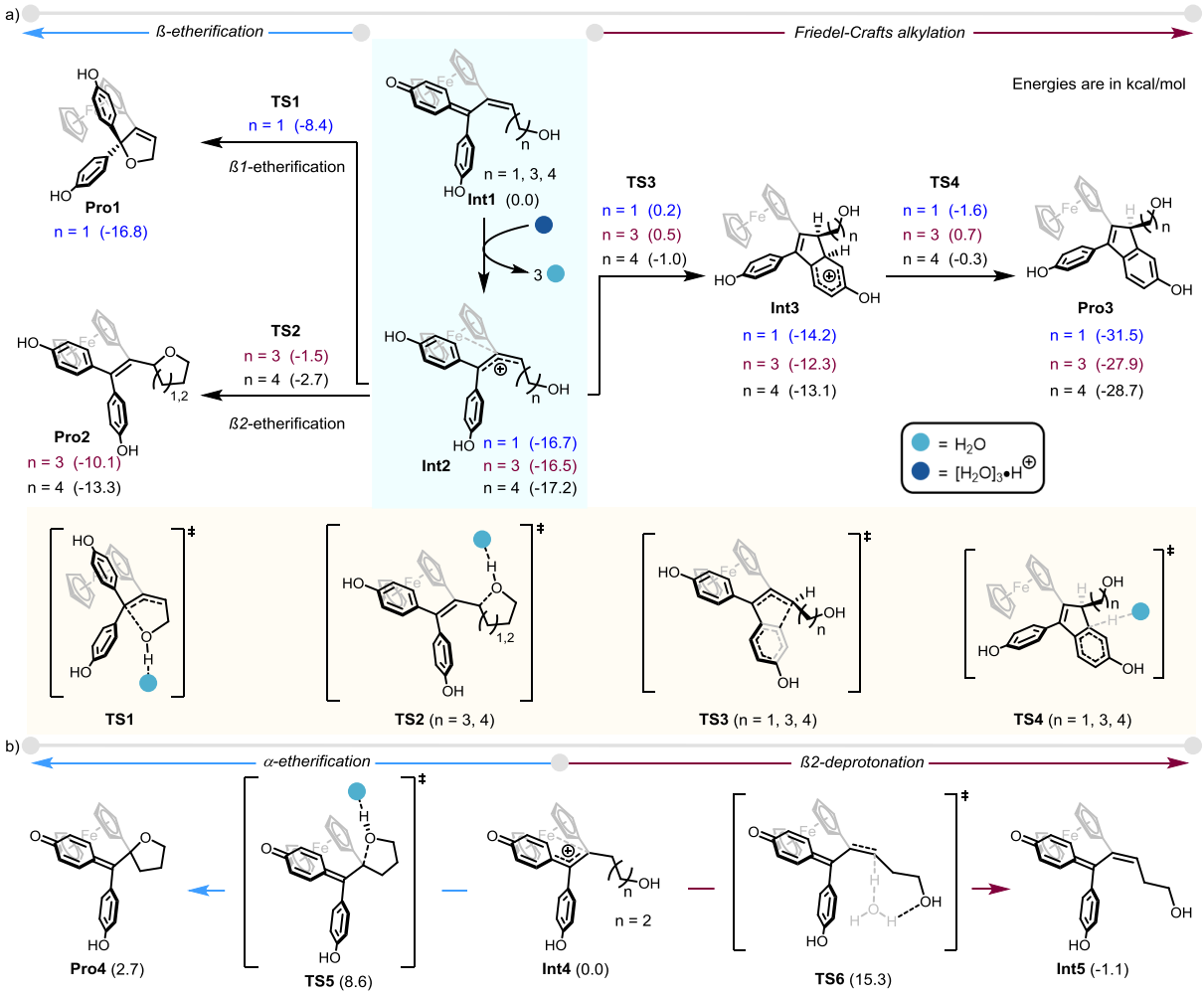

Fig. 9. DFT-computed competing reaction pathways of the ferrocidiphenols derivatives bearing a terminal hydroxy group with different chain lengths (n = 1–4). a) The reaction leading to π-allyl cationic species and subsequent competing etherification and Friedel–Crafts alkylation. b) Competition between α-etherification and β2-deprotonation. Computations were carried out at the M06-2X/def2-TZVP-SMD (acetone)//M06-2X/def2-SVP level of theory. Values are relative Gibbs free energies in kcal/mol.

We note that, in all cases where n = 1, 3 and 4, the intramolecular Friedel–Crafts-type cyclization co-exists as a kinetically less favoured pathway (*via* **TS3**, **Int3** and **TS4**, –1.6 to 0.7 kcal/mol), but the final indene products, **Pro3**, are thermodynamically more stable (–31.5 to –27.9 kcal/mol). The situation is entirely different for the hydroxypropyl case, where n = 2. The α-etherification from **Int4** (0.0 kcal/mol, set as the zero-point for the calculations) is much more facile (**TS5**, 8.6 kcal/mol) compared with the deprotonation to form quinone

methide **Int5** (–1.1 kcal/mol) *via* **TS6** (15.3 kcal/mol). Therefore, tetrahydrofuran-derivative **Pro4** (2.7 kcal/mol) is the major product in this case.

Although the vital role of ferrocene in the oxidative transformation of ferrocidiphenols has been proposed for a long time,[30] a systematic approach to rationalize this phenomenon is yet to be explored. Inspired by the remarkable profile of metabolic oxidation of hydroxyalkyl ferrocidiphenols, we venture to propose the chemo-evolutionary sequences to connect all the intermediates and observed products (Scheme 3).

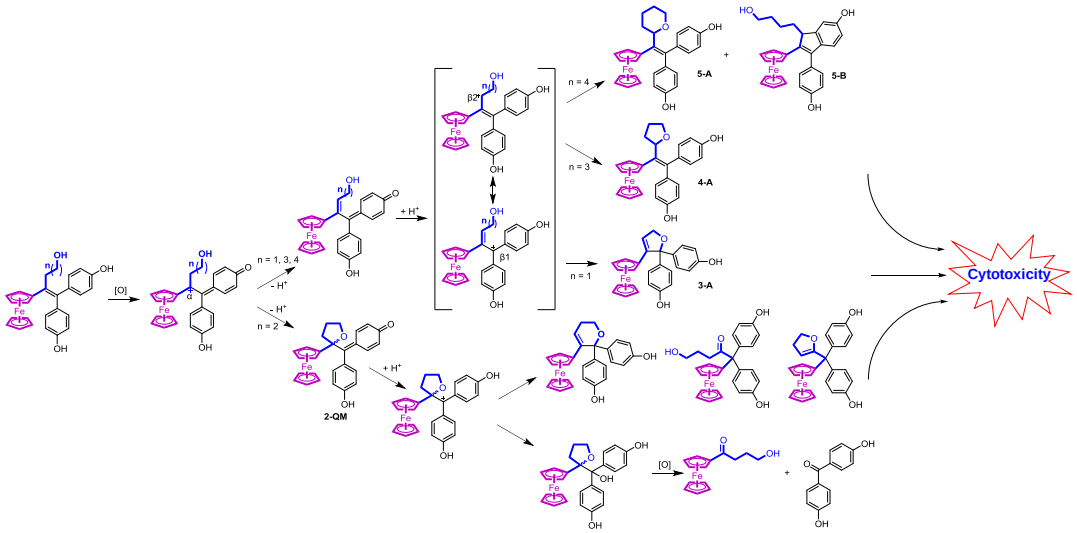

Scheme 3. Proposed mechanisms for the chemo-evolutionary sequences of ferrocidiphenols.

After the sequential loss of one proton/two electrons, the oxidation of ferrocidiphenols initially yields a cation (Scheme 3), stabilized by the adjacent ferrocenyl group and readily available for subsequent transformation. The observed ratio of intramolecular etherification to give the tetrahydrofuran-QM, versus deprotonation to generate the vinyl QM, depends markedly on the length of the hydroxyalkyl chain. In the case of the hydroxypropyl-ferrocidiphenol, **2**, oxidation primarily furnished the tetrahydrohydrofuran-quinone methide, **2-QM**, whose facile α-etherification was rationalized by DFT calculations, and which subsequently produced a great diversity of reactive metabolites (Scheme 3). Conversely, upon either extending or shortening the chain, for the hydroxyethyl-, hydroxybutyl- and hydroxypentyl-ferrocidiphenols **3**, **4** and **5**, respectively, oxidation proceeded via the deprotonation pathway to give the corresponding vinyl QMs, **3-**, **4-** and **5-QM**. Their subsequent protonation led to generation of π-allyl cationic species whose positive charge could be partially alleviated by overlap between the vacant *p* orbital on carbon and a filled *d* orbital on iron. Such interactions can be described in terms of localized molecular orbital and electrostatic potential diagrams. Once again, the length of the chain determined the further

fate of these cations. As revealed by DFT calculations, the β1-etherification is favoured for the short chain case (n = 1) to deliver predominantly the dihydrofuran product **3-A**. However, for the hydroxybutyl- and hydroxypentyl-ferrocidiphenols, **4** and **5**, β2-etherification becomes the preferred pathway and yields the corresponding tetrahydrofuran- or tetrahydropyran-derivatives, respectively. Notably, in each of these cases (n = 1, 3 and 4), the intramolecular Friedel–Crafts-type cyclization co-exists as a kinetically less favoured pathway, but does allow the isolation of the final indene **5-B**, the thermodynamic product.

Conclusions

By virtue of varying the hydroxyalkyl chain length, and the subtle modulation of the stabilities of multiple cationic intermediate species by the ferrocenyl group, the chemo-evolutionary sequences of a selected range of ferrocidiphenols have now been proposed for the first time. The state of the art of their transformations has been elucidated by a combination of multiple oxidation experiments with computational mechanistic studies. This unique chemotype evolutionary tree not only covered all ferrocidiphenol-related intermediates and analogues, but also allowed the prediction of the metabolic transformation profiles of organometallics possessing the [ferrocenyl-ene-phenol] motif. The involvement of ferrocenyl in the stabilization of carbenium ions dominates the metabolic transformation of the ferrocidiphenols, whether *via* α- or β-positional participation,[46] which may indicate the potential for diverse transformations in quinone methide chemistry.[47] Having fully established chemically the unprecedented metabolic profile of selected molecules, we then investigated their metabolic properties using enzymatic liver microsomes, *in-cellulo* rat hepatocytes and *in vivo* studies; these yielded very similar results in most cases, thus providing comprehensive data for the antitumor mechanism research of ferrocidiphenols.

Furthermore, more *in vitro* tests confirmed the strong ability of ferrocidiphenols to induce the apoptosis of breast cancer cells and the favourable selectivity on normal cells, and the cell migration and invasion studies evidenced the significant ability of certain molecules to inhibit the migratory and highly invasive behaviour of TNBC MDA-MB-231 cells. Subsequent biological experiments represented the first presentation of the ROS production of **2** at both molecular and cellular levels. Moreover, ferrocidiphenol **2** possessed acceptable pharmacokinetic properties and enabled the attenuation of the *in vivo* growth of 4T1 tumors, which accentuates the probable potential of the hydroxypropyl-ferrocidiphenols for further clinical applications. This work may not only provide the missing pieces in the transformation puzzle of the burgeoning ferrocidiphenol family, but also depict the requisite

role of ferrocene, thus opening the way to both new metallocenyl chemistry, and novel bioorganometallics for potential disease therapies.

Experimental Section

General Synthetic Methods. All reagents and solvents were obtained from commercial suppliers. THF was obtained by distillation from sodium/benzophenone. Thin layer chromatography (TLC) was performed on silica gel 60 GF_{254}. Column chromatography was performed on silica gel Merck 60 (40-63 μm). All NMR experiments (^{1}H, ^{13}C, 2D-) were carried out at room temperature on Bruker 300 and 400 NMR spectrometers. Mass spectrometry was performed with a Nermag R 10–10C spectrometer. HRMS measurements were performed on a Thermo Fischer LTQ-Orbitrap XL apparatus equipped with an electrospray source by IPCM (UMR 8232). Elemental analyses were performed by the microanalysis service of ICSN (Gif sur Yvette, France). HPLC was employed to confirm the purity of compounds to be >95%: detection at 254 nm, flow rate = 1.0 mL/min, mobile A: methyl alcohol, mobile B: water, gradient elution conditions are as follows: 20% A from 0 to 1.0 min, 20-100% A from 1.0 to 10.0 min, 100% A from 10.0 to 13.0 min, 100-20% A from 13.0 to 13.5 min, and 20% A from 13.5 to 15.0 min.

General procedure for McMurry coupling. Titanium chloride (5 eq.) was added dropwise to a suspension of zinc powder (10 eq.) in dry THF at 10-20 °C. The mixture was heated at reflux for 2 hours. A second solution of two ketone reagents (approximately 1 eq. to 1 eq.) was prepared by dissolving the two ketones in dry THF. This latter solution was added dropwise to the first solution and then the reflux was continued for the indicated time. After cooling to room temperature, the mixture was stirred with water and dichloromethane. The mixture was acidified with dilute hydrochloric acid until the dark color disappeared and was then decanted. The aqueous layer was extracted with dichloromethane and the combination of organic layers was dried on magnesium sulfate. After concentration under reduced pressure, the crude product was flash chromatographed on silica gel column with the indicated eluent to afford the alkenes.

2-Ferrocenyl-1,1-bis-(4-hydroxyphenyl)-6-hydroxy-hex-1-en, 4

$LiAlH_4$ (0.16 g, 4.2 mmol) was added slowly to the solution of methyl 5-ene-5-ferrocenyl-6,6-bis-(4-hydroxyphenyl)-hexanoate **7** (0.4 g, 0.83 mmol) in 10 ml of THF. The mixture obtained was heated at room temperature overnight. The reaction was then quenched by

water. The aqueous layer was extracted with ethyl acetate for three times. The organic layer was dried over Na_2SO_4, and evaporated. The residue was purified by column chromatography on silica gel eluting with petroleum ether/ethyl acetate (2:1) and was obtained in a yield 52 %. ^{1}H NMR (acetone-d_6) : δ 1.24-1.36 (m, 2H, CH_2), 1.36-1.50 (m, 2H, CH_2), 2.52 (t, J = 7.9 Hz, 2H, CH_2), 3.20-3.37 (m, 2H, CH_2O), 3.80 (t, J = 1.9 Hz, 2H, C_5H_4), 3.92 (t, J = 1.9 Hz, 2H, C_5H_4), 3.98 (s, 5H, Cp), 6.57 (d, J = 8.6 Hz, 2H, C_6H_4), 6.67 (d, J = 8.7 Hz, 2H, C_6H_4), 6.73 (d, J = 8.6 Hz, 2H, C_6H_4), 6.92 (d, J = 8.7 Hz, 2H, C_6H_4), 8.09 (s, 1H, OH), 8.12 (s, 1H, OH). ^{13}C NMR (acetone-d_6) : δ 27.9 (CH_2), 33.8 (CH_2), 35.3 (CH_2), 62.3 (CH_2O), 68.6 (2CH C_5H_4), 69.9 (5CH Cp), 70.1 (2CH C_5H_4), 88.5 (C C_5H_4), 115.8 (2CH C_6H_4), 115.8 (2CH C_6H_4), 131.3 (2CH C_6H_4), 131.8 (2CH C_6H_4), 135.4 (C), 137.2 (C), 137.5 (C), 139.1 (C), 156.6 (C), 156.7 (C). MS (CI, NH_3) m/z : 469 $[M+H]^+$. HRMS (ESI, $C_{28}H_{28}FeO_3$: $[M]^{+\cdot}$) calcd: 468.1388, found: 468.1382. Anal. Calcd for $C_{28}H_{28}FeO_3(H_2O)_{0.25}$: C, 71.12; H, 6.07. Found: C, 71.21; H, 6.03. Purity: 97.18%.

2-Ferrocenyl-1,1-bis-(4-hydroxyphenyl)-7-hydroxy-hept-1-en, 5

$LiAlH_4$ (0.30 g, 7.9 mmol) was added slowly to the solution of methyl 6-ene-6-ferrocenyl-7,7-bis-(4-hydroxyphenyl)-heptanoate **8** (0.7250 g, 0.83 mmol) in 10 ml of THF. The mixture obtained was heated at room temperature overnight. The reaction was then quenched by water. The aqueous layer was extracted with ethyl acetate for three times. The organic layer was dried over Na_2SO_4, and evaporated. The residue was purified by column chromatography on silica gel eluting with petroleum ether/ethyl acetate (2:1) and was obtained in a yield 93 %. ^{1}H NMR (acetone-d_6) : δ 1.09-1.22 (m, 2H, CH_2), 1.22-1.49 (m, 4H, $2CH_2$), 2.50 (t, J = 8.0 Hz, 2H, CH_2), 3.30-3.39 (m, 2H, CH_2), 3.78 (t, J = 1.9 Hz, 2H, C_5H_4), 3.92 (t, J = 1.9 Hz, 2H, C_5H_4), 3.98 (s, 5H, Cp), 6.57 (d, J = 8.6 Hz, 2H, 2CH C_6H_4), 6.67 (d, J = 8.6 Hz, 2H, 2CH C_6H_4), 6.73 (d, J = 8.6 Hz, 2H, 2CH C_6H_4), 6.92 (d, J = 8.6 Hz, 2H, 2CH C_6H_4), 8.08 (s, 1H, OH), 8.11 (s, 1H, OH). ^{13}C NMR (acetone-d_6) : δ 26.9 (CH_2), 31.4 (CH_2), 33.6 (CH_2), 35.6 (CH_2), 62.5 (OCH_2), 68.6 (2CH C_5H_4), 69.9 (5CH Cp), 70.0 (2CH C_5H_4), 88.6 (C C_5H_4), 115.8 (2CH C_6H_4), 115.8 (2CH C_6H_4), 131.3 (2CH C_6H_4), 131.8 (2CH C_6H_4), 135.4 (C), 137.2 (C), 137.5 (C), 139.0 (C), 156.6 (C), 156.7 (C). MS (CI, NH_3) m/z : 483 $[M+H]^+$, 500 $[M+NH_4]^+$. HRMS (ESI, $C_{29}H_{30}FeO_3$: $[M]^{+\cdot}$) calcd: 482.1544, found: 482.1534. Purity: 95.55%.

4,4'-(3-Ferrocenyl-2,5-dihydrofuran-2,2-diyl)diphenol, 3-A

Freshly made Ag_2O (17.9 mg, 0.31 mmol) was added to a solution of 2-ferrocenyl-1,1-bis-(4-hydroxyphenyl)-4-hydroxy-but-1-ene **3** (0.034 g, 0.077 mmol) in 1 ml of acetone. The reaction was monitored by TLC until complete conversion of the starting material (120 minutes). Filtration was followed by removal of the solvent under reduced pressure to give **3-A** as a dark red solid in a yield 63 %. ^{1}H NMR (400 MHz, acetone-d_6) δ 8.38 (s, 2H), 7.18 (d, J = 8.3 Hz, 4H), 6.78 (d, J = 8.2 Hz, 4H), 6.36 (t, J = 1.9 Hz, 1H), 4.61 (d, J = 2.0 Hz, 2H), 4.09 (dd, J = 5.0, 1.8 Hz, 4H), 3.92 (s, 5H). ^{13}C NMR (101 MHz, acetone-d_6) δ 156.67, 143.82, 135.63, 129.75, 122.34, 114.14, 94.50, 79.87, 72.61, 69.76, 68.39, 67.89. ESI (m/z): $[MH]^+$ calculated for $C_{26}H_{23}FeO_3$, 439.30; found 439.24. HRMS (ESI, $C_{26}H_{22}FeO_3$: $[M]^{+\cdot}$) calcd: 438.0913, found: 438.0926. Purity: 97.26%.

4,4'-(2-Ferrocenyl-2-(tetrahydrofuran-2-yl)ethene-1,1-diyl)diphenol, 4-A

Freshly made Ag_2O (65 mg, 0.3 mmol) was added to a solution of 2-ferrocenyl-1,1-bis-(4-hydroxyphenyl)-6-hydroxy-hex-1-en **4** (35 mg, 0.075 mmol) in 1.5 ml of acetone. The reaction was monitored by TLC until complete conversion of the starting material (120 minutes). Filtration was followed by removal of the solvent under reduced pressure to give **4-A** as a dark red solid in a yield 29 %. ^{1}H NMR (400 MHz, acetone-d_6) δ 8.36 (s, 2H), 7.05 (d, J = 8.6 Hz, 2H), 6.87 (d, J = 8.6 Hz, 2H), 6.79 – 6.71 (m, 4H), 4.71 (dd, J = 9.8, 6.7 Hz, 1H), 4.11 (s, 1H), 4.03 (m, 2H), 3.96 – 3.90 (m, 2H), 3.90 – 3.86 (m, 1H), 3.56 (q, J = 7.9 Hz, 1H), 2.42 – 2.26 (m, 1H), 1.88 (m, 3H). ^{13}C NMR (101 MHz, acetone-d_6) δ 156.97, 143.22, 137.54, 136.80, 134.36, 131.74, 131.45, 115.81, 115.43, 85.03, 82.56, 70.97, 70.56, 70.09, 68.31, 68.18, 67.89, 31.85, 26.63. HRMS (ESI, $C_{28}H_{26}FeO_3$: $[M]^{+\cdot}$) calcd: 466.1226, found: 466.1230. Purity: 97.98%.

4,4'-(2-Ferrocenyl-2-(tetrahydro-2*H*-pyran-2-yl)ethene-1,1-diyl)diphenol, 5-A

and 2-ferrocenyl-1-(4-hydroxybutyl)-3-(4-hydroxyphenyl)-1*H*-inden-6-ol, 5-B

Freshly made Ag_2O (16.8 mg, 0.29 mmol) was added to a solution of 2-ferrocenyl-1,1-bis-(4-hydroxyphenyl)-7-hydroxy-hept-1-en **5** (0.035 mg, 0.073 mmol) in 1 ml of acetone. The reaction was monitored by TLC until complete conversion of the starting material. Filtration was followed by removal of the solvent under reduced pressure. The residue was purified by column chromatography on silica gel eluting with petroleum ether/ethyl acetate to give **5-A** as a dark red solid in a yield 36 % and **5-B** as a dark red solid in a yield 21 %. **5-A**, ^{1}H NMR (400 MHz, acetone-d_6) δ 8.33 (d, J = 15.9 Hz, 2H), 7.08 (d, J = 8.2 Hz, 2H), 6.83 (d, J = 8.5 Hz, 2H), 6.80 – 6.75 (m, 2H), 6.72 (d, J = 8.1 Hz, 2H), 4.41 – 4.23 (m, 1H), 4.14 (s, 5H),

4.10 – 3.95 (m, 6H), 3.32 (td, *J* = 11.8, 2.3 Hz, 1H), 2.31 (qd, *J* = 12.8, 4.0 Hz, 1H), 1.84 (d, *J* = 13.1 Hz, 1H), 1.58 (dt, *J* = 12.9, 3.9 Hz, 2H), 1.44 (d, *J* = 14.5 Hz, 1H). ^{13}C NMR (101 MHz, acetone-d_6) δ 156.24, 156.05, 142.13, 136.59, 136.10, 134.95, 131.05, 130.65, 114.89, 114.54, 81.29, 71.00, 70.17, 69.30, 68.13, 67.38, 67.21, 30.27, 25.91, 24.32. ESI (m/z): [M]+ calculated for $C_{29}H_{28}FeO_3$, 480.14; found 480.29. HRMS (ESI, $C_{29}H_{28}FeO_3$: $[M]^{+\cdot}$) calcd: 480.1382, found: 480.1388. Purity: 96.53%. **5-B**, ^{1}H NMR (400 MHz, acetone-d_6) δ 8.57 (s, 1H), 8.17 (d, *J* = 3.1 Hz, 1H), 7.20 (ddd, *J* = 9.0, 4.1, 2.0 Hz, 2H), 7.09 – 6.95 (m, 5H), 6.67 (dd, *J* = 6.5, 3.6 Hz, 2H), 4.50 (d, *J* = 21.1 Hz, 1H), 4.34 – 4.09 (m, 4H), 4.09 – 3.98 (m, 5H), 3.83 – 3.66 (m, 1H), 3.52 (s, 4H), 2.25 (d, *J* = 10.2 Hz, 1H), 1.95 (d, *J* = 14.2 Hz, 1H), 1.55 – 1.45 (m, 2H). ^{13}C NMR (101 MHz, acetone-d_6) δ 156.90, 130.92, 119.69, 114.94, 113.06, 110.66, 69.65, 69.43, 68.15, 66.50, 61.65, 59.74, 50.56, 33.06, 21.28. ESI (m/z): [M]+ calculated for $C_{29}H_{28}FeO_3$, 480.14; found 480.29. HRMS(ESI, $C_{29}H_{28}FeO_3$: $[M]^{+\cdot}$) calcd: 480.1382, found: 480.1389. Purity: 95.46%.

ROS monitoring by fluorescence spectroscopy. 2′,7′-Dichlorofluorescin diacetate (DCFH-DA; 4.9 mg) was dissolved in DMF (100 μL) and added with aqueous NaOH (0.1 M, 900 μL). The resulting mixture was incubated for 30 min at 22 °C in the dark to obtain a stock solution of DCFH (10 mM). This solution was diluted by containing 3-(N-morpholino) propanesulfonic acid buffer (MOPS, 100 mM, pH 7.4), N,N,N',N'-ethylenediaminetetraacetic acid (EDTA, 10 mM), glutathione (GSH, 5 mM), and H_2O_2 (10 mM) to acquire the final solution of DCFH (10 μM). Monitoring of the fluorescence (λ_{ex} = 501 nm, λ_{em} = 529 nm, Bandwidth (nm) = 0.4, Source Light Path: Xenon Lamp, Detector Light Path: Visible PMT-980) of this solution was started. After the intensity is stable, compounds (10 μL, final concentration 0.1 mM) were added and the fluorescence monitoring was continued for the 225 mins. Meanwhile, monitoring generation of reactive oxygen species in the presence of control compounds in cell free settings.

Intracellular ROS production assay. MDA-MB-231 cells or 4T1 cells were seeded in 6-well plates at a density of 3×10^5 and allowed to attach for 24 h. Then, the cell culture medium was replaced with a fresh medium containing **2**, **3**, **4** (2 μM) or DMSO, and after incubation for 3h or 24 h. The culture medium was removed and cells were incubated with a medium containing the 5(6)-carboxy-20,70-dichlorodihydrofluorescein diacetate (DCFH-DA; 10 μM; Beyotime) probe for 30 min. Then, the medium was removed, and cells were washed with PBS three times. Finally, the fluorescence of live cells in the suspensions was determined by using flow cytometry.

Reactive oxygen species fluorescence imaging was taken by using laser scanning confocal microscopy. MDA-MB-231 cells or 4T1 cells were incubated with medium containing **2**, **3**, **4** (2 μM) or DMSO, and after incubation for 3 h. After incubation, cells were harvested and washed with PBS. Then, cells were incubated with a medium containing the DCFH-DA (10 μM) probe at 37°C for 30 min. The cells were washed three times with PBS to remove redundant DCFH-DA. The ROS level was examined by analyzing green fluorescence intensity using laser scanning confocal microscopy.

Antitumor Effect Evaluation In Vivo. All animal work was performed in accordance with the Institutional Animal Care and was approved by the Ethics for Animal Experiments committee of the Ocean University of China. After adaptive feeding of male BALB/c mice weighing 14-19 g for 3 days, axillary injection containing 5×10^5 cell suspensions of 4T1 cells. 25 mice were randomly divided into 5 groups according to their body weight (n=5 in each group) the next day. The negative control group was intraperitoneally injected with the blank solvent (DMSO/Tween80/PEG/physiological saline=10:5:40:45%) and the drug-treated groups received daily intraperitoneal injection of compound **2** and **3** with the dose of 60 mg/kg and 30 mg/kg. Record daily changes in tumor volume and body weight of mice. Tumor volume was calculated according to the equation V = L×W2/2, where L represented tumor length and W represented tumor width. After 12 days of continuous administration, the mice were sacrificed painlessly. Mouse organs and tumors were collected for pathological section analysis.

Statistical Analysis. Data were presented as mean ± SD (represented by error bars) for all *in vitro* experiments. All the experiments had three replicates (n = 3). *In vivo* antitumor Student's t-test was used for comparing the two groups, and significant differences were indicated using *P < 0.05, *P < 0.01, and ***P < 0.001. Statistical analysis was performed with GraphPad Prism 8.0.1.

Acknowledgements

Y. W. received funding from Qingdao Marine Science and Technology (2022QNLM030003-2), Taishan Scholar Youth Expert Program in Shandong Province (tsqn202103035) and Distinguished Young Scholars of Shandong Provincial Natural Science Foundation (Overseas, 2022HWYQ-069).

Author contributions

H. W., X. F., P. X. and S. Y. contributed equally to this manuscript. Y. W. and C. Z. designed the study. H. W., P. P., J. W., W. L. and H. Q. performed the synthesis and characterization of chemical compounds. X. F., Y. X. and X. Q. performed the *in vitro* and *in vivo* anticancer evaluation of the compounds. P. X. and C. Z. performed the DFT calculation work. S. Y., Q. Z. and S. G. contributed to the metabolism oxidation experiments and data analysis. M. J. M. prepared the crystal figure. Y. W., C. Z. and G. J. supervised the study. Y. W., C. Z. and M. J. M. wrote the manuscript. All authors participated in valuable discussion and manuscript correction.

Supplementary Information

Experimental procedures for syntheses and biological evaluation, supplementary Schemes S1-2, Figures S3-26 and Tables S27-29, X-ray crystallographic data, Computational methods and details, cif files and Molecular Formula Strings. This material is available free of charge via the Internet at http://www.acs.org.

Abbreviations

AUC, area under the concentration curve; Cl, clearance; C_{max}, maximum concentration detected after intravenous dose; DCFH-DA, 2′,7′-dichlorofluorescin diacetate; DFT, density functional theory; DMF, dimethylformamide; DMSO, dimethyl sulfoxide; DXR, doxorubicin; EDTA, N,N,N’,N’-ethylenediaminetetraacetic acid; EPR, electron paramagnetic resonance; ER, estrogen receptor; ESI, electrospray ionization; FITC, fluorescein isothiocyanate; GSH, glutathione; H&E, hematoxylin and eosin; HPLC, high performance liquid chromatography; HRMS, high-resolution mass spectrometry; IC_{50}, half-maximum inhibitory concentration; LC-MS, liquid chromatography-mass spectrometry; LM, liver microsomes; logP, logarithm of partition coefficient; LPO, lipid peroxidation products; *m/z*, mass-to-charge ratio; mM, millimolar (millimoles per liter); MRT, mean residence time; MS, mass spectrometry; NADPH, nicotinamide adenine dinucleotide phosphate; NMR, nuclear magnetic resonance; o/w, oil/water; PARP, poly ADP-ribose polymerase; PBS, Phosphate Buffered Saline; PEG, polyethylene glycol; PI, propidium iodide; PK, Pharmacokinetic; QMs, quinone methides; ROS, reactive oxygen species; TAM, tamoxifen; TGI, tumor growth inhibition; THF, tetrahydrofuran; TLC, thin-layer chromatography; TNBC, triple negative breast cancer; TrxR, thioredoxin reductase; $t_{1/2}$, half-time; UHPLC-MS, ultra-high pressure liquid chromatography mass spectrometry.

References

1. B. Rosenberg; L. Vancamp, Successful Regression of Large Solid Sarcoma 180-Tumors by Platinum Compounds. *Cancer Research* **1970,** *30* (6), 1799-1801.
2. J. J. Wilson; S. J. Lippard, Synthetic Methods for the Preparation of Platinum Anticancer Complexes. *Chem. Rev.* **2014,** *114* (8), 4470-4495.
3. T. Yang; S. Zhang; H. Yuan; Y. Wang; L. Cai; H. Chen; X. Wang; D. Song; X. Wang; Z. Guo; X. Wang, Platinum-Based TREM2 Inhibitor Suppresses Tumors by Remodeling the Immunosuppressive Microenvironment. *Angew. Chem. Int. Ed.* **2023,** *62* (2), e202213337.
4. X. Wang; X. Wang; S. Jin; N. Muhammad; Z. Guo, Stimuli-Responsive Therapeutic Metallodrugs. *Chemical Reviews* **2019,** *119* (2), 1138-1192.
5. H. Huang; K. Cao; Y. Kong; S. Yuan; H. Liu; Y. Wang; Y. Liu, A dual functional ruthenium arene complex induces differentiation and apoptosis of acute promyelocytic leukemia cells. *Chemical Science* **2019,** *10* (42), 9721-9728.
6. C. G. Hartinger; P. J. Dyson, Bioorganometallic chemistry—from teaching paradigms to medicinal applications. *Chemical Society Reviews* **2009,** *38* (2), 391-401.
7. S. M. Meier-Menches; C. Gerner; W. Berger; C. G. Hartinger; B. K. Keppler, Structure–activity relationships for ruthenium and osmium anticancer agents – towards clinical development. *Chemical Society Reviews* **2018,** *47* (3), 909-928.
8. X. Wang; M. d. G. Jaraquemada-Peláez; C. Rodríguez-Rodríguez; Y. Cao; C. Buchwalder; N. Choudhary; U. Jermilova; C. F. Ramogida; K. Saatchi; U. O. Häfeli; B. O. Patrick; C. Orvig, H4octox: Versatile Bimodal Octadentate Acyclic Chelating Ligand for Medicinal Inorganic Chemistry. *Journal of the American Chemical Society* **2018,** *140* (45), 15487-15500.
9. H. Huang; S. Banerjee; K. Qiu; P. Zhang; O. Blacque; T. Malcomson; M. J. Paterson; G. J. Clarkson; M. Staniforth; V. G. Stavros; G. Gasser; H. Chao; P. J. Sadler, Targeted photoredox catalysis in cancer cells. *Nature Chemistry* **2019,** *11* (11), 1041-1048.
10. X. Zhao; J. Zhang; W. Zhang; Z. Guo; W. Wei; X. Wang; J. Zhao, A chiral fluorescent Ir(iii) complex that targets the GPX4 and ErbB pathways to induce cellular ferroptosis. *Chemical Science* **2023,** *14* (5), 1114-1122.
11. J.-J. Zhang; M. A. Abu el Maaty; H. Hoffmeister; C. Schmidt; J. K. Muenzner; R. Schobert; S. Wölfl; I. Ott, A Multitarget Gold(I) Complex Induces Cytotoxicity Related to Aneuploidy in HCT-116 Colorectal Carcinoma Cells. *Angew. Chem. Int. Ed.* **2020,** *59* (38), 16795-16800.
12. G. Moreno-Alcántar; A. Casini, Bioinorganic supramolecular coordination complexes and their biomedical applications. *FEBS Letter* **2023,** *597* (1), 191-202.
13. W. D. J. Tremlett; D. M. Goodman; T. R. Steel; S. Kumar; A. Wieczorek-Błauż; F. P. Walsh; M. P. Sullivan; M. Hanif; C. G. Hartinger, Design concepts of half-sandwich organoruthenium anticancer agents based on bidentate bioactive ligands. *Coordination Chemistry Reviews* **2021,** *445*, 213950.
14. M. M; S. Gadre; S. Chhatar; G. Chakraborty; N. Ahmed; C. Patra; M. Patra, Potent Ruthenium–Ferrocene Bimetallic Antitumor Antiangiogenic Agent That Circumvents Platinum Resistance: From Synthesis and Mechanistic Studies to In Vivo Evaluation in Zebrafish. *Journal of Medicinal Chemistry* **2022,** *65* (24), 16353-16371.
15. B. Albada; N. Metzler-Nolte, Highly Potent Antibacterial Organometallic Peptide Conjugates. *Accounts of Chemical Research* **2017,** *50* (10), 2510-2518.
16. M. Dörr; E. Meggers, Metal complexes as structural templates for targeting proteins. *Current Opinion in Chemical Biology* **2014,** *19*, 76-81.
17. Y. Huang; M. Lv; B. Guo; G. Hu; Y. Qian; Z. Su; X. Xue; H.-K. Liu, Selectively attacking tumor cells of Ru/Ir–arene complexes based on meclofenamic acid via cyclooxygenase-2 inhibition. *Dalton Transactions* **2023,** *52* (20), 6922-6933.
18. Z. Liang; L. Liu; Y. Zhou; W. Liu; Y. Lu, Research Progress on Bioactive Metal Complexes against ER-Positive Advanced Breast Cancer. *Journal of Medicinal Chemistry* **2023,** *66* (4), 2235-2256.

19. Y. Lai; N. Lu; S. Luo; H. Wang; P. Zhang, A Photoactivated Sorafenib-Ruthenium(II) Prodrug for Resistant Hepatocellular Carcinoma Therapy through Ferroptosis and Purine Metabolism Disruption. *Journal of Medicinal Chemistry* **2022,** *65* (19), 13041-13051.
20. G. Jaouen; A. Vessieres; S. Top, Ferrocifen type anti cancer drugs. *Chem. Soc. Rev.* **2015,** *44* (24), 8802-8817.
21. M. Patra; G. Gasser, *Nature Rev. Chem.* **2017,** (1), 0066.
22. D. R. van Staveren; N. Metzler-Nolte, Bioorganometallic Chemistry of Ferrocene. *Chemical Reviews* **2004,** *104* (12), 5931-5986.
23. K. Kowalski, Organometallic nucleosides—Synthesis, transformations, and applications. *Coordination Chemistry Reviews* **2021,** *432*, 213705.
24. B. Sharma; V. Kumar, Has Ferrocene Really Delivered Its Role in Accentuating the Bioactivity of Organic Scaffolds? *Journal of Medicinal Chemistry* **2021,** *64* (23), 16865-16921.
25. H.-G. Xu; M. Schikora; M. Sisa; S. Daum; I. Klemt; C. Janko; C. Alexiou; G. Bila; R. Bilyy; W. Gong; M. Schmitt; L. Sellner; A. Mokhir, An Endoplasmic Reticulum Specific Pro-amplifier of Reactive Oxygen Species in Cancer Cells. *Angew. Chem. Int. Ed.* **2021,** *60* (20), 11158-11162.
26. W.-J. Wang; Y.-Y. Ling; Y.-M. Zhong; Z.-Y. Li; C.-P. Tan; Z.-W. Mao, Ferroptosis-Enhanced Cancer Immunity by a Ferrocene-Appended Iridium(III) Diphosphine Complex. *Angew. Chem. Int. Ed.* **2022,** *61* (16), e202115247.
27. J. Yan; K. Yue; X. Fan; X. Xu; J. Wang; M. Qin; Q. Zhang; X. Hou; X. Li; Y. Wang, Synthesis and bioactivity evaluation of ferrocene-based hydroxamic acids as selective histone deacetylase 6 inhibitors. *European Journal of Medicinal Chemistry* **2023,** *246*, 115004.
28. S. S. Braga; A. M. S. Silva, A New Age for Iron: Antitumoral Ferrocenes. *Organometallics* **2013,** *32* (20), 5626-5639.
29. P. Biegański; E. Kovalski; N. Israel; E. Dmitrieva; D. Trzybiński; K. Woźniak; V. Vrček; M. Godel; C. Riganti; J. Kopecka; H. Lang; K. Kowalski, Electronic Coupling in 1,2,3-Triazole Bridged Ferrocenes and Its Impact on Reactive Oxygen Species Generation and Deleterious Activity in Cancer Cells. *Inorganic Chemistry* **2022,** *61* (25), 9650-9666.
30. A. Vessières; Y. Wang; M. J. McGlinchey; G. Jaouen, Multifaceted chemical behaviour of metallocene (M = Fe, Os) quinone methides. Their contribution to biology. *Coordination Chemistry Reviews* **2021,** *430*, 213658.
31. D. Hamels; P. M. Dansette; E. A. Hillard; S. Top; A. Vessieres; P. Herson; G. Jaouen; D. Mansuy, Ferrocenyl Quinone Methides as Strong Antiproliferative Agents: Formation by Metabolic and Chemical Oxidation of Ferrocenyl Phenols. *Angew. Chem. Int. Ed.* **2009,** *48* (48), 9124-9126.
32. P. Messina; E. Labbe; O. Buriez; E. A. Hillard; A. Vessieres; D. Hamels; S. Top; G. Jaouen; Y. M. Frapart; D. Mansuy; C. Amatore, Deciphering the Activation Sequence of Ferrociphenol Anticancer Drug Candidates. *Chem. Eur. J.* **2012,** *18* (21), 6581-6587.
33. C. Bruyere; V. Mathieu; A. Vessières; P. Pigeon; S. Top; G. Jaouen; R. Kiss, Ferrocifen derivatives that induce senescence in cancer cells selected examples. *J. Inorg. Biochem.* **2014,** *141*, 144-151.
34. A. Citta; A. Folda; A. Bindoli; P. Pigeon; S. Top; A. Vessieres; M. Salmain; G. Jaouen; M. P. Rigobello, Evidence for targeting thioredoxin reductases with ferrocenyl quinone methides. A possible molecular basis for the antiproliferative effect of hydroxyferrocifens on cacer cells. *J. Med. Chem.* **2014,** *57* (21), 8849-8859.
35. P. Pigeon; Y. Wang; S. Top; F. Najlaoui; M. C. Garcia Alvarez; J. Bignon; M. J. McGlinchey; G. Jaouen, A New Series of Succinimido-ferrociphenols and Related Heterocyclic Species Induce Strong Antiproliferative Effects, Especially against Ovarian Cancer Cells Resistant to Cisplatin. *Journal of Medicinal Chemistry* **2017,** *60* (20), 8358-8368.
36. V. Scalcon; A. Citta; A. Folda; A. Bindoli; M. Salmain; I. Ciofini; S. Blanchard; J. de Jésús Cázares-Marinero; Y. Wang; P. Pigeon; G. Jaouen; A. Vessières; M. P. Rigobello, Enzymatic oxidation of ansa-ferrocifen leads to strong and selective thioredoxin reductase inhibition in vitro. *Journal of Inorganic Biochemistry* **2016,** *165*, 146-151.

37. Y. Wang; P. Pigeon; S. Top; M. J. McGlinchey; G. Jaouen, Organometallic Antitumor Compounds: Ferrocifens as Precursors to Quinone Methides. *Angew. Chem. Ed. Int.* **2015,** *54* (35), 10230-10233.
38. Y. Wang; P. M. Dansette; P. Pigeon; S. Top; M. J. McGlinchey; D. Mansuy; G. Jaouen, A new generation of ferrociphenols leads to a great diversity of reactive metabolites, and exhibits remarkable antiproliferative properties. *Chemical Science* **2018,** *9* (1), 70-78.
39. E. Hillard; A. Vessières; L. Thouin; G. Jaouen; C. Amatore, Ferrocene-Mediated Proton-Coupled Electron Transfer in a Series of Ferrocifen-Type Breast-Cancer Drug Candidates. *Angew. Chem. Int. Ed.* **2006,** *45* (2), 285-290.
40. K. Zeilinger; N. Freyer; G. Damm; D. Seehofer; F. Knöspel, Cell sources for in vitro human liver cell culture models. *Experimental biology and medicine (Maywood, N.J.)* **2016,** *241* (15), 1684-98.
41. L. Yin; J.-J. Duan; X.-W. Bian; S.-c. Yu, Triple-negative breast cancer molecular subtyping and treatment progress. *Breast Cancer Research* **2020,** *22* (1), 61.
42. H. Hagen; P. Marzenell; E. Jentzsch; F. Wenz; M. R. Veldwijk; A. Mokhir, Aminoferrocene-Based Prodrugs Activated by Reactive Oxygen Species. *Journal of Medicinal Chemistry* **2012,** *55* (2), 924-934.
43. Y. Wang; P. Pigeon; W. Li; J. Yan; P. M. Dansette; M. Othman; M. J. McGlinchey; G. Jaouen, Diversity-oriented synthesis and bioactivity evaluation of N-substituted ferrocifen compounds as novel antiproliferative agents against TNBC cancer cells. *European Journal of Medicinal Chemistry* **2022,** *234*, 114202.
44. Scott J. Dixon; Kathryn M. Lemberg; Michael R. Lamprecht; R. Skouta; Eleina M. Zaitsev; Caroline E. Gleason; Darpan N. Patel; Andras J. Bauer; Alexandra M. Cantley; Wan S. Yang; B. Morrison, III; Brent R. Stockwell, Ferroptosis: An Iron-Dependent Form of Nonapoptotic Cell Death. *Cell* **2012,** *149* (5), 1060-1072.
45. Wan S. Yang; R. SriRamaratnam; Matthew E. Welsch; K. Shimada; R. Skouta; Vasanthi S. Viswanathan; Jaime H. Cheah; Paul A. Clemons; Alykhan F. Shamji; Clary B. Clish; Lewis M. Brown; Albert W. Girotti; Virginia W. Cornish; Stuart L. Schreiber; Brent R. Stockwell, Regulation of Ferroptotic Cancer Cell Death by GPX4. *Cell* **2014,** *156* (1), 317-331.
46. S. Barlow; L. M. Henling; M. W. Day; W. P. Schaefer; J. C. Green; T. Hascall; S. R. Marder, Metallocene-Terminated Allylium Salts: The Effect of End Group on Localization in Polymethines. *Journal of the American Chemical Society* **2002,** *124* (22), 6285-6296.
47. B. J. Nachtsheim, Mild map to quinone methides. *Nature Chemistry* **2020,** *12* (4), 326-328.

Table of Contents Graphic

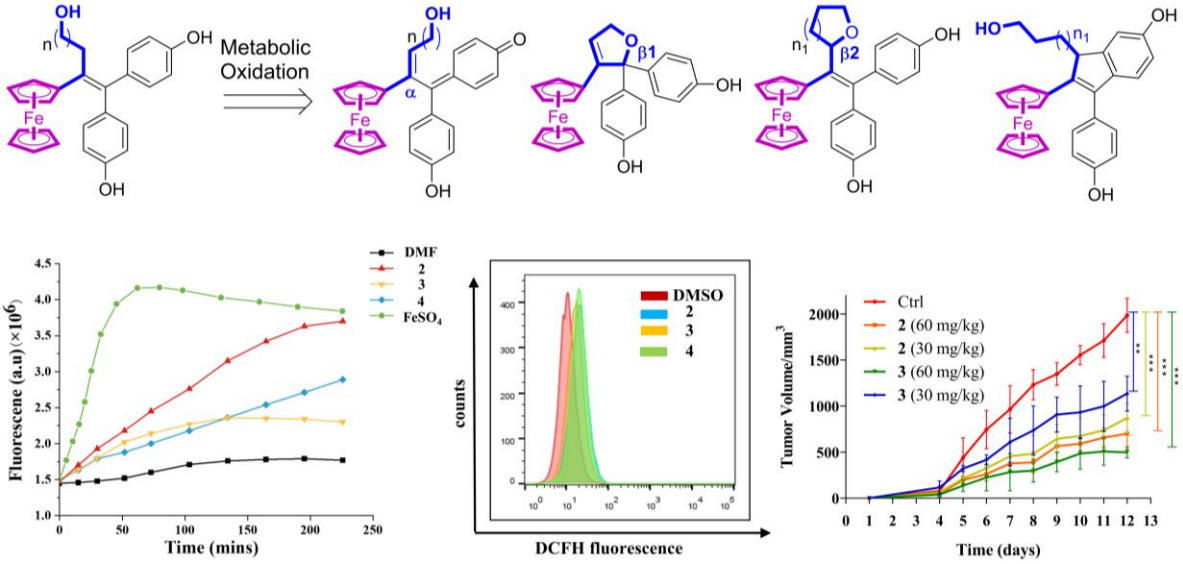

Deciphering the Diversified Metabolic Behaviour of Hydroxyalkyl Ferrocidiphenol Anticancer Complexes

Supplementary Data

Hui Wang,[a]# Xuejing Fan,[a]# Pei-Pei Xie,[b]# Shuang Yang,[a]# Pascal Pigeon,[c,d] Ying Xiong,[e] Susu Gai,[a] Xin Qi,[a] Jing Wang,[a] Qianer Zhang,[a] Wei Li,[a] Huimei Qian,[a] Michael J. McGlinchey,[f] Gérard Jaouen,[c,d], Chao Zheng,[b]* and Yong Wang[a]*

[a] Key Laboratory of Marine Drugs, Chinese Ministry of Education; School of Medicine and Pharmacy, Ocean University of China, Qingdao 26003, Shandong, P. R. China; Laboratory for Marine Drugs and Bioproducts, Pilot National Laboratory for Marine Science and Technology, Qingdao 266200, P. R. China

E-mail: wangyong8866@ouc.edu.cn

[b] State Key Laboratory of Organometallic Chemistry, Shanghai Institute of Organic Chemistry, Chinese Academy of Sciences, 345 Lingling Lu, Shanghai 200032, P. R. China

E-mail: zhengchao@sioc.ac.cn

[c] PSL, Chimie ParisTech, 11 rue Pierre et Marie Curie, F-75005 Paris, France

[d] Sorbonne Université, UMR 8232 CNRS, IPCM, 4 place Jussieu, F-75005 Paris, France

[e] School of Pharmacy, Fudan University, Shanghai, 201203, China.

[f] UCD School of Chemistry, University College Dublin, Belfield, Dublin 4, D04 C1P1, Ireland

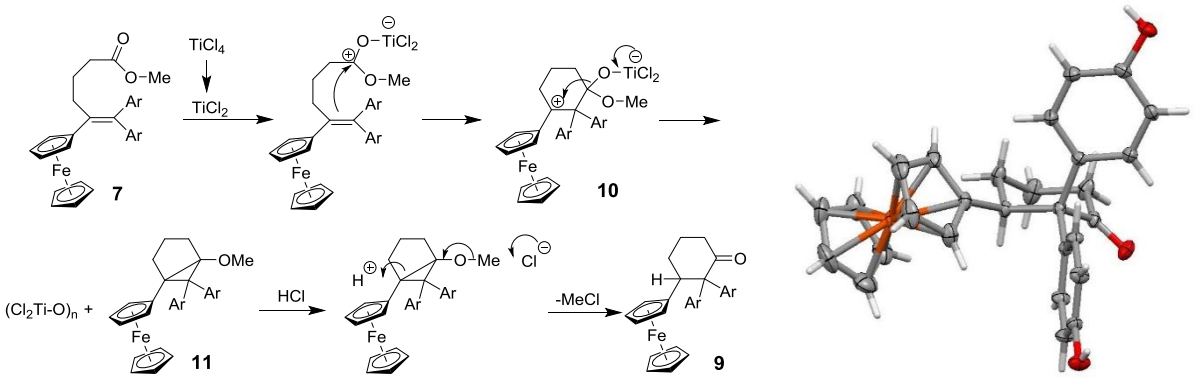

Scheme S1. Proposed mechanism for the formation of the cyclohexanone byproduct (left), **9**, and its molecular structure (right). One one can envisage initial attack by the reduced titanium species on the ester oxygen, cyclization to position the cationic site adjacent to the ferrocenyl group, as in **10**, abstraction of the ketonic oxygen by titanium with concomitant formation of the [3.1.0]-bicyclohexane, **11**, and finally ring-opening of the cyclopropyl ring upon attack by HCl. Note that in this process, the ketonic oxygen in the final product is derived from the methoxy group, and that the initial cyclization is particularly favoured by formation of a six-membered ring, a situation not available to the other hydroxyalkyl-ferrocidiphenol precursor esters. The X-ray structure of **9** is shown in Scheme 3 and the chair conformation of the resulting cyclohexanone, in which the bulky ferrocenyl substituent occupies an equatorial position, is evident.

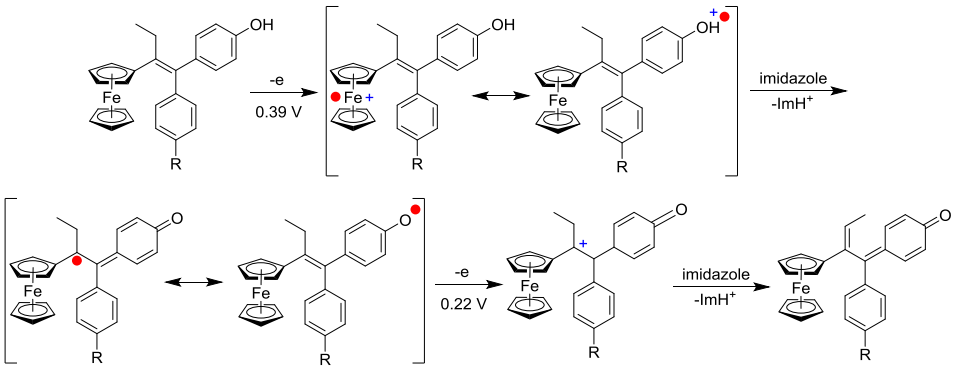

Scheme S2. Stepwise oxidation/deprotonation sequence to form a quinone methide.

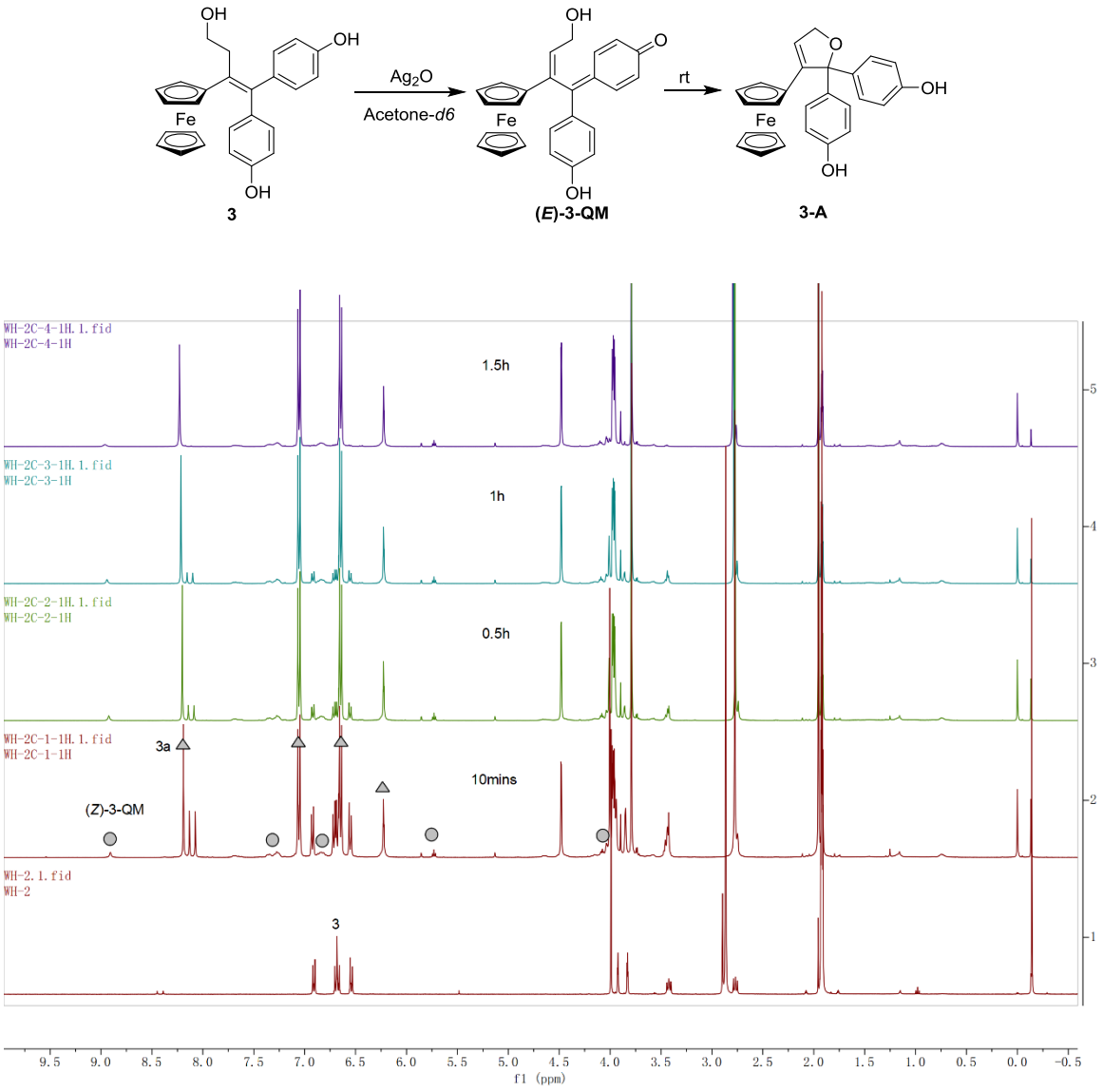

Fig. S1. ^{1}H NMR study of the evolution of **3** in the presence of Ag_2O in acetone-d_6.

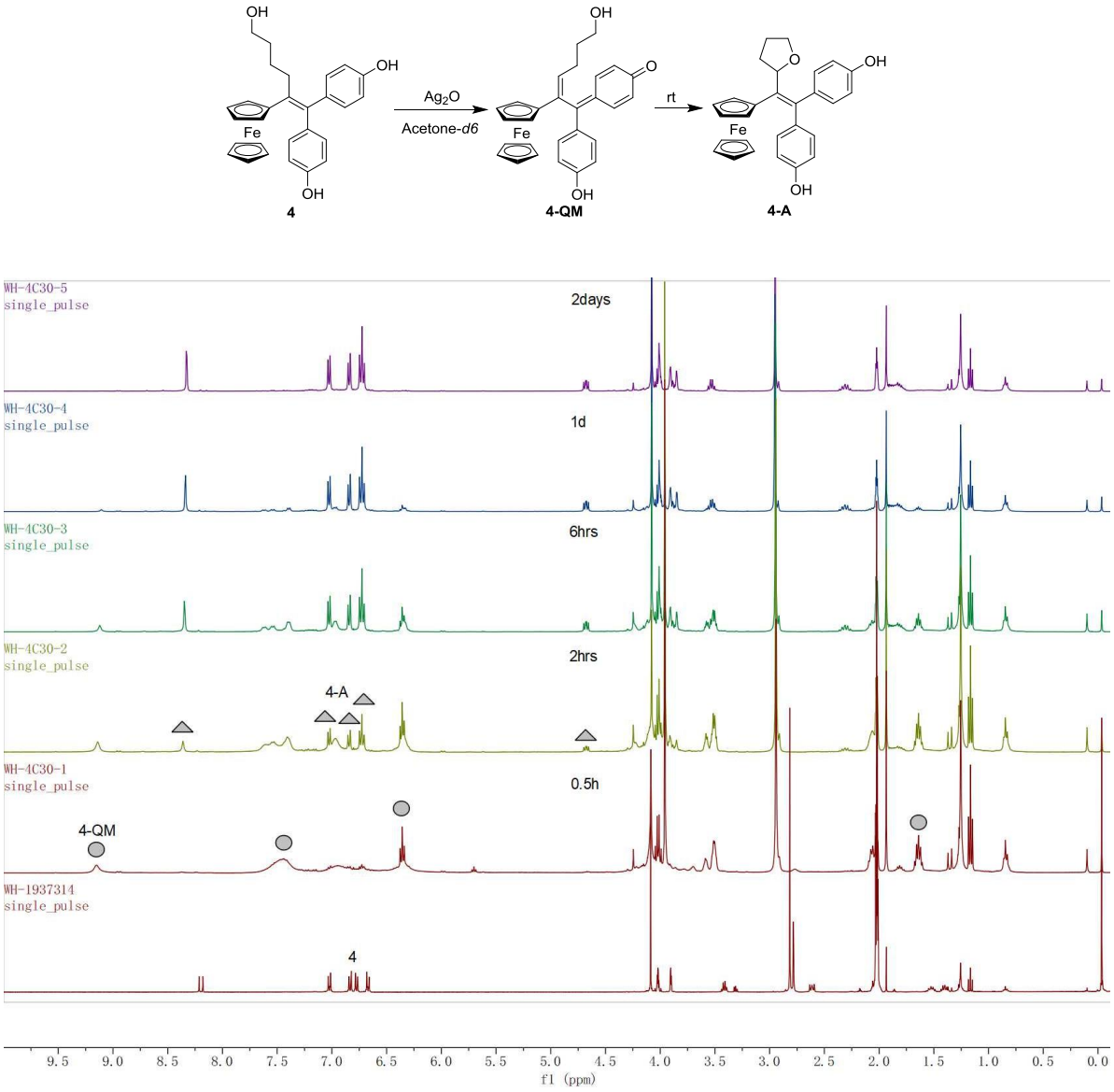

Fig. S2. ^{1}H NMR study of the evolution of **4** in the presence of Ag_2O in acetone-d_6.

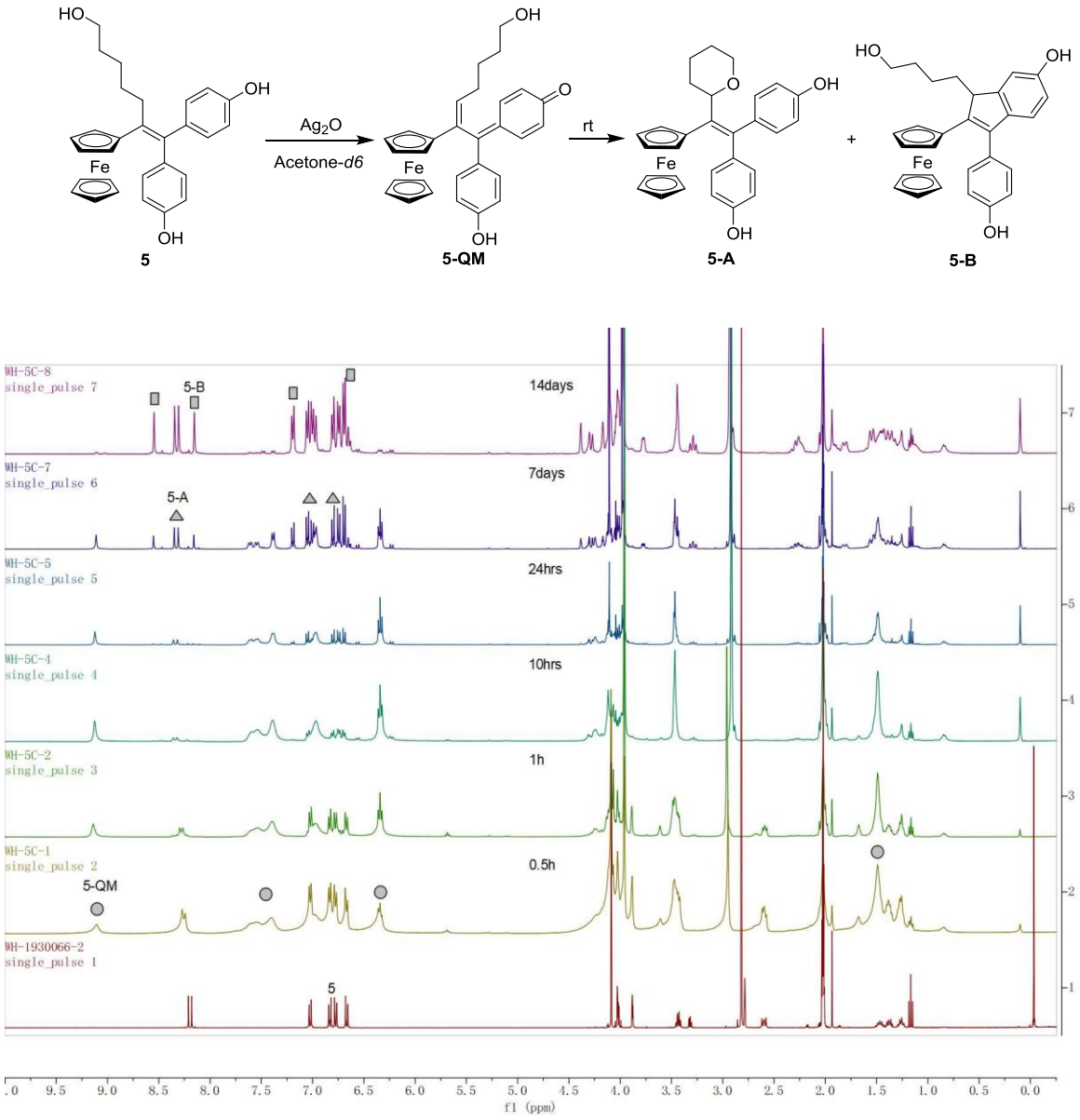

Fig. S3. ^{1}H NMR study of the evolution of **5** in the presence of Ag_2O in acetone-d_6.

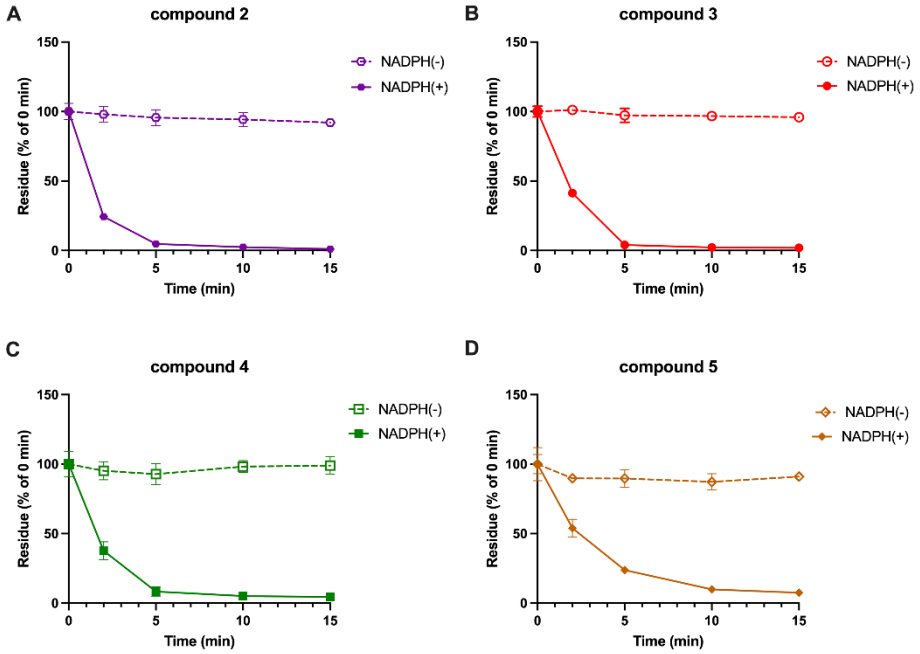

Fig. S4. Stability of ferrociphenols **2**~**5** in rat liver microsomes.

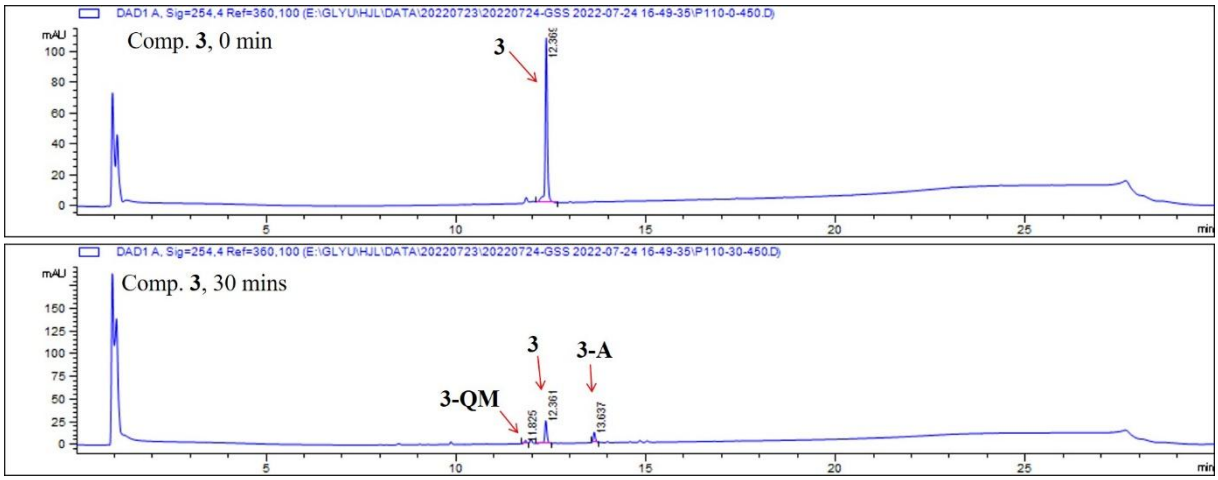

Fig. S5. The HPLC-UV analysis (254 nm) of **3** at 0 min and 30 min after incubation with rat liver microsomes.

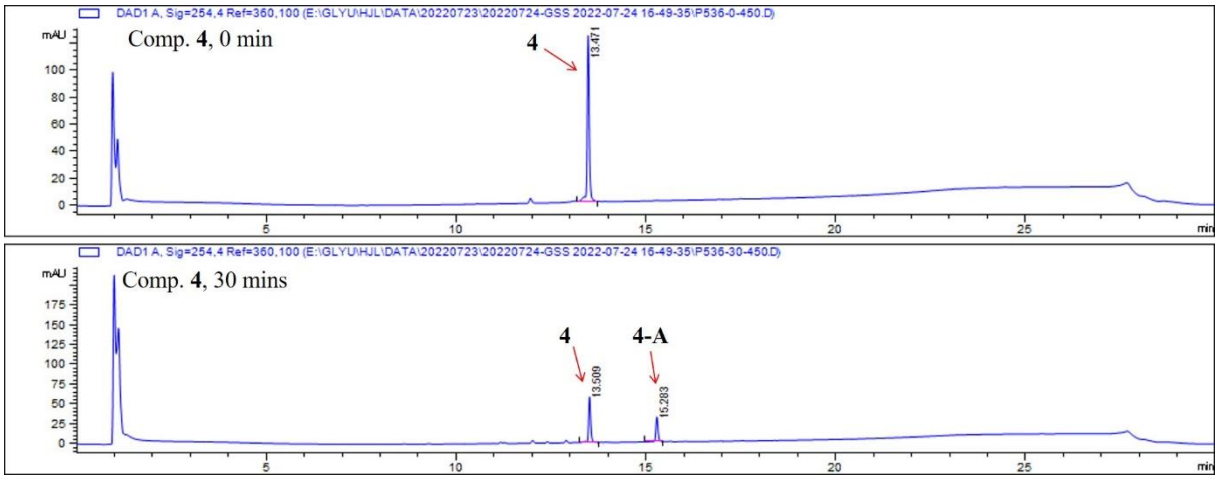

Fig. S6. The HPLC-UV analysis (254 nm) of **4** at 0 min and 30 min after incubation with rat liver microsomes.

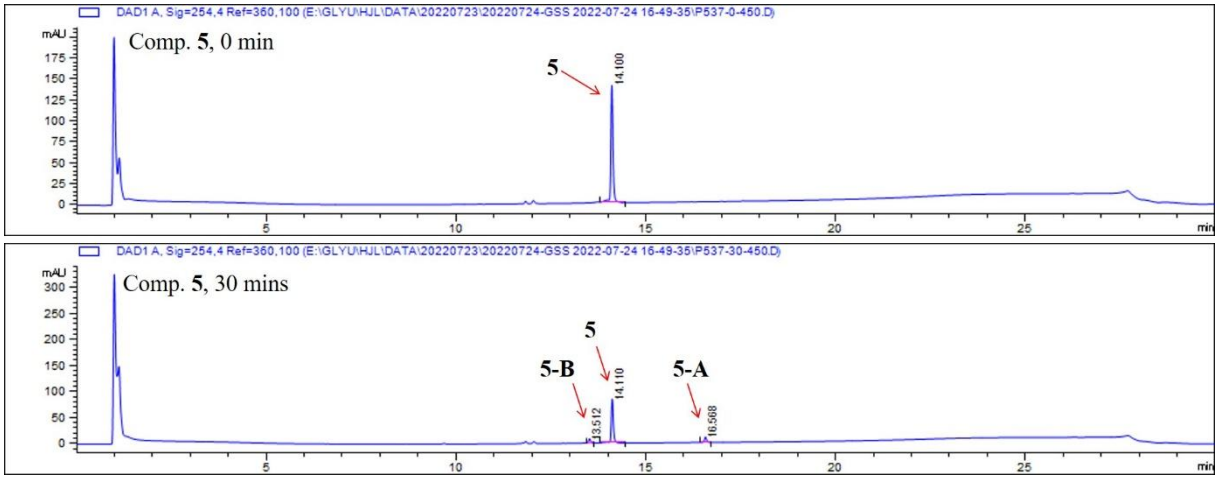

Fig. S7. The HPLC-UV analysis (254 nm) of **5** at 0 min and 30 min after incubation with rat liver microsomes.

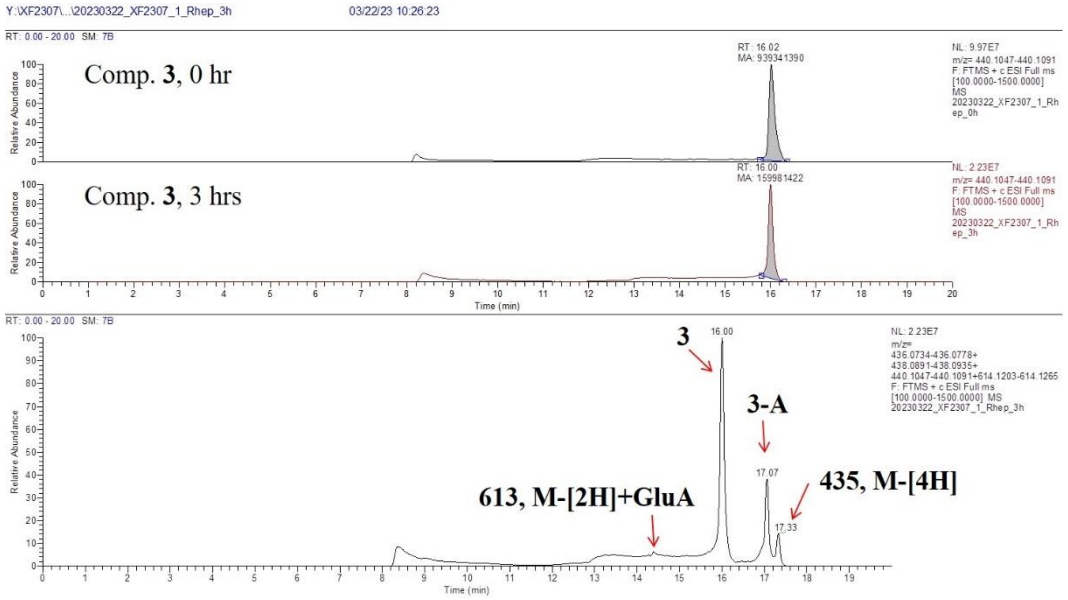

Comp.	Pathway	Rt (min)	$[M+H]^+$ calculated	MS Area(%)	$[M+H]^+$ found	SD ppm
3	-	16.00	440.1069	64.94	440.1069	0
M613	-[2H]+GluA	14.38	614.1234	1.78	614.1232	-0.3
M437 (3-A)	-[2H]	17.07	438.0913	24.99	438.0913	0
M435	-[4H]	17.33	436.0756	8.29	436.0756	0

Fig. S8. The extracted ion chromatograms of **3** and its metabolites in rat hepatocytes (upper) and their identification by LC-UV/HRMS (lower).

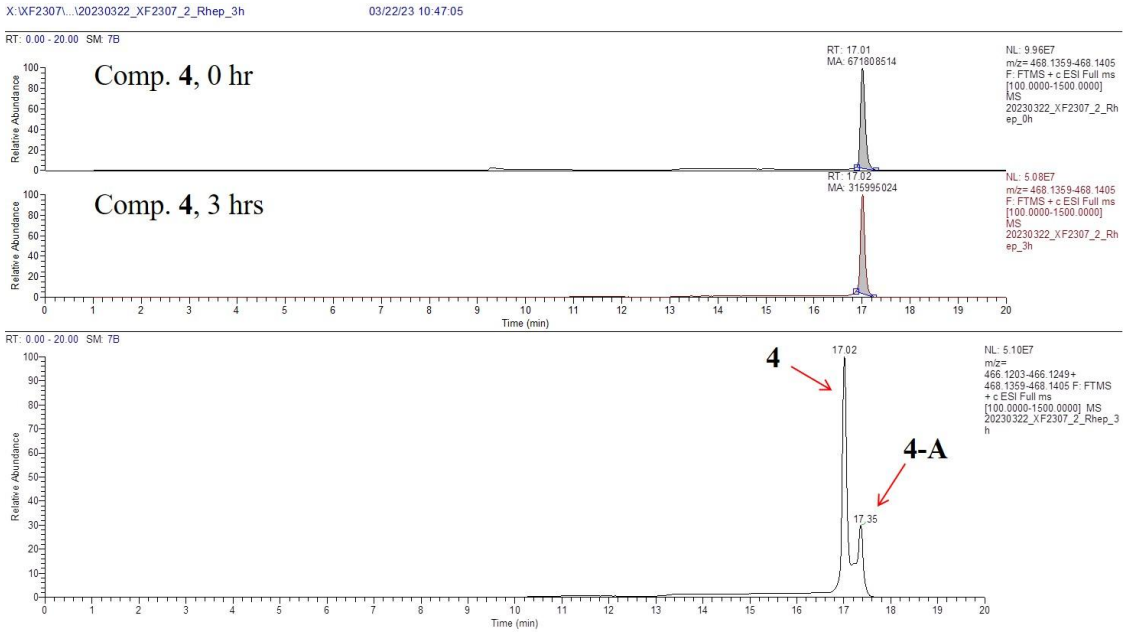

Comp.	Pathway	Rt (min)	$[M+H]^+$ calculated	MS Area(%)	$[M+H]^+$ found	SD ppm
4	-	17.02	468.1382	66.82	468.1380	-0.4
4-A	-[2H]	17.35	466.1226	33.18	466.1224	-0.4

Fig. S9. The extracted ion chromatograms of **4** and its metabolites in rat hepatocytes (upper) and their identification by LC-UV/HRMS (lower).

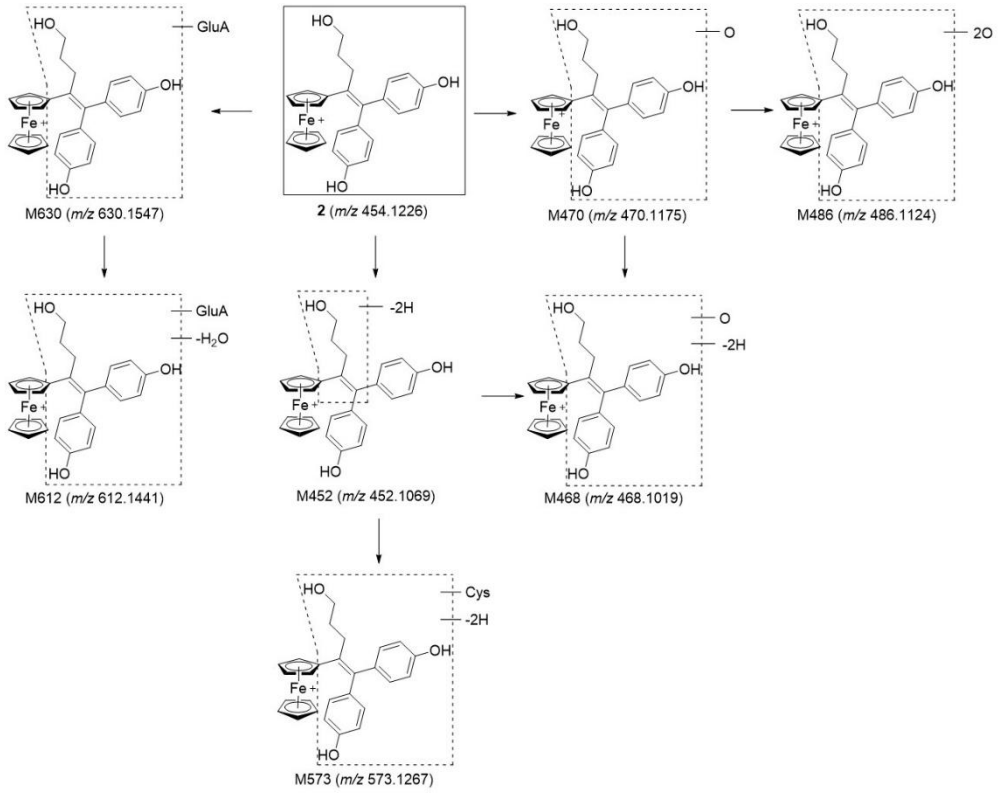

Comp.	Pathway	Rt	$[M+H]^+$ Calculated	$[M+H]^+$ Found	Plasma		Feces		Urine	
		min	m/z	m/z	MS Area	%	MS Area	%	MS Area	%
2	--	13.42	454.1226	454.1223	503362249	81.04	1641155847	45.78	147836669	86.78
M452	[-2H]	14.72	452.1069	452.1063	13934724	2.24	298030673	8.31	7651885	4.49
M468	[O]+[-2H]	13.13	468.1019	468.1011	35291338	5.68	225917903	6.30	2640966	1.55
M470	[O]	12.80	470.1157	470.1169	31363234	5.05	1173270386	32.73	11795685	6.92
M486	2[O]	12.22	486.1124	486.1120	2373784	0.38	49147601	1.37	0	0.00
M573	Cys+[-2H]	10.62	573.1267	573.1262	0	0.00	173770774	4.85	0	0.00
M612	GluA+[-H_2O]	12.23	612.1441	612.1435	0	0.00	23548688	0.66	0	0.00
M630	GluA	10.42	630.1547	630.1548	34809105	5.60	0	0.00	440672	0.26
SUM					621134434	100.00	3584841872	100.00	170365877	100.00

Fig. S10. The plausible metabolic pathways (upper) of **2** *in vivo* and the identification and MS abundance of corresponding metabolites (lower) in terms of plasma, faeces and urine characterized by LC-UV/HRMS.

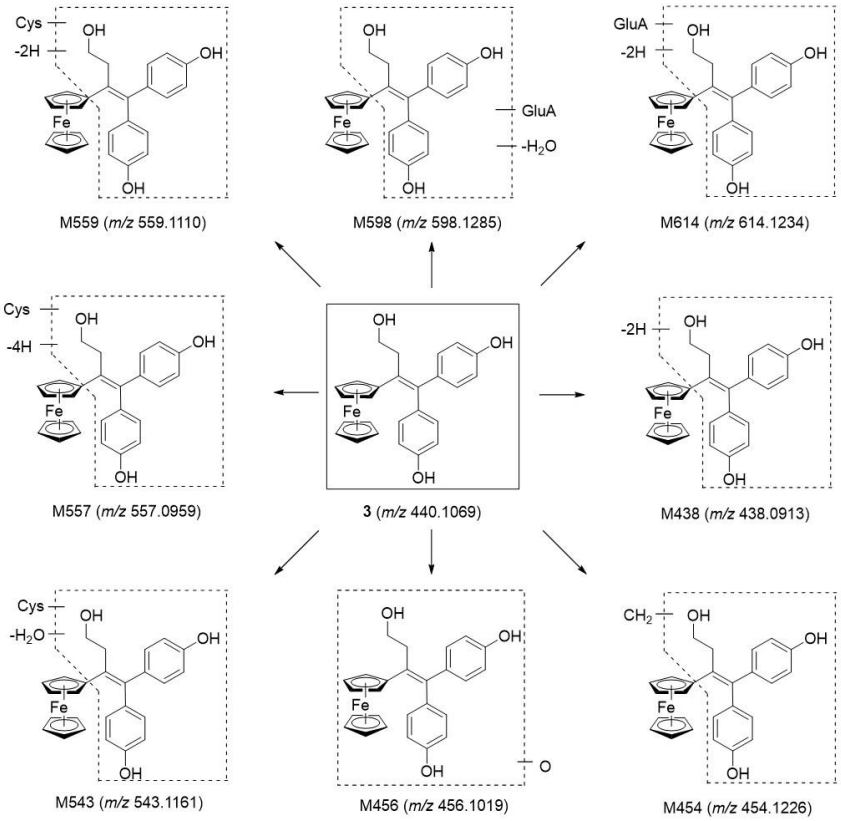

Comp.	Pathway	Rt	$[M+H]^+$ Calculated	$[M+H]^+$ Found	Plasma		Urine		Feces	
		min	m/z	m/z	MS Area	%	MS Area	%	MS Area	%
3	--	12.48	440.1069	440.1069	650953432	92.19	103710397	87.75	1287268437	75.69
M438	[-2H]	13.35	438.0913	438.0917	32338942	4.58	14479330	12.25	156188499	9.18
M454	[CH_2]	12.52	454.1226	454.1232	17419922	2.47	0	0.00	2928384	0.17
M456	[O]	12.01	456.1019	456.1018	972253	0.14	0	0.00	14404076	0.85
M543	Cys+[-H_2O]	10.72	543.1161	543.1163	0	0.00	0	0.00	9757797	0.57
M557	Cys+[-4H]	10.29	557.0959	557.0961	0	0.00	0	0.00	16731928	0.98
M559	Cys+[-2H]	10.13	559.1110	559.1111	0	0.00	0	0.00	147367737	8.66
M598	GluA+[-H_2O]	11.51	598.1285	598.1280	0	0.00	0	0.00	63939191	3.76
M614	GluA+[-2H]	11.20	614.1234	614.1234	4437616	0.63	0	0.00	2175262	0.13
SUM					706122165	100.00	118189727	100.00	1700761311	100.00

Fig. S11. The plausible metabolic pathways (upper) of **3** *in vivo* and the identification and MS abundance of corresponding metabolites (lower) in terms of plasma, faeces and urine characterized by LC-UV/HRMS.

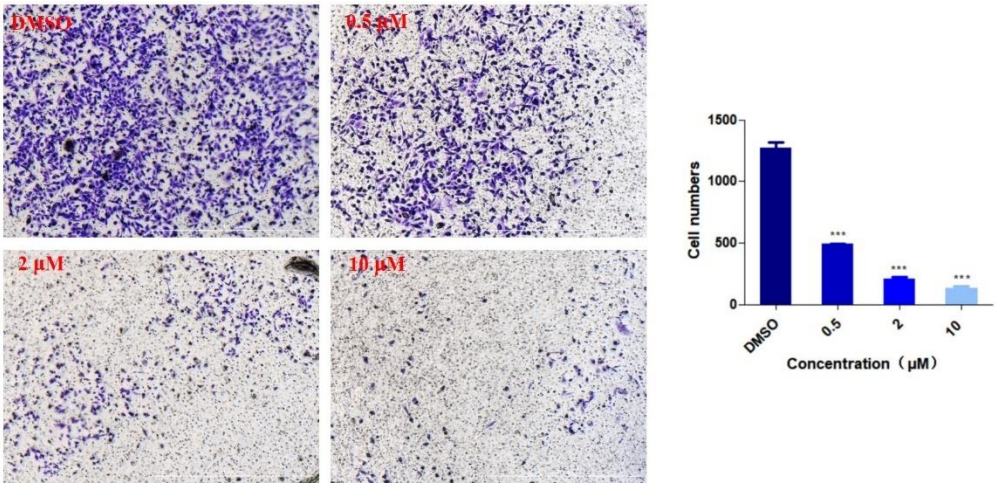

Fig. S12. Transwell assays were used to detect the invasion of cancer cells after treatment with various concentrations of **2** (0.5, 2, 10 μM). Data are presented as the mean ± SD from three independent experiments. *P < 0.05, **P < 0.01, ***P < 0.001 vs the vehicle control.

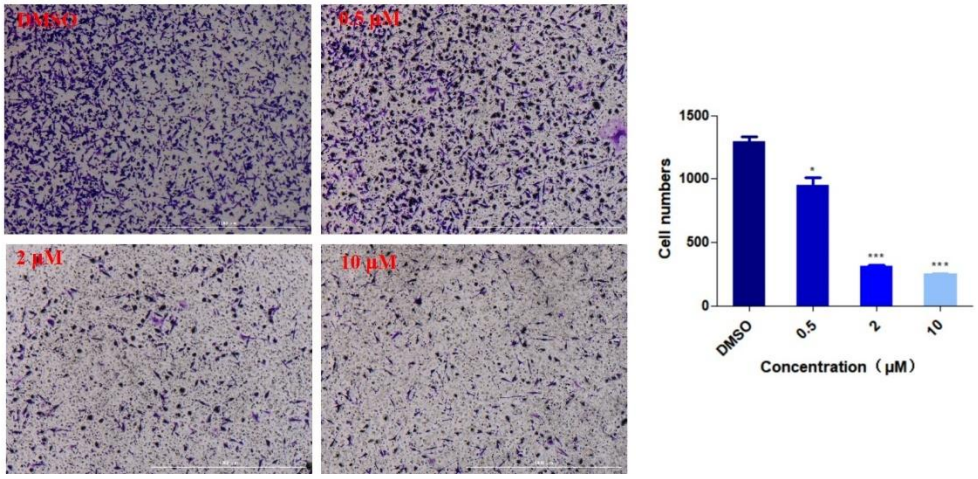

Fig. S13. Transwell assays were used to detect the invasion of cancer cells after treatment with various concentrations of **3** (0.5, 2, 10 μM). Data are presented as the mean ± SD from three independent experiments. *P < 0.05, **P < 0.01, ***P < 0.001 vs the vehicle control.

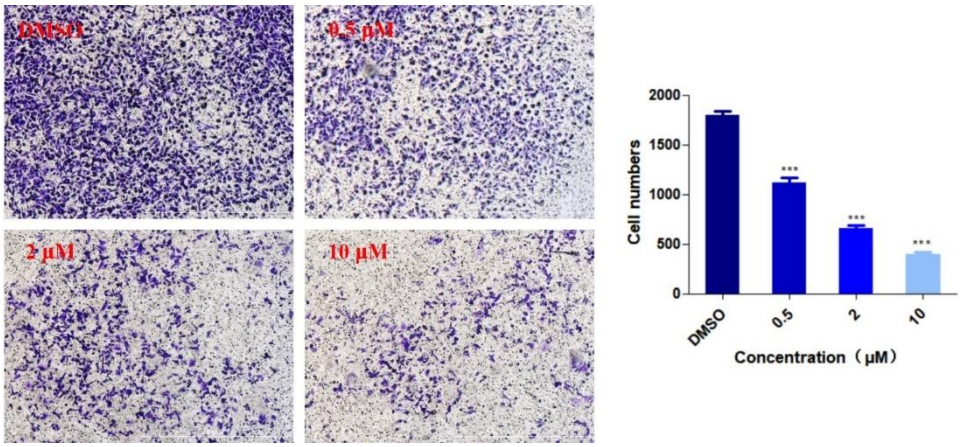

Fig. S14. Transwell assays were used to detect the invasion of cancer cells after treatment with various concentrations of **4** (0.5, 2, 10 μM). Data are presented as the mean ± SD from three independent experiments. *P < 0.05, **P < 0.01, ***P < 0.001 vs the vehicle control.

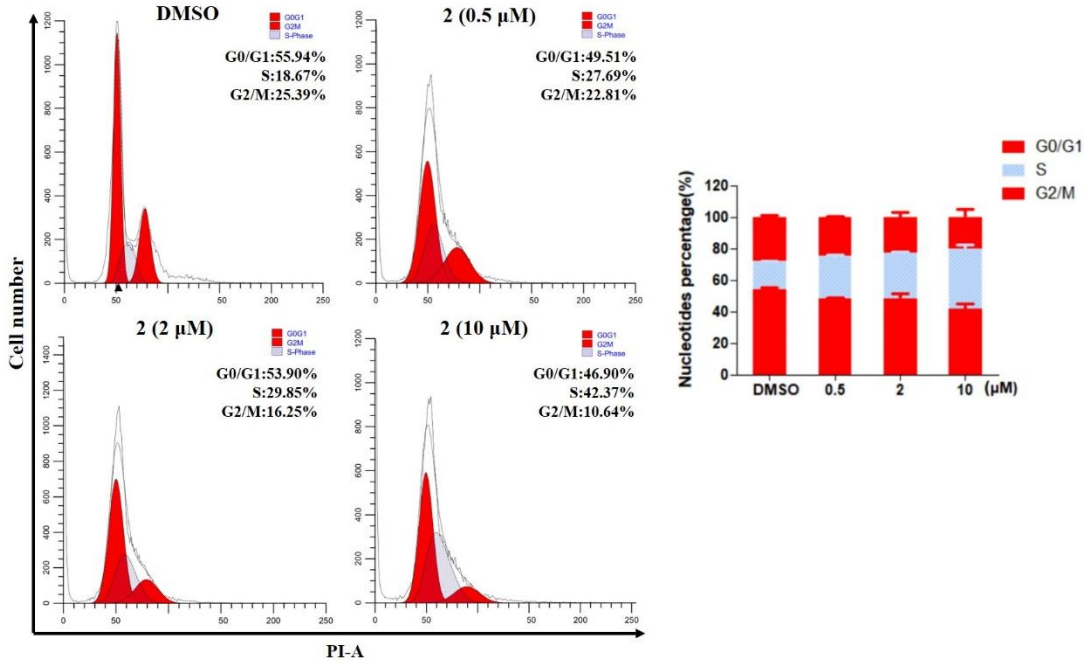

Fig. S15. Cell cycle changes of MDA-MB-231 cells after incubation with various concentrations of **2** (0.5, 2, 10 μM) for 24 h.

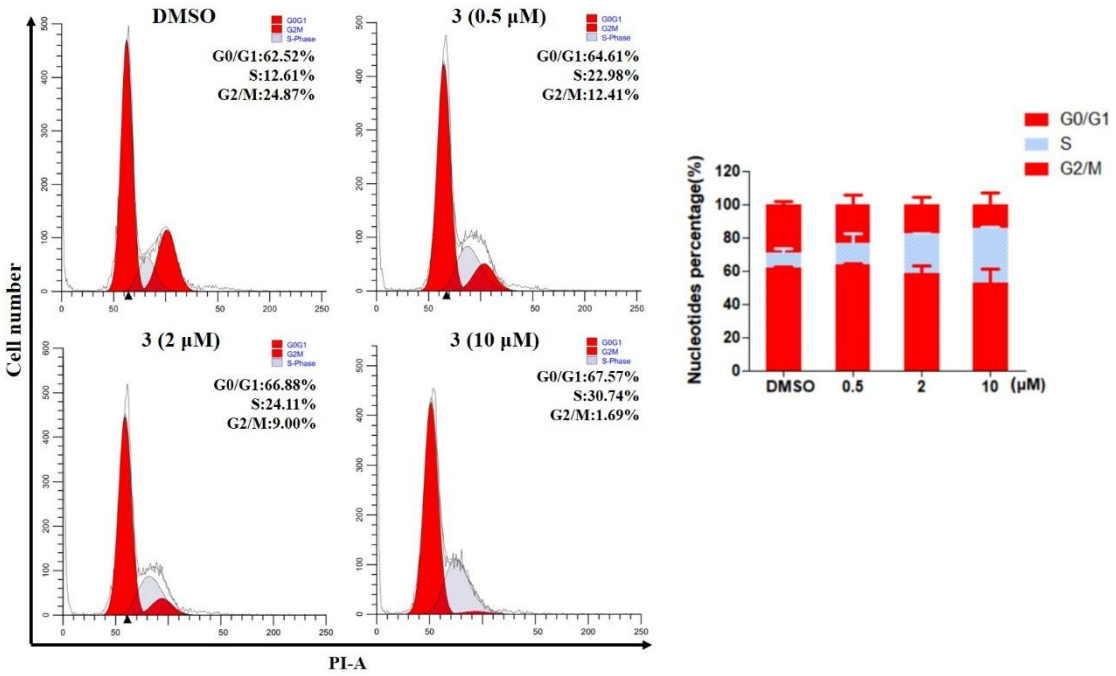

Fig. S16. Cell cycle changes of MDA-MB-231 cells after incubation with various concentrations of **3** (0.5, 2, 10 μM) for 24 h.

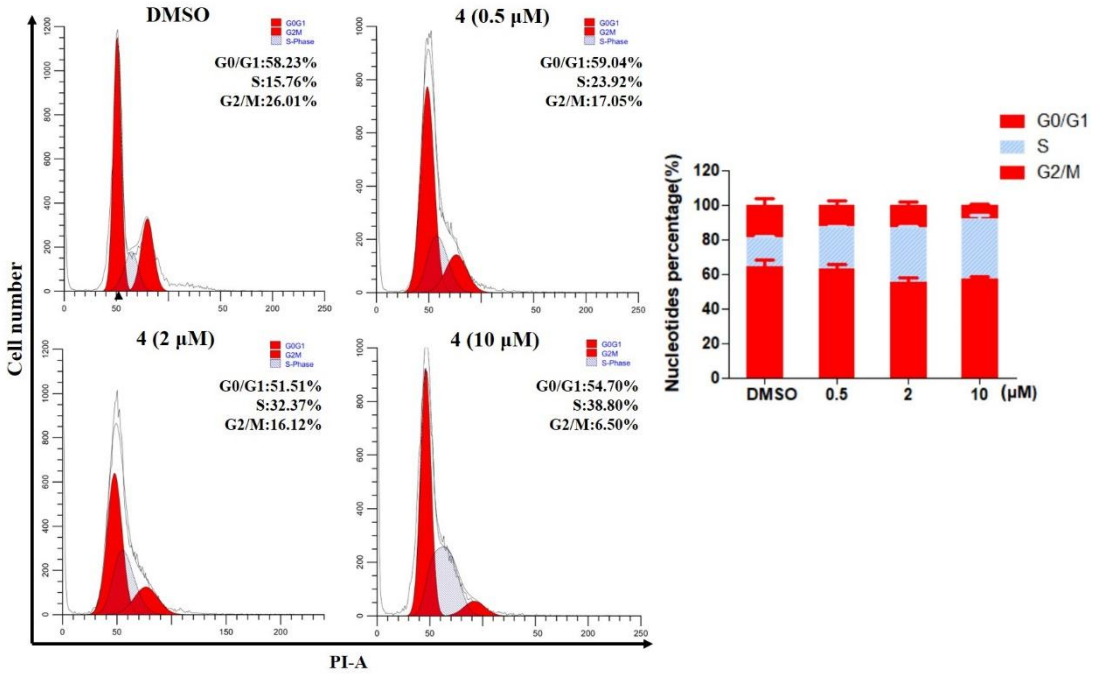

Fig. S17. Cell cycle changes of MDA-MB-231 cells after incubation with various concentrations of **4** (0.5, 2, 10 μM) for 24 h.

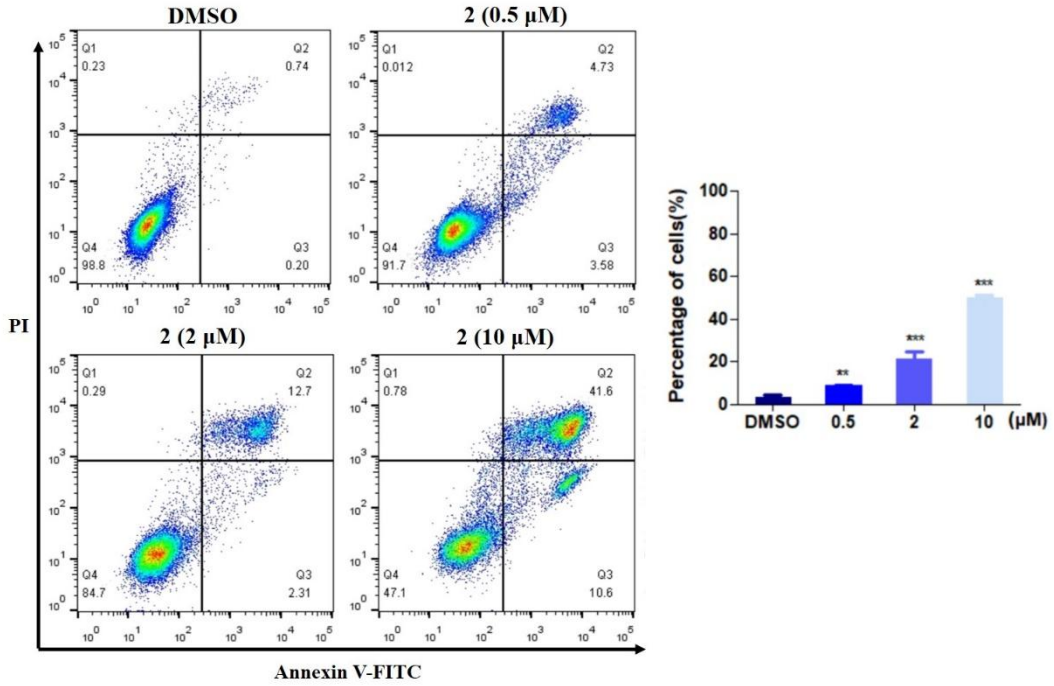

Fig. S18. Flow cytometry analysis of MDA-MB-231 cells after incubation with various concentrations of **2** (0.5, 2, 10 μM) for 24 h. Data are presented as the mean ± SD from three independent experiments. *P < 0.05, **P < 0.01, ***P < 0.001 vs the vehicle control.

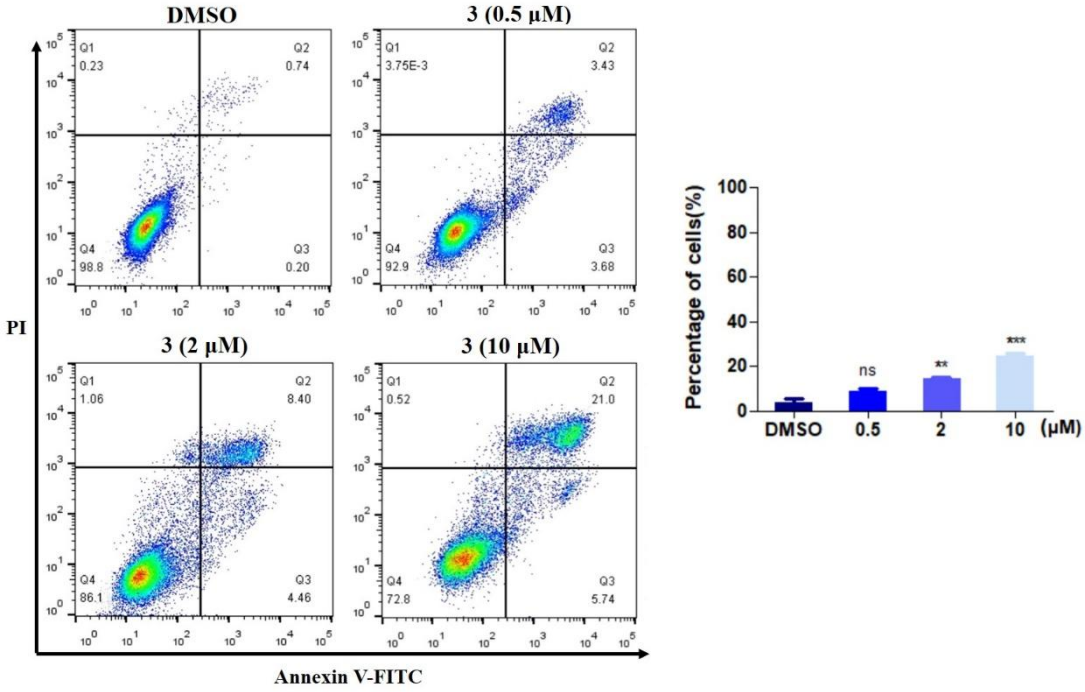

Fig. S19. Flow cytometry analysis of MDA-MB-231 cells after incubation with various concentrations of **3** (0.5, 2, 10 μM) for 24 h. Data are presented as the mean ± SD from three independent experiments. *P < 0.05, **P < 0.01, ***P < 0.001 vs the vehicle control.

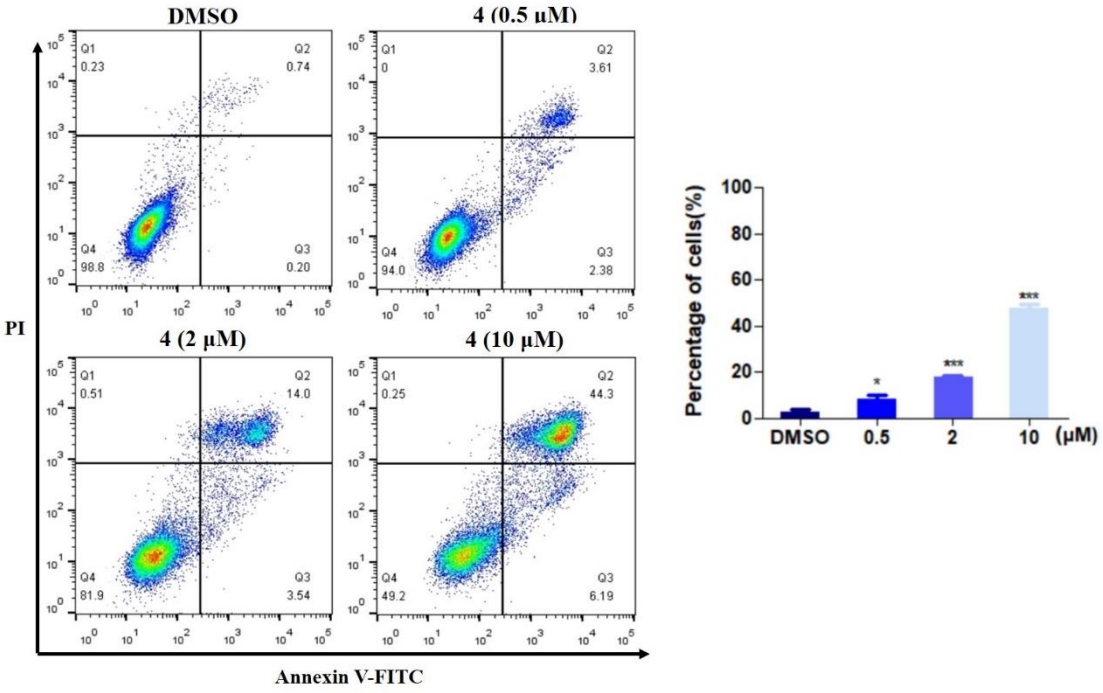

Fig. S20. Flow cytometry analysis of MDA-MB-231 cells after incubation with various concentrations of **4** (0.5, 2, 10 μM) for 24 h. Data are presented as the mean ± SD from three independent experiments. *P < 0.05, **P < 0.01, ***P < 0.001 vs the vehicle control.

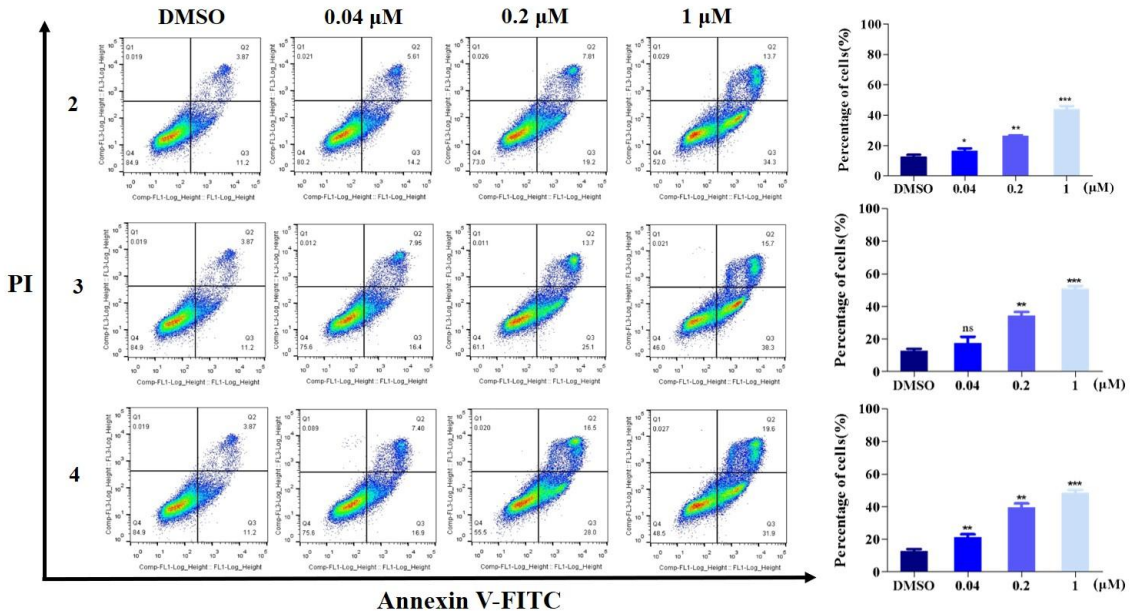

Fig. S21. Flow cytometry analysis of 4T1 cells after incubation with various concentrations (0.04, 0.2, 1 μM) of **2**, **3**, **4** for 24 h. Data are presented as the mean ± SD from three independent experiments. *P < 0.05, **P < 0.01, ***P < 0.001 vs the vehicle control.

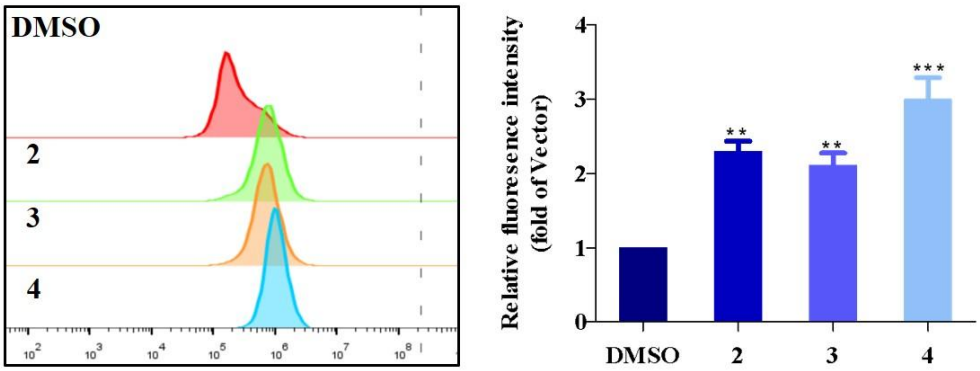

Fig. S22. Flow cytometry and its data analysis of 4T1 cells after incubation with **2**, **3**, **4** (2 μM) and DCFH-DA for 3 h.

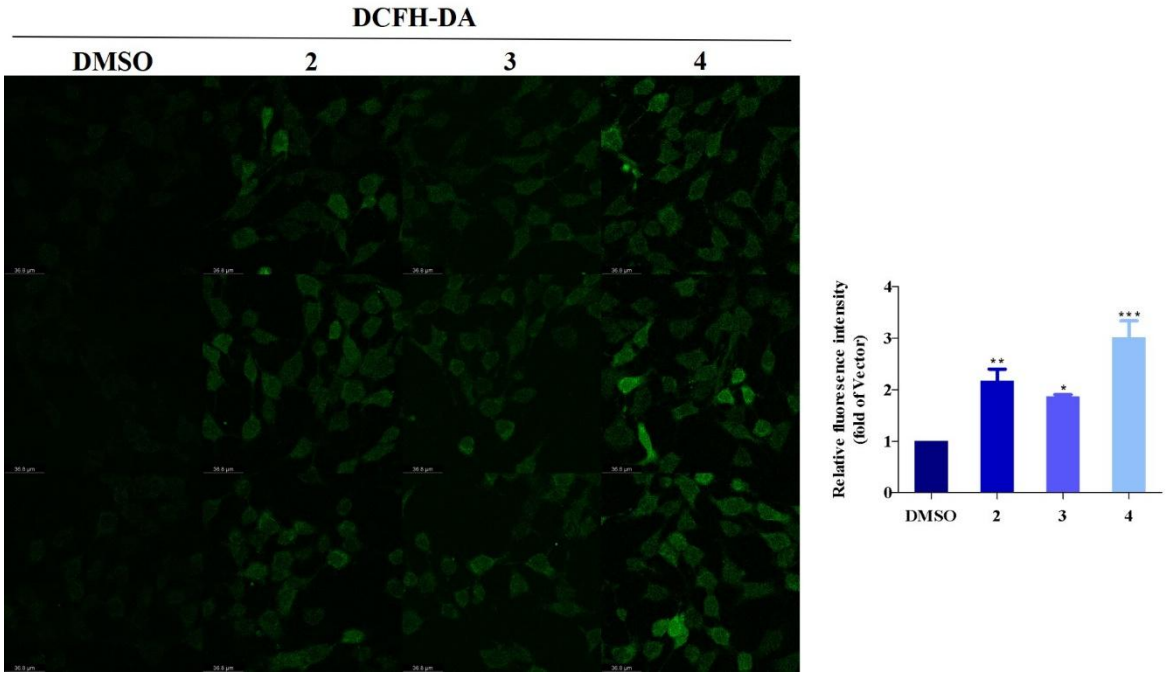

Fig. S23. Representative confocal images and its data analysis of 4T1 cells after incubation with **2**, **3**, **4** (2 μM) and DCFH-DA for 3 h.

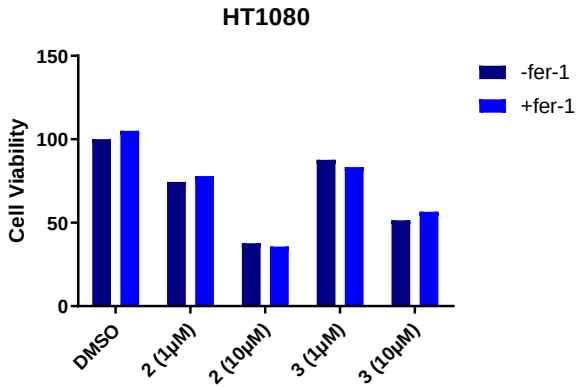

Fig. S24. Ferroptosis-inducing activity of **2** and **3** were measured on ferroptosis sensitive fibrosarcoma cells HT1080 with or without 1.5 μM fer-1.

Table S1. Crystallographic Data for the Dihydrofuran **3-A**.

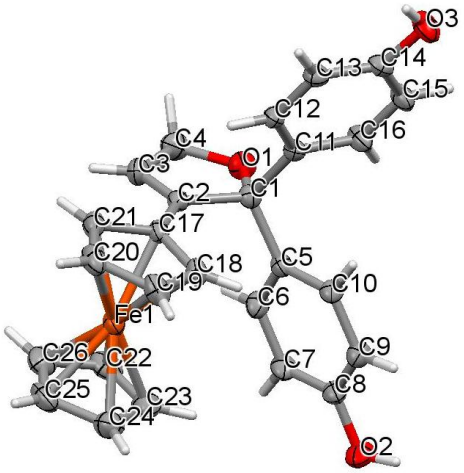

3-A

Formula	$C_{26}H_{22}FeO_3$	Selected bond lengths (Å)	
Molecular Weight	438.30	C(1)-C(2)	1.530(3)
Crystal description	Orange block	C(1)-C(11)	1.528(3)
Crystal size (mm)	0.04 x 0.06 x 0.20	C(2)-C(17)	1.468(3)
λ (Å)	1.54186	C(5)-C(10)	1.383(3)
Temperature (K)	298(2)	C(1)-O(1)	1.454(3)
Crystal system	Monoclinic	C(8)-S(2)	1.371(3)
Space group	$P2_1/n$	Fe(1)-C(17)	2.044(2)
a (Å)	13.1064(5)	Fe(1)-C(18)	2.032(3)
b (Å)	10.9009(3)	Selected Bond Angles (°)	
c (Å)	16.8834(6)	C(6)-C(5)-C(1)	118.9(2)
α (°)	90	C(12)-C(11)-C(1)	124.1(2)
β (°)	93.037(3)	C(17)-C(2)-C(3)	126.9(2)
γ (°)	90	C(11)-C(1)-C(2)	113.8(2)
Volume (Å3)	2408.77(14)	C(16)-C(11)-C(12)	116.7(2)
Z	4	C(4)-O(1)-C(1)	110.9(2)
R	0.0367	C(9)-C(8)-O(2)	121.9(3)
Rw	0.0788	C(13)-C(14)-O(3)	123.9(3)
GOF	0.821	C(18)-Fe(1)-C(17)	40.58(10)
		C(22)-Fe(1)-C(18)	122.87(13)

Table S2. Crystallographic Data for the Tetrahydrofuran **4-A**.

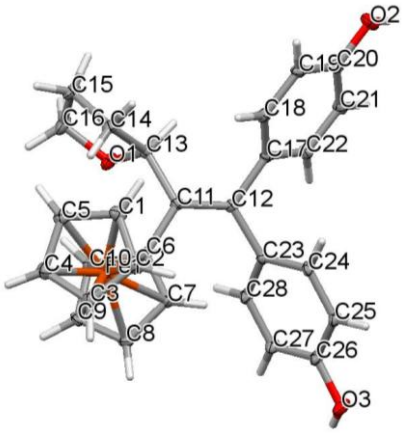

4-A

Formula	$C_{28}H_{26}FeO_3$	Selected bond lengths (Å)	
Molecular Weight	466.36	C(1)-C(2)	1.436(3)
Crystal description	Orange block	C(1)-C(5)	1.440(3)
Crystal size (mm)	0.08 x 0.11 x 0.13	C(1)-C(11)	1.478(3)
λ (Å)	0.7107	C(12)-C(19)	1.486(3)
Temperature (K)	200	C(16)-O(1)	1.356(2)
Crystal system	monoclinic	C(22)-O(2)	1.370(3)
Space group	$P2_1$	Fe(1)-C(3)	2.038(2)
a (Å)	9.9470(3)	Fe(1)-C(4)	2.047(2)
b (Å)	9.0043(3)	Selected Bond Angles (°)	
c (Å)	12.1438(4)	C(2)-C(1)-C(5)	105.92(17)
α (°)	90	C(2)-C(1)-C(11)	126.14(16)
β (°)	91.316(2)	C(1)-C(5)-C(4)	108.8(2)
γ (°)	90	C(7)-C(6)-C(10)	107.7(2)
Volume (Å3)	1087.38(6)	C(6)-C(10)-C(9)	108.45(19)
Z	2	C(1)-C(11)-C(25)	118.82(16)
R	0.0271	C(1)-C(5)-Fe(1)	71.00(11)
Rw	0.0594	C(21)-C(22)-O(2)	122.38(19)
GOF	0.9954	C(23)-C(22)-O(2)	117.37(19)
		C(1)-Fe(1)-C(8)	124.59(8)

Table S3. Crystallographic Data for Cyclohexanone by-product, **9**.

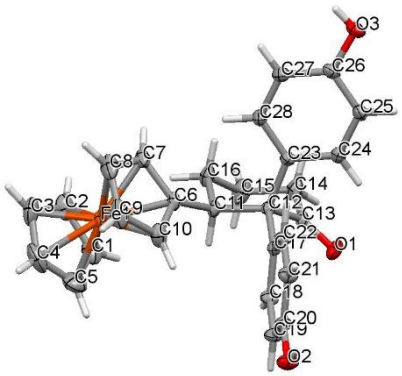

9

Formula	$C_{28}H_{26}FeO_3$	Selected bond lengths (Å)	
Molecular Weight	466.36	C(6)-C(7)	1.16(14)
Crystal description	Yellow block	C(6)-C(23)	1.73(12)
Crystal size (mm)	0.15 x 0.19 x 0.25	C(8)-C(17)	1.44(14)
λ (Å)	0.7107	C(18)-O(2)	1.04(9)
Temperature (K)	200	C(14)-O(3)	1.36(9)
Crystal system	Monoclinic	C(15)-C(19)	1.47(12)
Space group	$P2_1/c$	Fe(1)-C(20)	2.10(10)
a (Å)	11.2970(15)	Fe(1)-C(22)	2.07(16)
b (Å)	14.265(2)	Selected Bond Angles (°)	
c (Å)	15.9508(16)	C(6)-C(7)-C(9)	109.72(10)
α (°)	90	C(6)-C(7)-C(18)	106.13(9)
β (°)	93.474(9)	C(10)-C(8)-C(17)	116.70(12)
γ (°)	90	C(7)-C(9)-C(12)	122.57(11)
Volume (Å3)	2565.8(6)	C(8)-C(10)-C(25)	121.71(12)
Z	4	C(9)-C(12)-C(21)	121.67(12)
R	0.0490	C(7)-C(18)-O(2)	122.25(12)
Rw	0.0868	C(16)-C(18)-O(2)	120.38(12)
GOF	0.9546	C(6)-C(23)-Fe(1)	125.79(9)
		C(20)-C(23)- Fe(1)	68.22(8)

Chemical Synthesis

Methyl 5-ene-5-ferrocenyl-6,6-bis-(4-hydroxyphenyl)-hexanoate (7)

Titanium tetrachloride (0.812 ml, 7.39 mmol) was added dropwise to a suspension of zinc powder (0.9663 g, 14.78 mmol) in dry THF at 0 °C. The mixture was heated at reflux for 2 hours. A second solution was prepared by dissolving each ketone in dry THF: the ferrocenyl ester ketone (0.7051 g, 2.24 mmol) and the bis(4-hydroxyphenyl)methanone (1.0561 g, 4.93 mmol). This latter solution was added dropwise to the first solution and then the reflux was continued overnight. After cooling to room temperature, the mixture was acidified with conc. hydrochloric acid until dark color disappeared and was decanted. The aqueous layer was extracted with ethyl acetate and the combination of organic layers was washed with water, brine, dried on Na_2SO_4. After concentration under reduced pressure, the crude product was chromatographed on silica gel column with a mixture of petroleum ether /ethyl acetate as the eluent and was obtained in a yield 12%. ^{1}H NMR (300 MHz, DMSO-d_6): δ 1.56-1.76 (m, 2H, CH_2), 2.19 (t, J = 8.2 Hz, 2H, CH_2), 2.48-2.60 (m, 2H, CH_2), 3.53 (s, 3H, CH_3), 3.85 (t, J = 1.9 Hz, 2H, C_5H_4), 4.08 (t, J = 1.9 Hz, 2H, C_5H_4), 4.09 (s, 5H, Cp), 6.62 (d, J = 8.5 Hz, 2H, C_6H_4), 6.71 (d, J = 8.5 Hz, 2H, C_6H_4), 6.77 (d, J = 8.5 Hz, 2H, C_6H_4), 6.94 (d, J = 8.5 Hz, 2H, C_6H_4), 9.26 (s, 1H, OH), 9.30 (s, 1H, OH). ^{13}C NMR (75 MHz, DMSO-d_6): δ 25.4 (CH_2), 33.2 (CH_2), 33.4 (CH_2), 51.1 (CH_3), 67.8 (2CH C_5H_4), 68.7 (2CH C_5H_4), 68.9 (5CH Cp), 86.7 (C C_5H_4), 115.0 (2x2CH C_6H_4), 129.9 (2CH C_6H_4), 130.3 (2CH C_6H_4), 132.9 (C), 135.1 (C), 135.5 (C), 138.4 (C), 156.5 (C), 156.6 (C), 174.1 (CO). IR (KBr, ν cm^{-1}): 3420 (OH), 3028, 2948 (CH_2, CH_3), 1706, 1693 (CO). MS (CI, NH_3) m/z : 497 $[M+H]^+$, 514 $[M+NH_4]^+$. HRMS (CI, NH_3, $C_{29}H_{29}FeO_4$: $[M+H]^+$) calcd: 497.1416, found: 497.1430. Anal. Calcd for $C_{29}H_{28}FeO_4$: C, 70.17; H, 5.68. Found: C, 69.96; H, 5.71.

Methyl 6-ene-6-ferrocenyl-7,7-bis-(4-hydroxyphenyl)-heptanoate (8)

Titanium tetrachloride (1.04 ml, 9.44 mmol) was added dropwise to a suspension of zinc powder (1.234 g, 18.88 mmol) in dry THF at 0 °C. The mixture was heated at reflux for 2 hours. A second solution was prepared by dissolving each ketone in dry THF: the ferrocenyl ester ketone (0.9398 g, 2.86 mmol) and the bis(4-hydroxyphenyl)methanone (1.35 g, 6.30 mmol). This latter solution was added dropwise to the first solution and then the reflux was continued overnight. After cooling to room temperature, the mixture was acidified with conc. hydrochloric acid until dark color disappeared and was decanted. The aqueous layer was extracted with ethyl acetate and the combination of organic layers was washed with water,

brine, dried on Na_2SO_4. After concentration under reduced pressure, the crude product was chromatographed on silica gel column with a mixture of petroleum ether/ethyl acetate as the eluent and was obtained in a yield 39 %. ^{1}H NMR (300 MHz, acetone-d_6): δ 1.46-1.56 (m, 4H, CH_2), 2.13-2.21 (m, 2H, CH_2), 2.57-2.67 (m, 2H, CH_2), 3.59 (s, 3H, CH_3), 3.90-3.96 (m, 2H, C_5H_4), 4.04-4.08 (m, 2H, C_5H_4), 4.13 (s, 5H, Cp), 6.70 (d, *J* = 8.7 Hz, 2H, C_6H_4), 6.81 (d, *J* = 8.7 Hz, 2H, C_6H_4), 6.86 (d, *J* = 8.7 Hz, 2H, C_6H_4), 7.04 (d, *J* = 8.7 Hz, 2H, C_6H_4), 8.19 (s, 1H, OH), 8.23 (s, 1H, OH). ^{13}C NMR (75 MHz, acetone-d_6): δ 25.7 (CH_2), 30.9 (CH_2), 34.0 (CH_2), 35.1 (CH_2), 51.5 (CH_3), 68.7 (2CH C_5H_4), 69.9 (5CH Cp), 70.0 (2CH C_5H_4), 88.6 (C C_5H_4), 115.76 (2CH C_6H_4), 115.83 (2CH C_6H_4), 131.3 (2CH C_6H_4), 131.8 (2CH C_6H_4), 135.0 (C), 137.1 (C), 137.4 (C), 139.3 (C), 156.63 (C), 156.71 (C), 174.0 (CO). MS (ESI) m/z : 510 $[M]^{+\cdot}$, 271, 143, 83. HRMS (ESI, $C_{30}H_{30}FeO_4$: $[M]^{+\cdot}$) calcd: 510.1493, found: 510.1509. Purity: 98.33%.

3-Ferrocenyl-2,2-bis(4-hydroxyphenyl)-cyclohexan-one (9)

This compound was obtained as a by-product during the synthesis of **7**, in 66% yield. ^{1}H NMR (300 MHz, DMSO-d_6): δ 1.94-2.54 (m, 6H, CH_2-CH_2-CH_2), 2.74 (s broad, 1H, C_5H_4), 3.70-3.80 (m, 1H, CH), 3.83 (s broad, 1H, C_5H_4), 4.00 (s broad, 1H, C_5H_4), 4.04 (s, 5H, Cp), 4.28 (s broad, 1H, C_5H_4), 6.51-6.69 (m, 6H, C_6H_4), 6.82 (d, *J* = 8.5 Hz, 2H, C_6H_4), 9.23 (s, 1H, OH), 9.34 (s, 1H, OH). ^{13}C NMR (75 MHz, DMSO-d_6): δ 24.8 (CH_2), 26.8 (CH_2), 39.3 (CH_2), 48.4 (CH), 66.1 (CH C_5H_4), 67.1 (CH C_5H_4), 67.4 (C), 68.6 (5CH Cp+CH C_5H_4), 68.9 (CH C_5H_4), 89.6 (C C_5H_4), 113.9 (2CH C_6H_4), 114.9 (2CH C_6H_4), 129.4 (C), 130.4 (2CH C_6H_4), 131.2 (2CH C_6H_4), 134.7 (C), 155.6 (C), 157.8 (C), 210.5 (CO). IR (KBr, ν cm^{-1}): 3474, 3278 (OH), 1703 (CO). MS (CI, NH_3) m/z : 467 $[M+H]^+$, 484 $[M+NH_4]^+$, 449 $[M+H-H_2O]^+$. HRMS (CI, NH_3, $C_{28}H_{27}FeO_3$: $[M+H]^+$) calcd: 467.1310, found: 467.1303.

X-ray crystal structure determinations for 3-A, 4-A and the Cyclohexanone byproduct 9.

A single crystal of each compound was selected, mounted onto a cryoloop and transferred into a cold nitrogen gas stream. Intensity data were collected with a Bruker Kappa-APEXII diffractometer using graphite-monochromated Mo-Kα radiation (λ = 0.71073 Å). Data collection was performed with the Bruker APEXII suite. Unit-cell parameters determination, integration and data reduction were carried out with SAINT program. SADABS was used for scaling and absorption corrections. The structures were solved with SHELXT-2014[2] and refined by full-matrix least-squares methods with SHELXL-2014[3] using the WinGX suite[4] or Olex2 software package[5]. All non-hydrogen atoms were refined anisotropically. The

structures were deposited at the Cambridge Crystallographic Data Centre with numbers CCDC 221630, 2218360, 2218361 and can be obtained free of charge via www.ccdc.cam.ac.uk.

Electrochemical oxidation of 2, 3, 4 and 5

Cyclic voltammograms (CVs) were obtained using a three-electrode cell with a 0.5 mm Pt working electrode, stainless steel rod counter electrode, and Ag/AgCl ethanol reference electrode, with an μ-Autolab 3 potentiostat driven by GPES software (General Purpose Electrochemical System, Version 4.8, EcoChemie B.V., Utrecht, the Netherlands). Solutions consisted of 5 mL CH_3CN, approximately 1 mM analyte, and 0.1 M Bu_4NPF_6 supporting electrolyte. Scan rate of CVs was 200 mV/s.

Lipophilicity

Measurements of the octanol/water partition coefficient (log Po/w) were made by the HPLC technique. Measurement of the chromatographic capacity factors (k) for each molecule was done at various concentrations in the range of 95–75% methanol containing 0.25% (v/v) 1-octanol and an aqueous phase consisting of 0.15% (v/v) n-decylamine in the buffering agent MOPS (3-morpholinopropane-1-sulfonic acid, prepared in 1-octanol saturated water) adjusted to pH 7.4. These capacity factors (k′) are extrapolated to 100% of the aqueous component given the value of k′w. The log Po/w is obtained by the formula log Po/w = 0.13418 + 0.98452 log k′.

Incubation in rat liver microsomes and analytical conditions

Rat liver microsomes (RLMs, 0.8645 nmole P450 /mg protein) were pooled with 10 males (200-250 g). In stability assay, incubation samples of 2 μM of different compounds in 200 μL with NADPH-regenerating system (1.1m M β-nicotinamide adenine dinucleotide phosphate, 11 mM glucose 6-phosphate, and 1 U/mL glucose-6-phosphate dehydrogenase) in 50 mM Tris-HCl buffer (pH 7.4) containing RLMs (final protein concentration 0.2 mg/mL) were placed in water bath at 37 °C. All samples were quenched with two volumes of acetonitrile containing IS (compound **1** or compound **4**, 200 ng/mL) at 2, 5, 10, 15 min and then vortex-mixed and centrifuged at 18,880 g for 10 min. To identify the metabolites of ferrociphenols, incubation with compounds at 100 μM in buffer containing 1.3 mg protein /mL thus 1.13 μM P450 were performed for 30 min at 37°C. The supernatant was subjected to LC−MS/MS analysis. The results were expressed as the percentage of the concentration at 0 min. Concomitantly, the NADPH-free incubations were performed as the control. The halflife ($t_{1/2}$)

were calculated using a nonlinear regression (curve fit) program based on the one phase decay (GraphPad Prism 9.4; GraphPad Software Inc., San Diego, CA).

For quantification, the LC−MS/MS instrument (Waters, MA, USA) consisted of a H-Class PLUS UPLC system and Xevo TQ-XS triple quadrupole mass spectrometer with Masslynx 4.2 software for data acquisition and processing. The analytical column used was an Acquity UPLC BEH C18 column (2.1×50 mm, 1.7 μm; Waters, MA, USA) with a C18 Vanguard pre-column (2.1×5 mm, 1.7 μm; Waters, MA, USA). A 2 μl aliquot of each supernatant was injected into the UPLC–MS/MS system for quantitative analysis. Both the column oven and autosampler were maintained at room temperature. The mobile phase consisted of solvent A (0.1% formic acid in acetonitrile) and solvent B (0.1% formic acid in water). The gradient elution was performed at a flow rate of 0.3 mL/min with the following gradient conditions: 0–0.5 min, 30% solvent A; 0.5–1.5 min, 30–100% solvent A; 1.5–1.8 min, 100–30% solvent A; 1.8–4.0 min, 30% solvent A. The total run time was 4.0 min. An ESI source was used in the positive-ion mode. The optimized parameters were as follows: capillary voltage, 1.60 kV; desolvation temperature, 500 °C, desolvation gas, 1000 L/h; cone gas, 150 L/h, collision gas, 0.15 mL/min. The transitions and corresponding cone voltages and collision voltages were optimized as follows: m/z 454.1055>286.1123 (4V, 34V) for compound **2**, m/z 440.0117>343.1379 (38V, 38V) for compound **3**, m/z 469.1466>145.0138 (16V, 20V) for compound **4**, m/z 483.1766>417.1877 (18V, 30V) for compound **5**.

For metabolite profiling, 5 μL of supernatant was injected and analyzed using an Agilent UPLC 1290 plus LTQ Orbitrap XL mass spectrometer system (Thermo Fischer Scientific, MA, USA). The chromatography was carried out on an ACQUITY UPLC BEH C_{18} column (2.1 × 100 mm, 1.7 μm, Waters, MA, USA) at room temperature. The mobile phase consisted of solvent A (0.1% formic acid in acetonitrile) and solvent B (0.1% formic acid in water). A gradient elution was applied by setting solvent A at 10% for 1 min, then increasing to 100% for the next 19 min and keeping for 1 min, followed by reequilibration at 10% through 4 min. The flow rate was set at 0.25 mL/min. An ESI source was used in positive mode. The parameters were set as follows: spray voltage, 4.0 kV; capillary temperature, 300 °C; sheath gas, 40 arb; auxiliary gas, 10 arb; tube Lens voltage, 35 V. Data acquisition was performed in full-scan mode with data-dependent MS/MS mode in m/z 200–1000 Da. Data were analyzed using OpenLab CDS ChemStation Edition (Agilent, MA, USA) and Xcalibur 2.2 software (Thermo Fischer Scientific, MA, USA).

Incubation in rat hepatocytes and analytical conditions

In vitro incubation experiments in rat hepatocytes have been done by XenoFinder Co., Ltd. Cells were thawed in and washed with Williams' E Medium, penicillin/streptomycin (1%) and FBS (5%) and centrifuged at 55×g for 3 min at room temperature. After centrifugation and removal of the supernatant, the cell pellet was resuspended in Williams' E Medium with FBS (5%). About 2 μL of compounds (1 mM) was incubated in 198 μL of rat hepatocytes ($1.0*10^6$ cells/mL) suspension at 37 ℃ for 3 h in an incubator. After incubation, the samples were taken out and terminated by cold acetonitrile. For 0 h samples, rat hepatocyte and cold acetonitrile was added first. The supernatants of the samples were collected after centrifugation (15000 g, 10 min, 4 ℃), and the supernatants were evaporated with nitrogen and re-dissolved with 200 μL of solvent (ACN:H_2O = 20:80, v/v). After centrifugation (15000 g, 10 min, 4℃), the supernatants were transferred into HPLC sample bottles for LC-UV/HRMS analysis. UHPLC-UV-Q Exactive Plus MS (LC-UV/HRMS) were optimized using standard compounds as reference before final metabolites detection and identification.

Pharmacokinetc study and metabolites analysis in vivo

Pharmacokinetic studies and metabolites profiling were performed at XenoFinder Co., Ltd., which is in accordance with <Guidance for Nonclinical Pharmacokinetics of Medicinal Products> issued by National Medical Products Administration and all applicable Standard Operation Procedures (SOP) at the XenoFinder Co., Ltd. The animal testing process complies with the requirements of Institute Animal Care and Use Committee (IACUC) for animal welfare. Male Sprague-Dawley (SD) rats (weighing 200 - 300 g) were acclimated for 2-5 days prior to the study on a 12 h light/12 h dark cycle at 22 ± 2 ℃, 60% relative humidity. They were allowed free access to water and chow diet.

Rats were given **2** (30.0 mg/kg) through the tail vein . The dosing solutions were prepared by dissolving in solvent consists of 2% DMSO, 10% PEG400 and 88% normal saline. Blood samples were collected into heparinized centrifuge tubes via jugular vein sampling under isoflurane anesthesia before dosing and at 0.083, 0.25, 0.5, 1, 2, 4, 6, 8, and 24 h after intravenous injection. Plasma was separated by centrifuging the blood samples at 5000 rpm for 10 min. Besides, rats (n=3) were kept in the metabolic cages with free access to water and food. Urine was collected before dosing and at 0–8, 8–24, and 24–48 h after dosing, as well as the feces before dosing and at 0–24, and 24–48 h, simultaneously. Weigh and record the combined urine and feces samples. All samples were stored at -20 °C until analysis .

Plasma (20.0 μL) were added to 20.0 μL internal standard (IS, EZL or SLFS/BDN, final concentration 100 ng/mL) solution and 200 μL acetonitrile. All mixtures were vortexed and centrifuged at 3900 rpm for 10 min at 4 °C. A mixture of 50.0 μL aliquot of each supernatant and 150 μL water was injected into the LC-MS/MS system for pharmacokinetc analysis. For metabolites analysis, after centrifugation, the supernatants were transferred into HPLC sample bottles for LC-UV/HRMS analysis. UHPLC-UV-Q Exactive Plus MS (LC-UV/HRMS) were optimized using standard compounds as reference before final metabolites detection and identification.

Culture cells and proliferation assay. Stock solutions (10 mM) of the compounds to be tested were prepared in DMSO and were kept at -20°C in the dark. Serial dilutions in Dulbecco's modified eagle medium (DMEM) without phenol red/Glutamax I were prepared just prior to use. DMEM without phenol red, Glutamax I and fetal bovine serum were purchased from Gibco; MDA-MB-231 cells were obtained from ATCC (Manassas, VA, USA). Cells were maintained in a monolayer culture in DMEM with phenol red/Glutamax I supplemented with 9% fetal bovine serum at 37°C in a 5% CO_2/air-humidified incubator. For proliferation assays, MDA-MB-231 cells were plated in 1 mL of DMEM without phenol red, supplemented with 9% decomplemented and hormone-depleted fetal bovine serum, 1% kanamycin, 1% Glutamax I and incubated. The following day (D0), 1 mL of the same medium containing the compounds to be tested was added to the plates. After 3 days (D3) the incubation medium was removed and 2 mL of the fresh medium containing the compounds was added. At different days (D4, D5), the protein content of each well was quantified by methylene blue staining as follows: cell monolayers were fixed for 1 h at room temperature with methylene blue (1mg mL-1 in 50:50 water/MeOH mixture), then washed with water. After addition of HCl (0.1 M, 2 mL), the plate was incubated for 1 h at 37 °C and then the absorbance of each well (4 wells for each concentration) was measured at 655 nm with a Biorad spectrophotometer. The results are expressed as the percentage of proteins versus the control. Two independent experiments, run in quadruplicate, were performed.

Human colorectal carcinoma HCT-116 cells, mouse 4T1 cells and leukemia K562 cells were grown in RPMI 1640 supplemented with 10% fetal calf serum (FCS) and 1% glutamine. MCF-7, A-375, HT1080 carcinoma cells and MCF-10A were grown in Gibco medium DMEM supplemented with 10% fetal calf serum (FCS) and 1% glutamine. Cells were maintained at 37 °C in a humidified atmosphere containing 5% CO_2. Cell growth inhibition was determined by an CCK-8 assay according to the manufacturer's instructions (Promega,

Madison, WI, USA). Briefly, the cells were seeded in 96-well plates (2.5×10^3 cells/well) containing 100 μL of growth medium. After 24 h of culture, the cells were treated with the tested compounds at 8 different final concentrations. After 48 h of incubation, 10 μL of CCK-8 stock solution was added for 2 h before recording absorbance at 450 nm with a spectrophotometric plate reader. The dose-response curves were plotted with Graph Prism software and the IC_{50} values were calculated using the Graph Prism software from polynomial curves (four or five-parameter logistic equations).

Colony-formation assay. For colony-formation assays, 6-well plates were seeded with 500 cells per well, and the cells were cultured with different concentrations of **2**, **3**, **4** (0.01, 0.1, 1 μM) for approximately two weeks. Four percent paraformaldehyde (Biosharp, Anhui, China) was used to fix the colonies, and 0.1% crystal violet (G1063, Solarbio, Beijing) was used for staining. Then, representative colonies were captured and quantified.

Wound-healing assay. A P10 pipette tip was used to scrape the cells in 96-well plates to produce wounds. Medium containing only 1% FBS was used to culture the cells to exclude the effect of cell proliferation. After the cells were treated with different concentrations of **2**, **3**, **4** (2 μM), the wound area was photographed at 0 h, 12 h, and 36 h. Representative boundaries of the wound were drawn with lines.

Transwell assay. Transwell chambers and polycarbonate membranes coated with Matrigel (R&D, USA) were used to perform the Transwell assay. The cells treated with different concentrations of **2**, **3**, **4** (0.5, 2, 10 μM) were seeded in the upper chamber with 200 μl of medium with 5% FBS, and 500 μl of medium with 20% FBS was added into the lower chamber as a chemoattractant. After incubation of the cells in an incubator at 37 °C for 24 h and fixation with 4% paraformaldehyde, 0.1% crystal violet was used to stain the cells on the lower side of the Transwell chamber. An inverted microscope (Olympus BX51, Japan) was used to take the image and record the cell number.

Cell cycle assay. The cell cycle was detected by flow cytometry (ACEN; NovoCyte, San Diego, California, USA). MDA-MB-231 cells were incubated with different concentrations of **2**, **3**, **4** (0.5, 2, 10 μM) for 24 h. After 24 h, the cells were collected and centrifuged at 1200 r for 5 min. Then the cells were fixed with 2 ml 95% ethanol and incubated at -20 °C for 12 h. At the end of incubation, the cells were centrifuged at 1200 rpm for 5 min. Then, the cells were washed with 1 mL PBS and were resuspended in 400 μL PBS. The cells were incubated

with 4 μL PI solution and 4 μL RNase A(10 mg/mL PI, 1 mg/mL RNase A) at 37°C for 30 min in the dark. The content of DNA of cell cycle was measured by flow cytometry.

Cell apoptosis assay. MDA-MB-231 cells or 4T1 cells were seeded in 6-well plates at a density of 3×10^5 and allowed to attach for 24 h. Then, the cells treated with 0.5, 2, 10 μM of compound **2**, **3**, **4** for 24 h were stained with annexin V-FITC and propidium iodide, followed by analysis with flow cytometry. Percentages of cells in each group were quantified by the FlowJo software.

Western blot analysis. Cells were lysed to obtain processed protein. Then, we separated the processed proteins by SDS–PAGE and transferred them to a PVDF membrane (Millipore, Germany). After the PVDF membrane was blocked, the membrane was successively incubated with the diluted primary antibody solution and the secondary antibody (Proteintech, Wuhan, China). Membranes were imaged with Imaging Systems. The relative protein level was normalized to β-tubulin.

References

(1) W. Tagaki in *Organic Chemistry of Sulfur* (Ed. S. Oae), Plenum Press, New York, 1977, P. 246.

(2) D. Hamels, P. M. Dansette, E. A. Hillard, S. Top, A. Vessieres, P. Herson, G. Jaouen, D. Mansuy, *Angew. Chem. Int. Ed.* **2009**, *48*, 9124-9126.

(3) D. Y. Curtin, R. J. Harder, *J. Am. Chem. Soc.* **1960**, *82*, 2357-2368.

(4) R. H. Blessing, *Acta Cryst. A* **1995**, *51*, 33.

(5) P. W. Betteridge, J. R. Carruthers, R. I. Cooper, K. Prout, D. J. Watkin, *J. Appl. Crystallogr.* **2003**, *36*, 1487.

(6) P. W. Fan, F. Zhang, J. L. Bolton, *Chem. Res. Toxicol.* **2000**, *13*, 45-52.

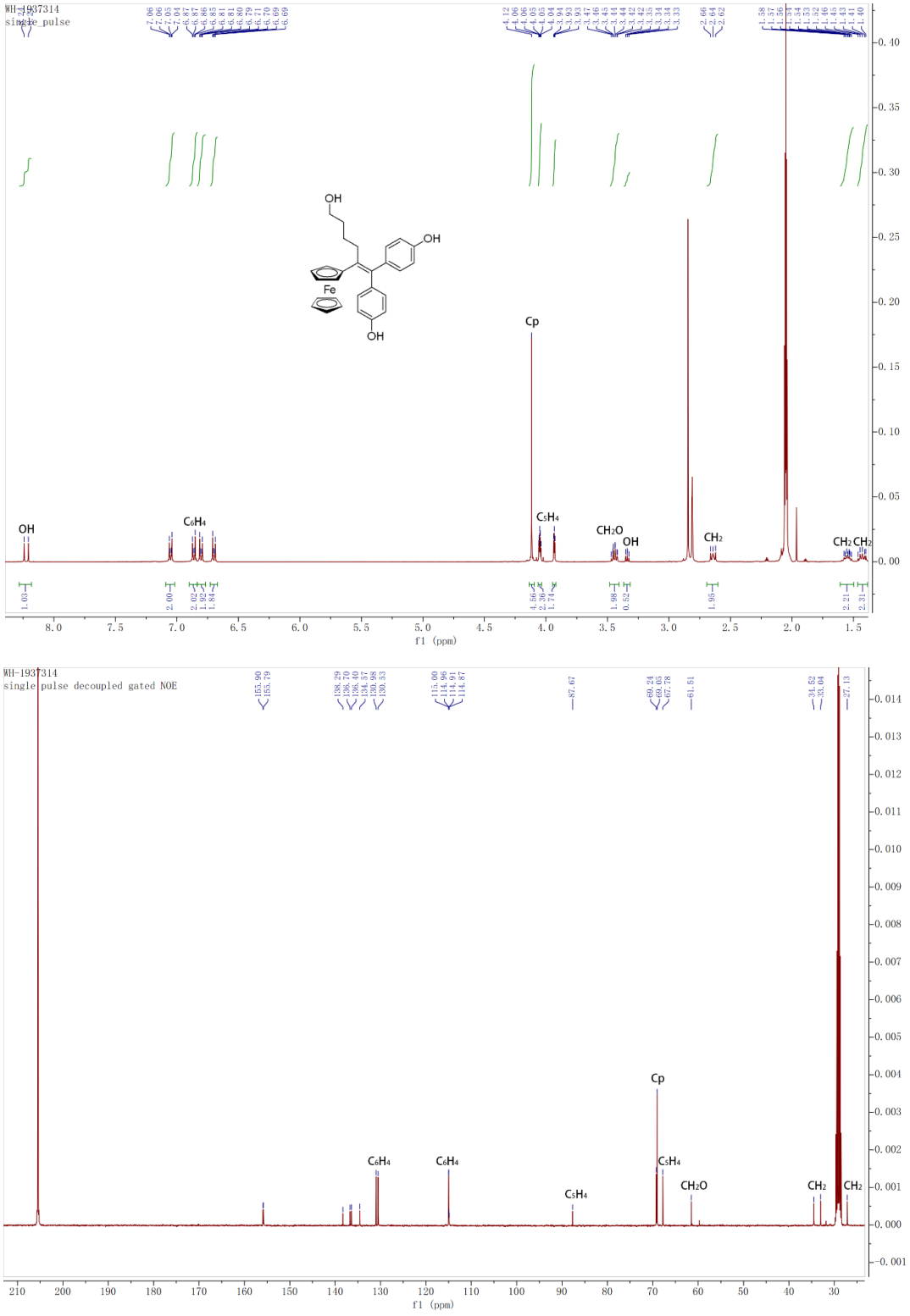

^{1}H and ^{13}C NMR spectrum of compound **4**

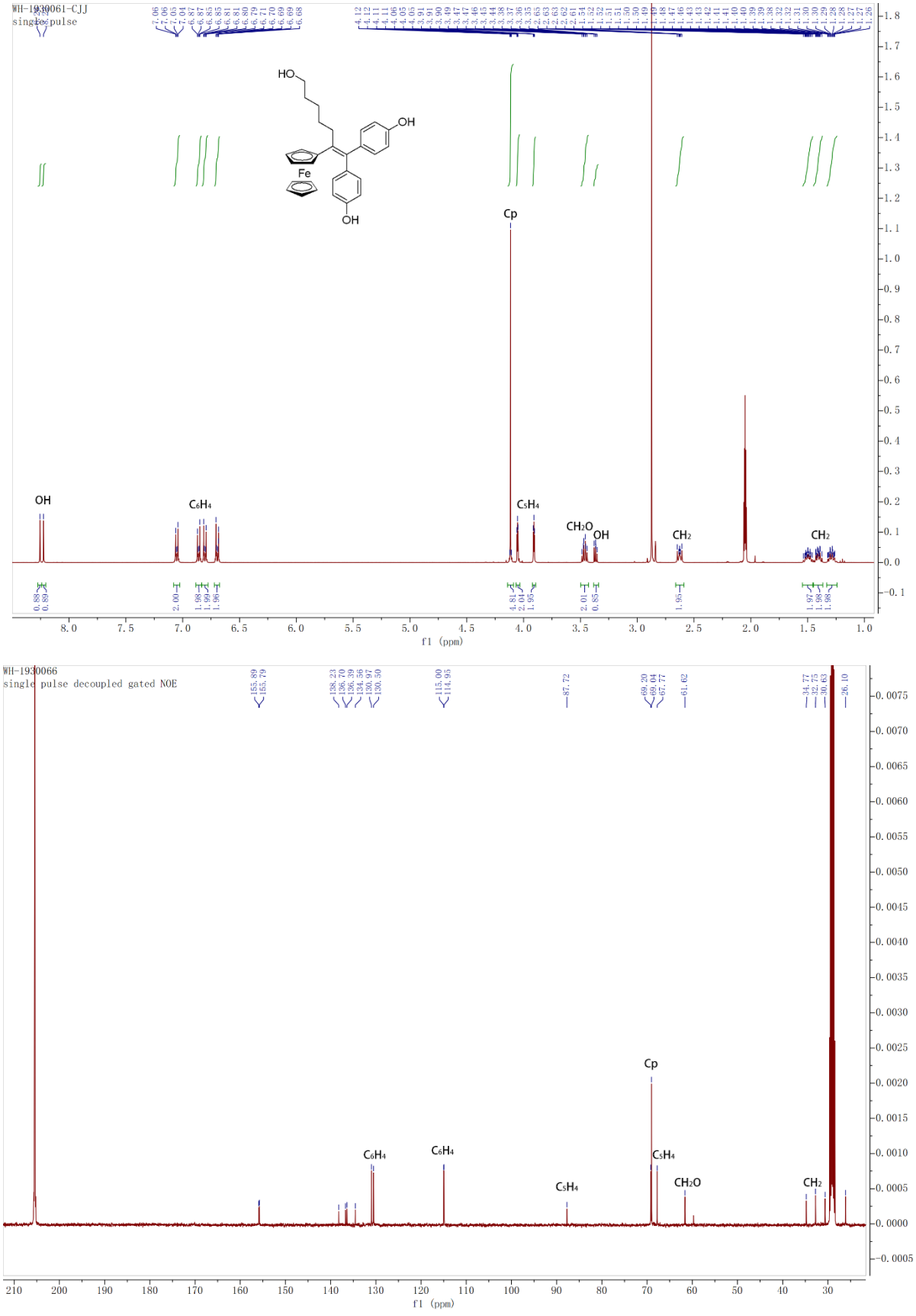

^{1}H and ^{13}C NMR spectrum of compound **5**

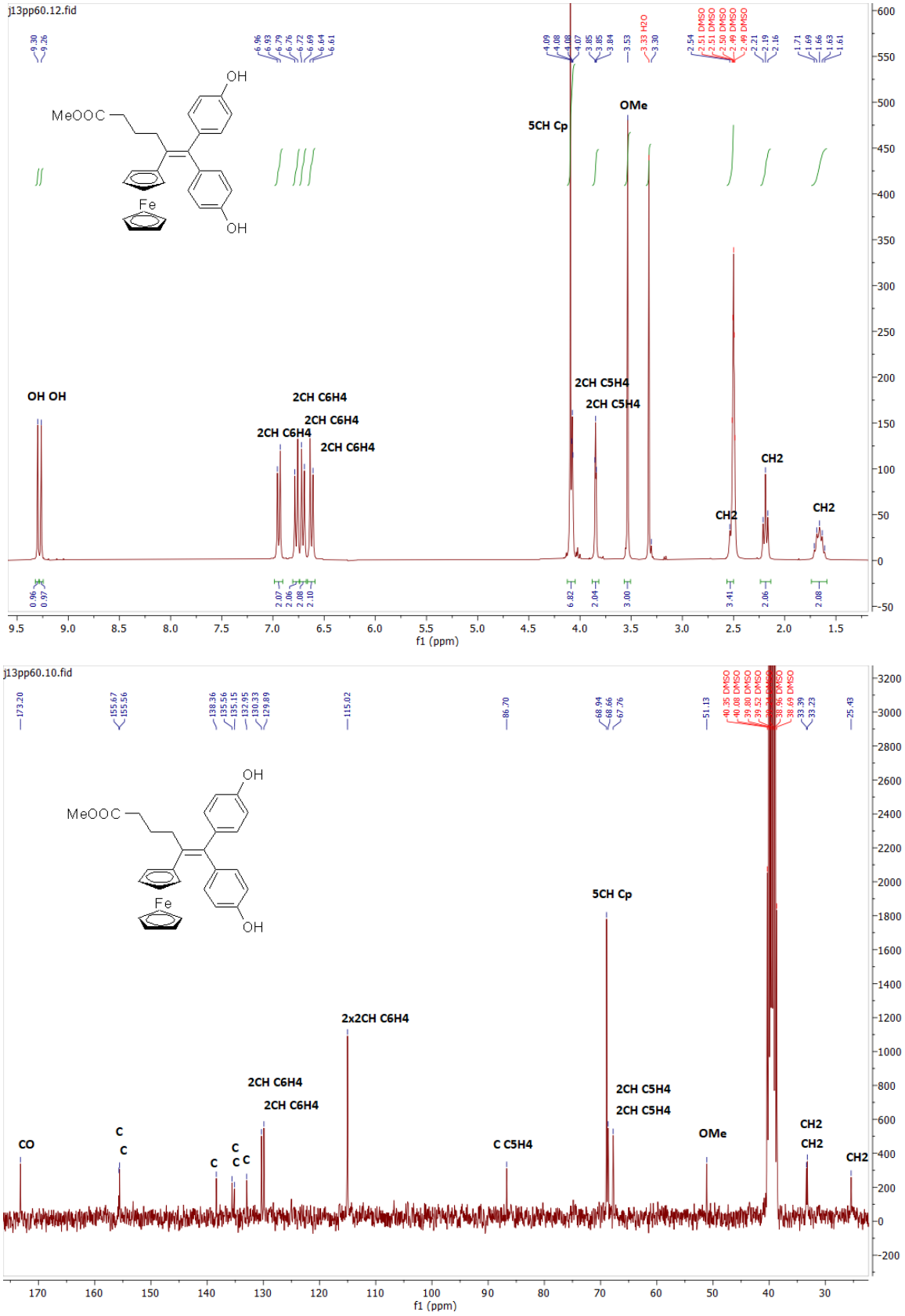

^{1}H and ^{13}C NMR spectrum of compound **7**

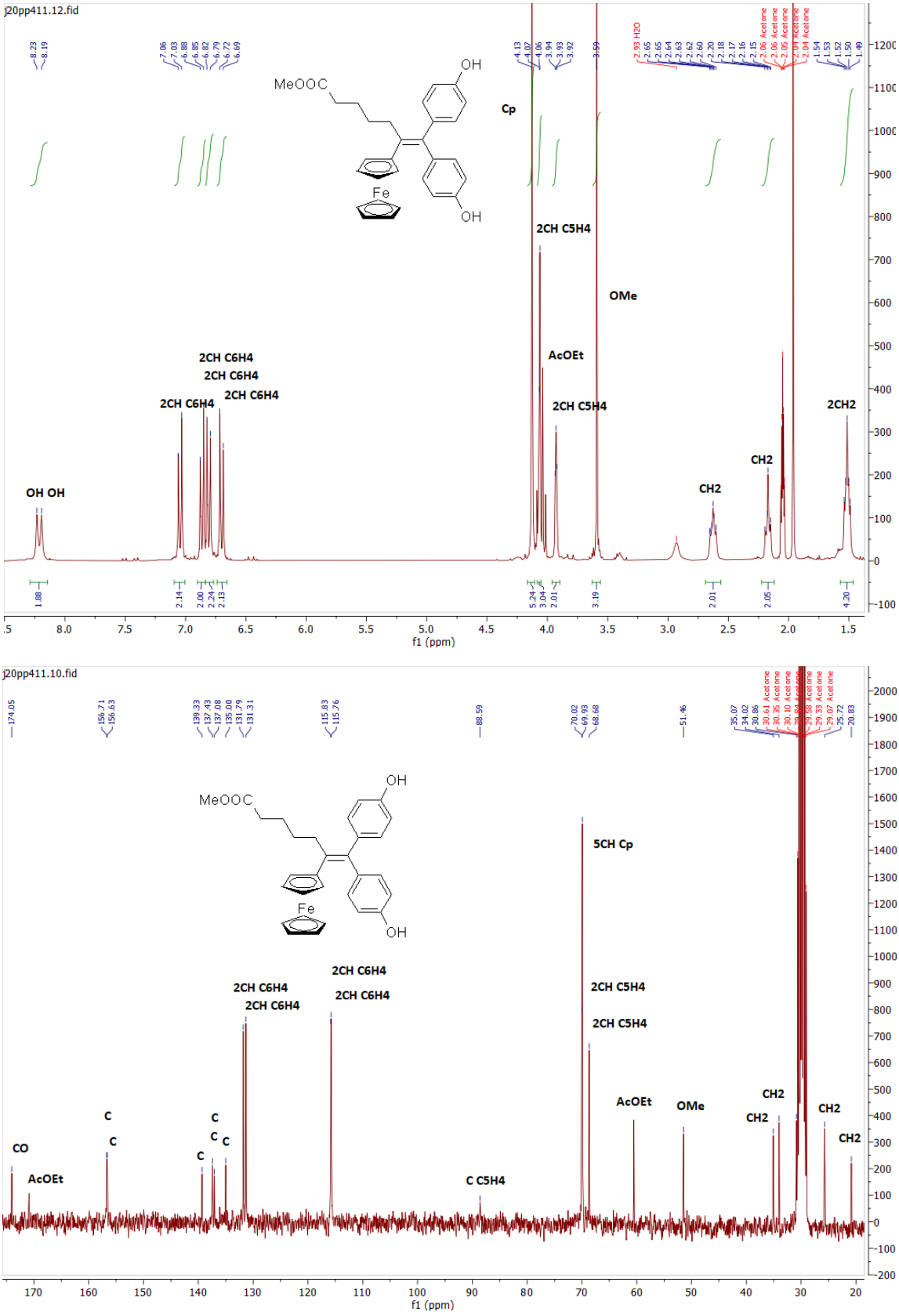

^{1}H and ^{13}C NMR spectrum of compound **8**

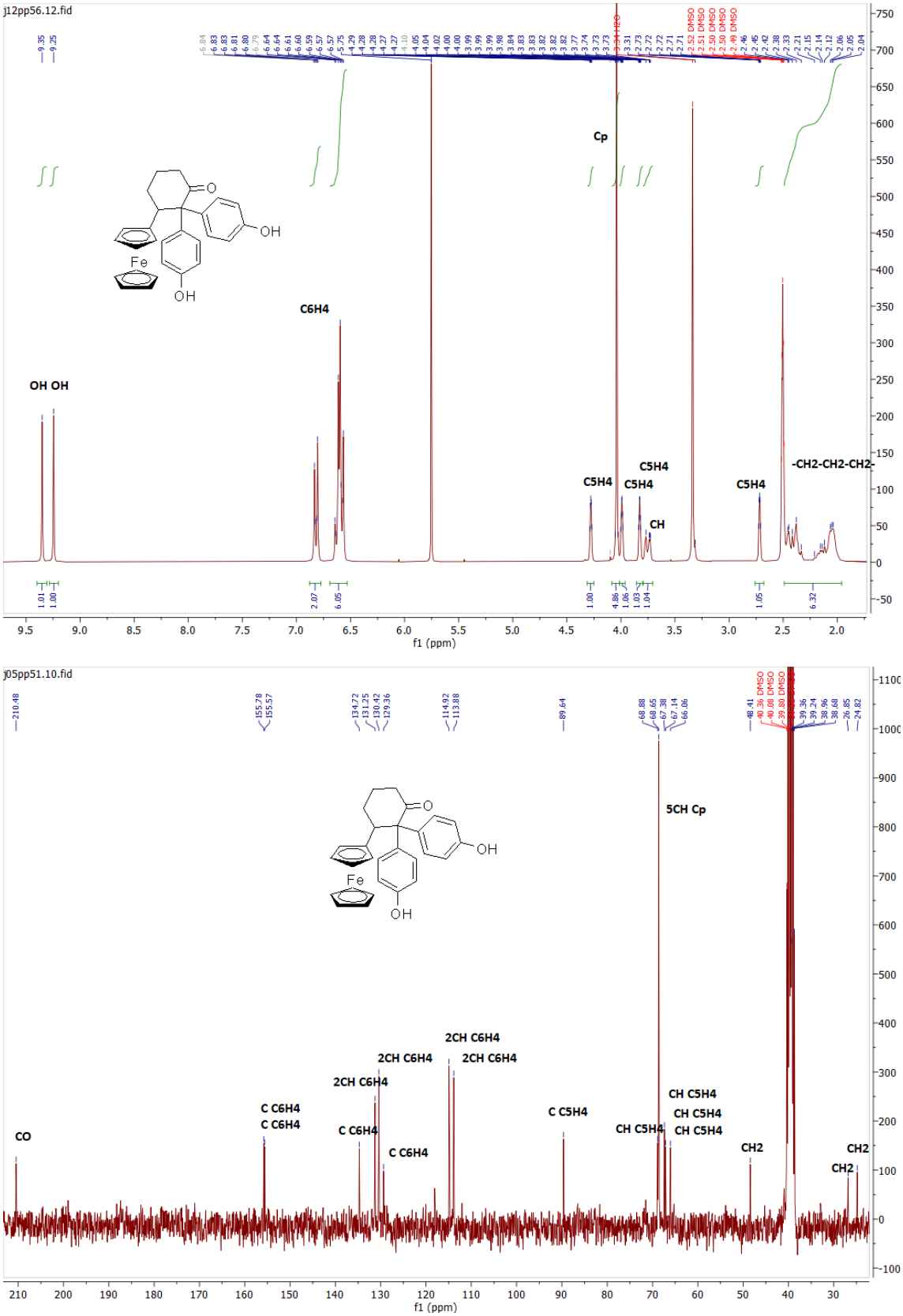

^{1}H and ^{13}C NMR spectrum of compound **9**

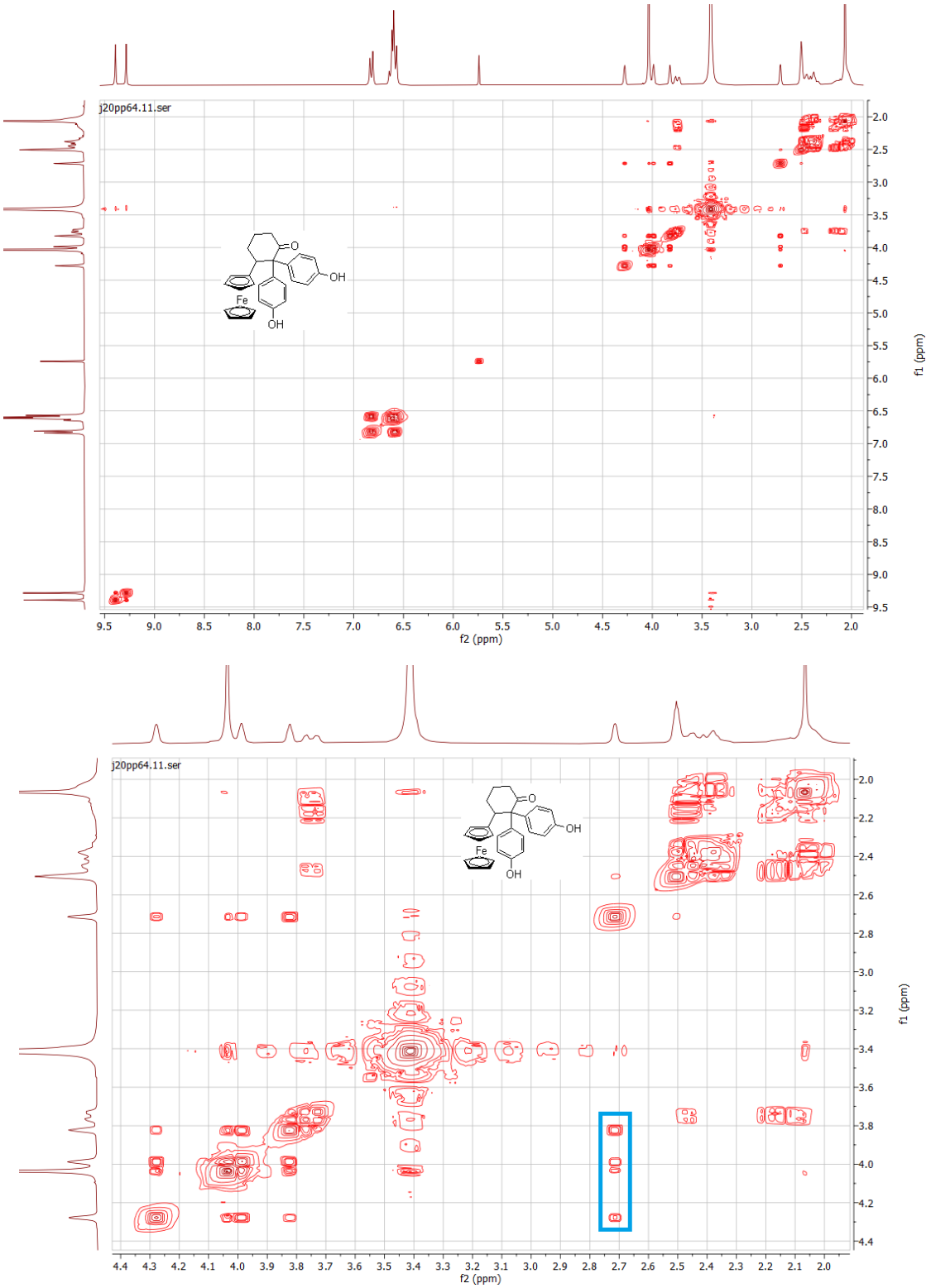

COSY (full and zoom) spectra of compound **9** proving the high shielding of the ferrocenic proton at 2.7 ppm and its coupling with other ferrocenic protons at 3.8 – 4.3 ppm

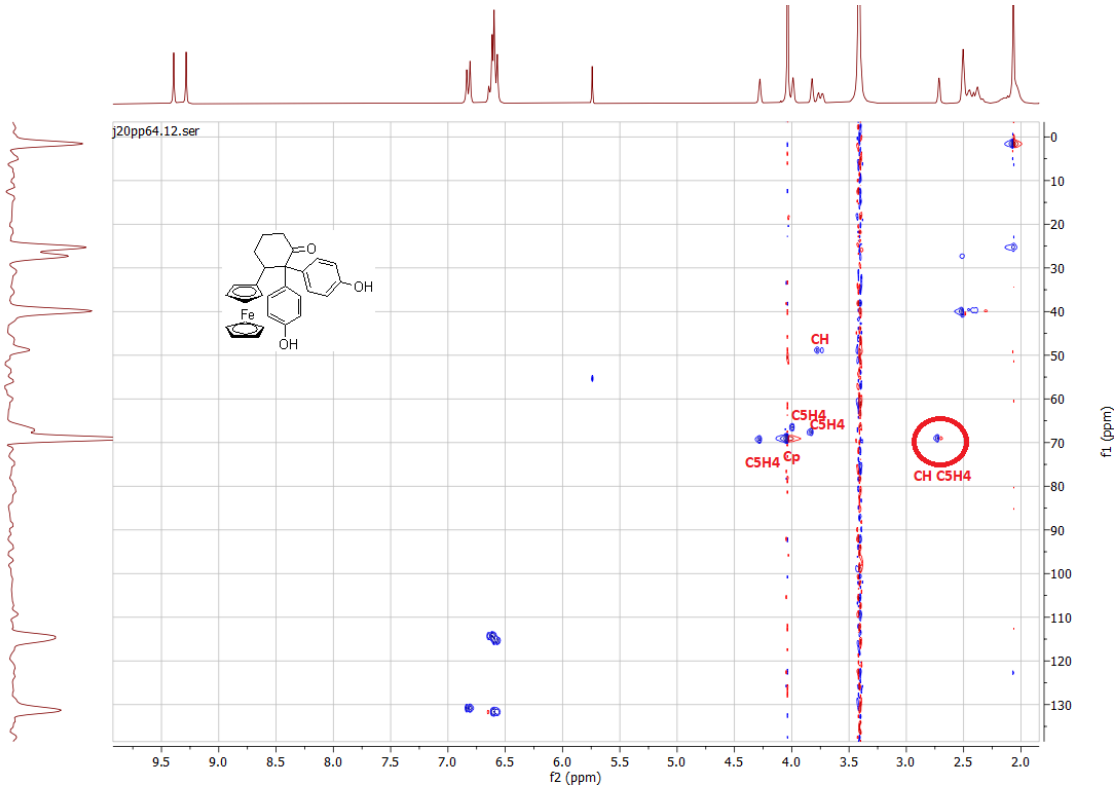

HMQC spectra of compound **9** proving the high shielding of the ferrocenic proton at 2.7 ppm with its corresponding carbon atom

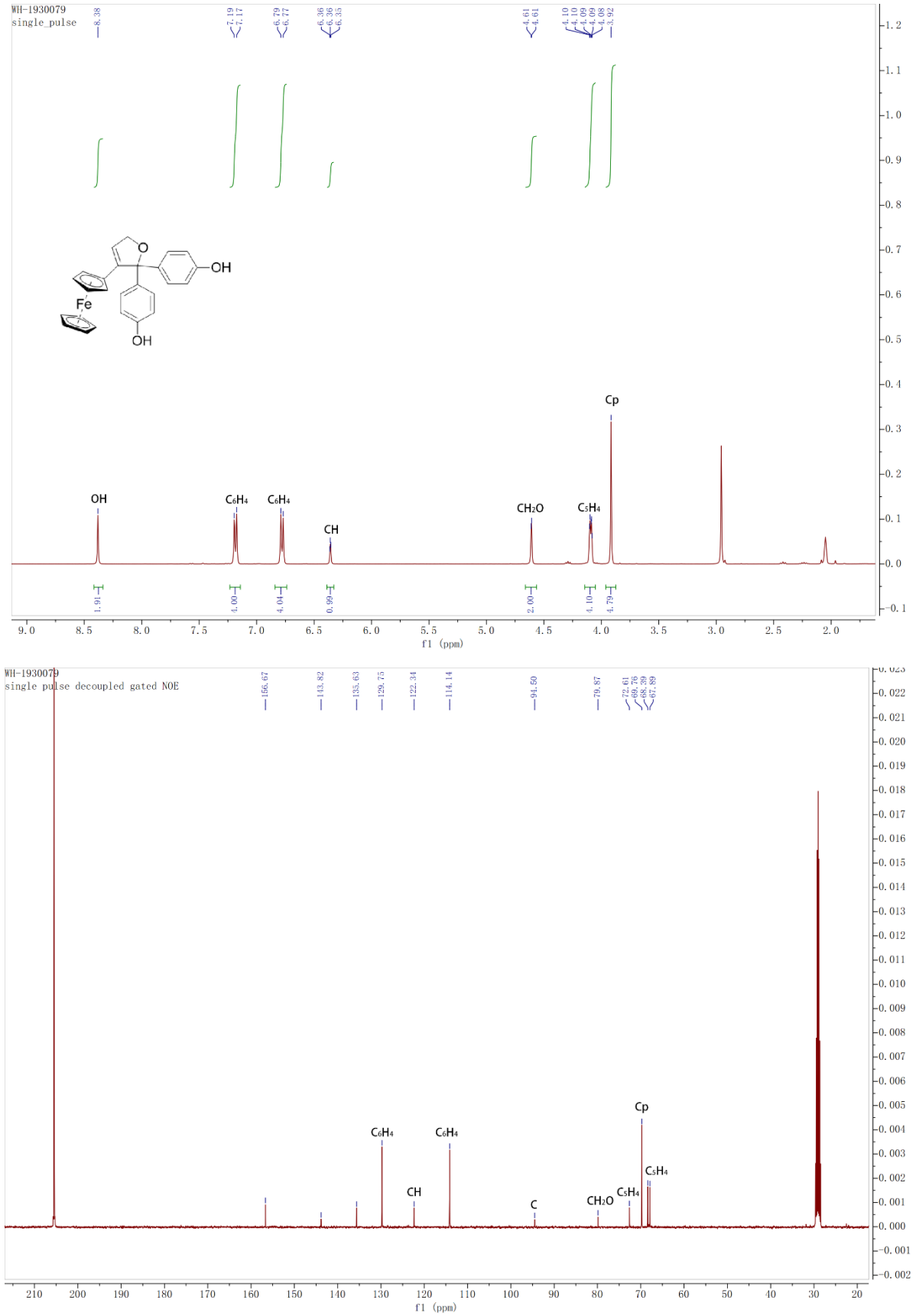

^{1}H and ^{13}C NMR spectrum of compound **3-A**

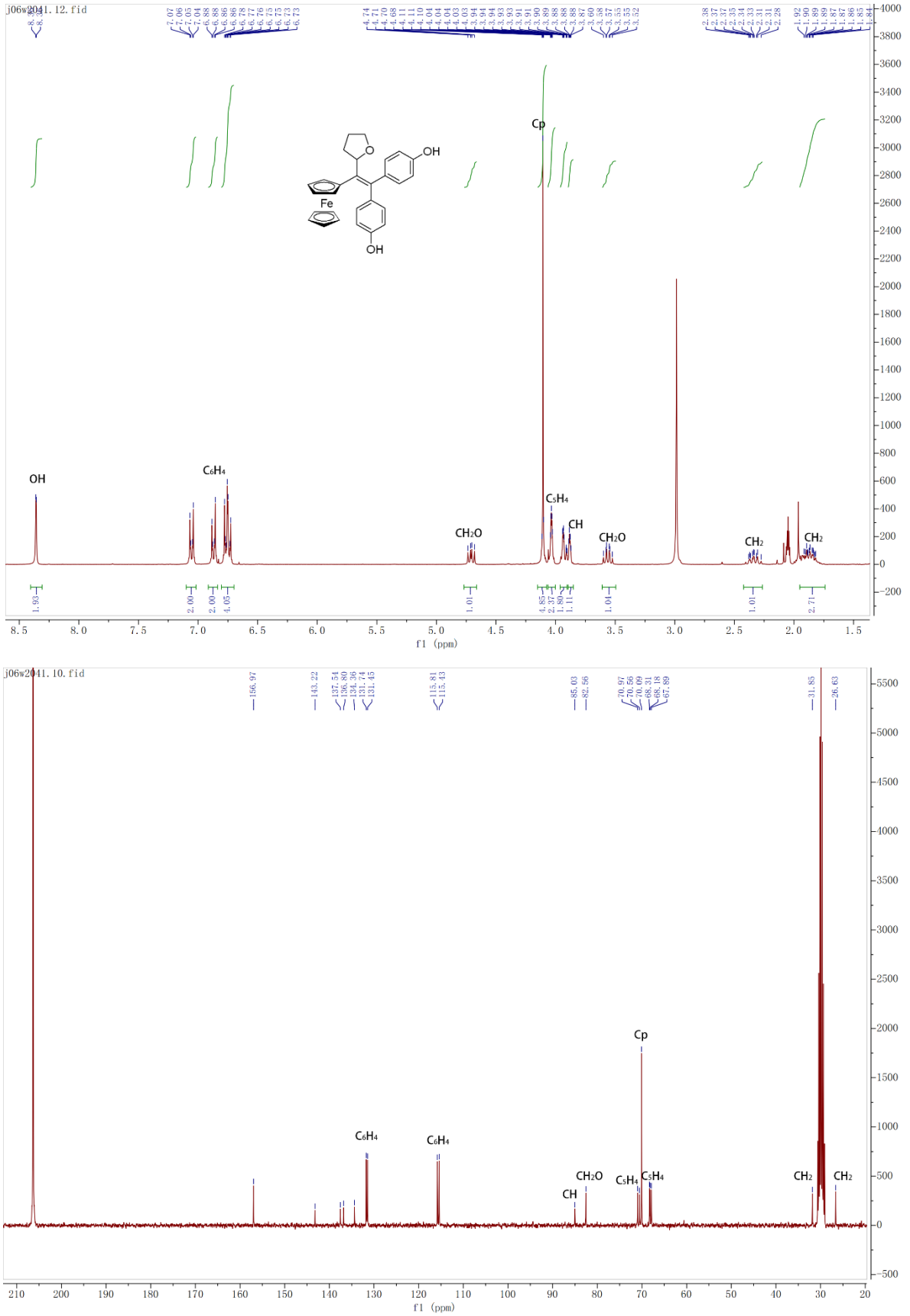

^{1}H and ^{13}C NMR spectrum of compound **4-A**

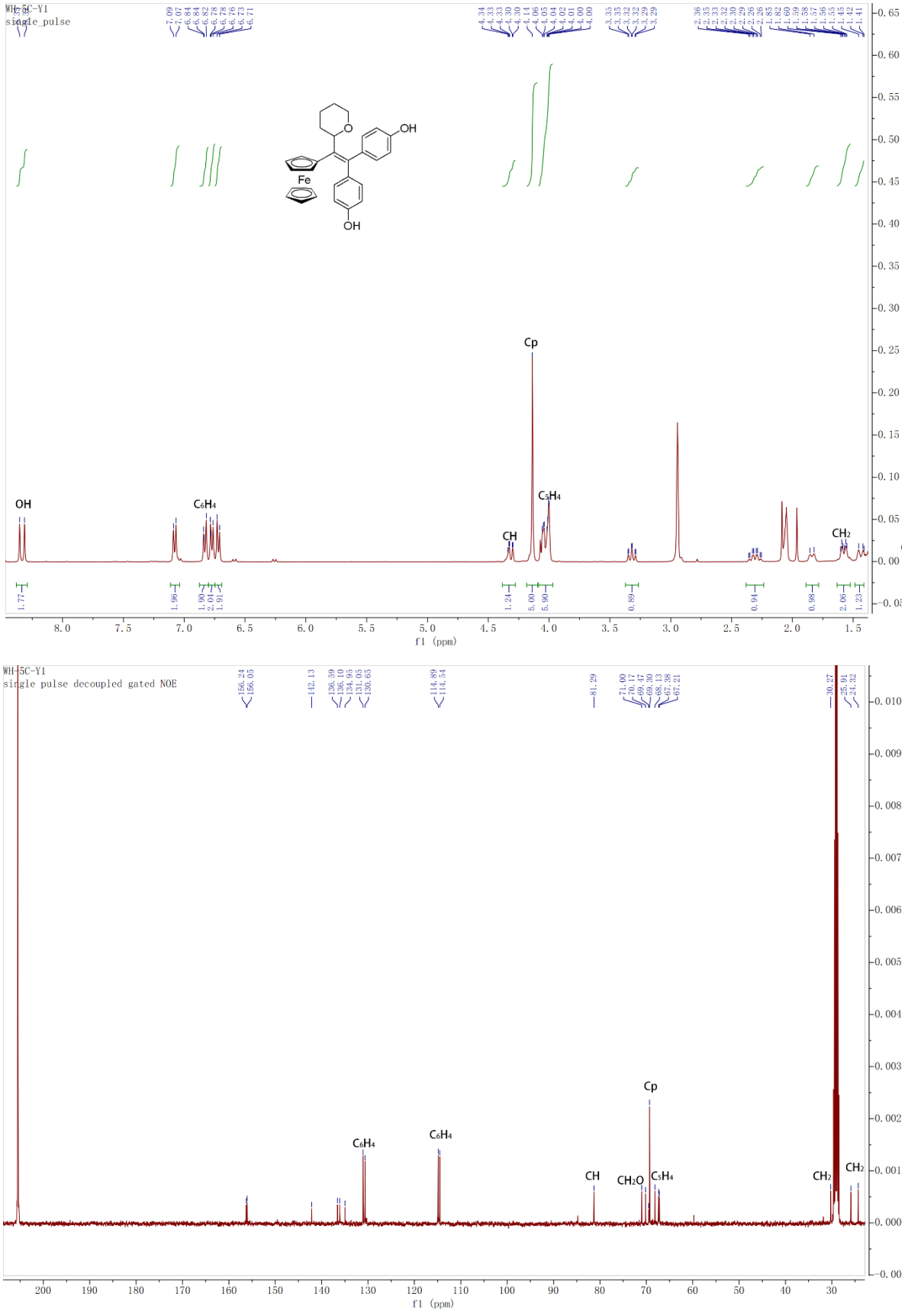

^{1}H and ^{13}C NMR spectrum of compound **5-A**

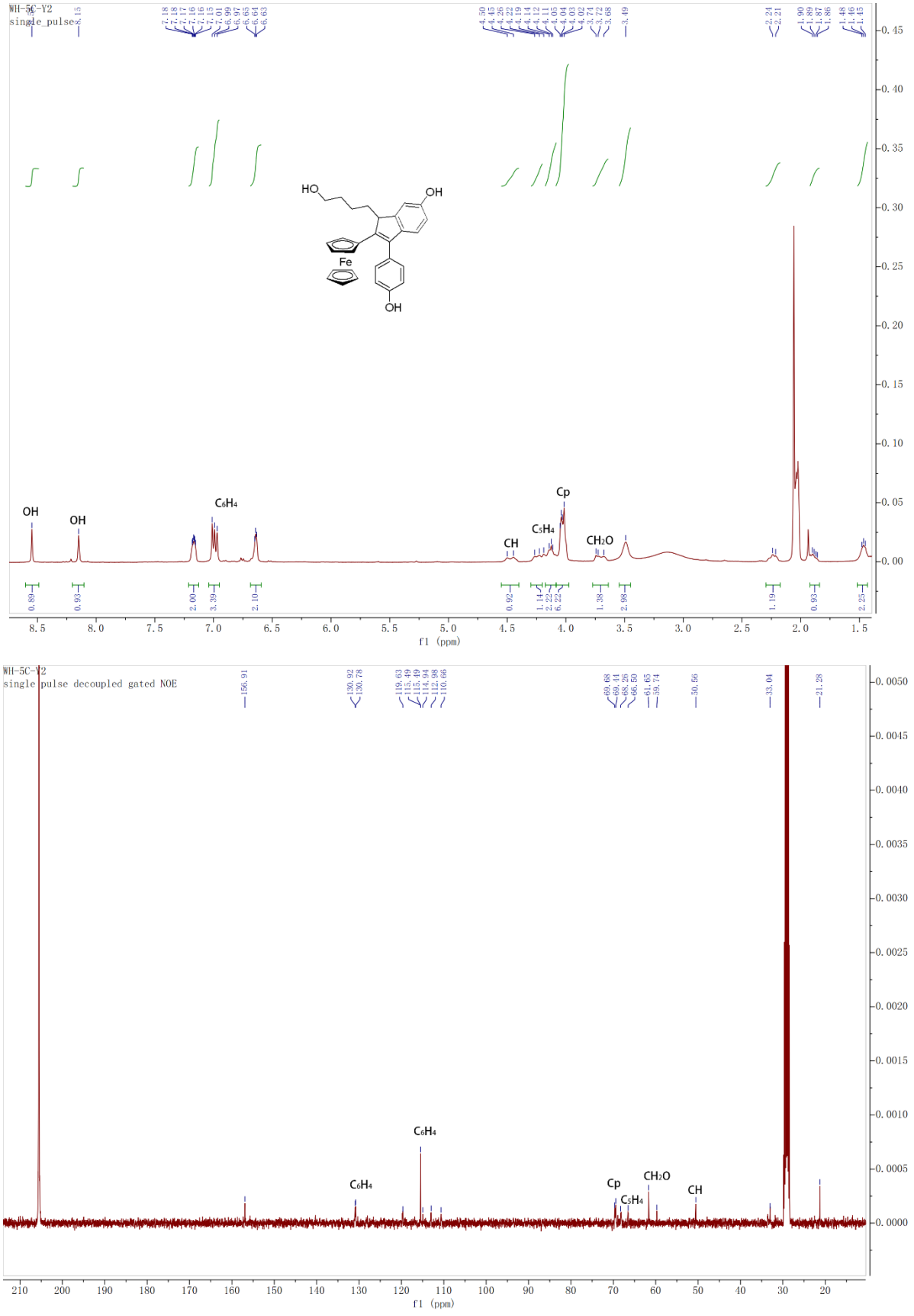

^{1}H and ^{13}C NMR spectrum of compound **5-B**

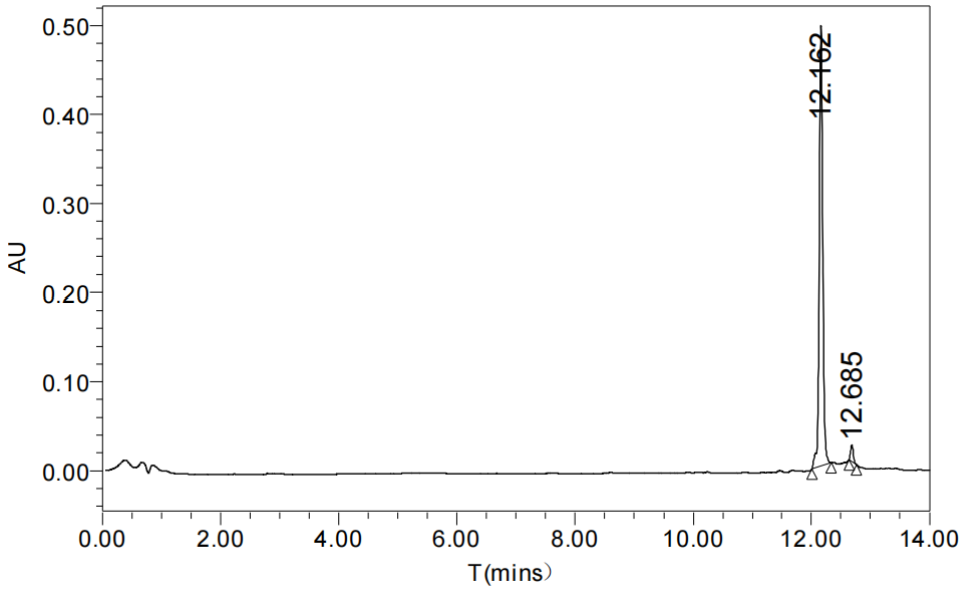

Result

	Ret.Time	Area	Rel.Area(%)
1	12.162	2028457	97.18
2	12.685	58945	2.82

The purity data of the compound **4**

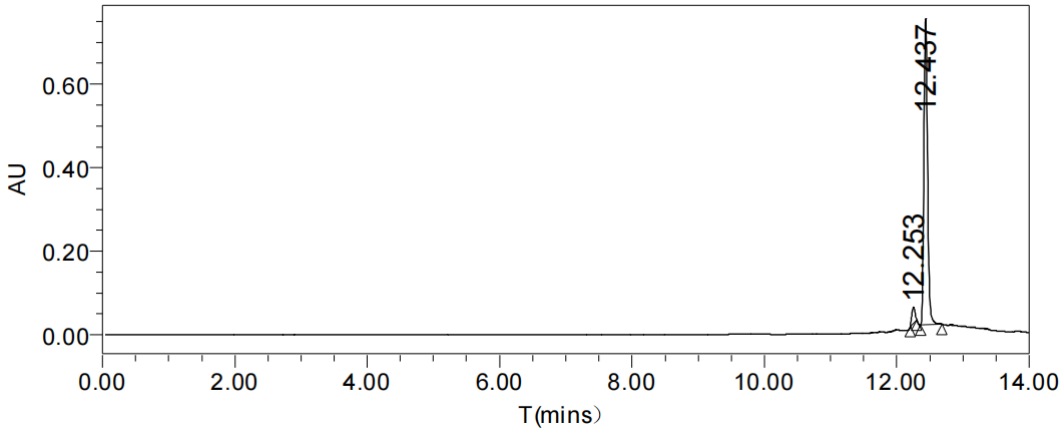

Result

	Ret.Time	Area	Rel.Area(%)
1	12.253	129878	4.45
2	12.437	2789559	95.55

The purity data of the compound **5**

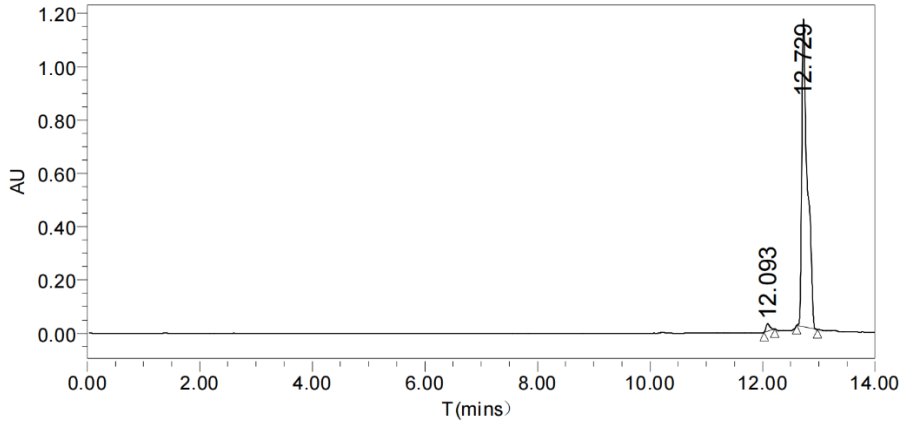

Result

	Ret.Time	Area	Rel.Area(%)
1	12.093	134488	1.67
2	12.729	7938453	98.33

The purity data of the compound **8**

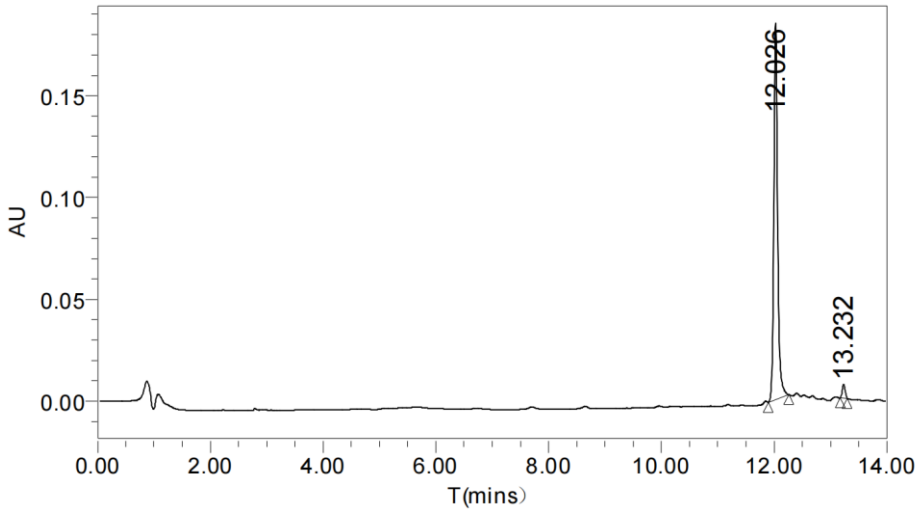

Result

	Ret.Time	Area	Rel.Area(%)
1	12.026	852143	97.26
2	13.232	24043	2.74

The purity data of the compound **3-A**

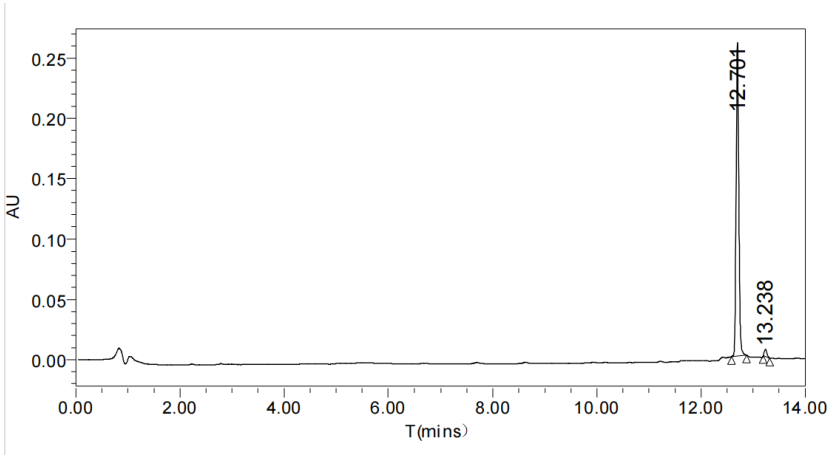

Result

	Ret.Time	Area	Rel.Area(%)
1	12.701	935389	97.98
2	13.238	19329	2.02

The purity data of the compound **4-A**

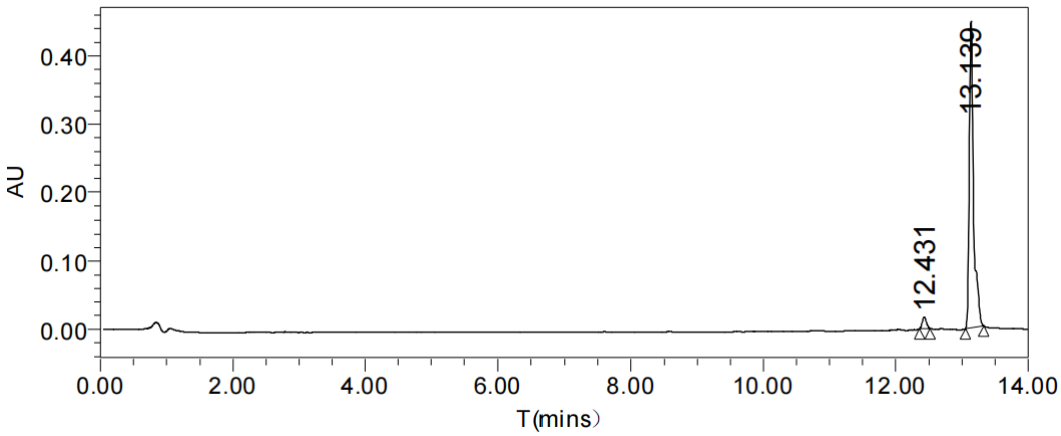

Result

	Ret.Time	Area	Rel.Area(%)
1	12.431	71481	3.47
2	13.139	1990714	96.53

The purity data of the compound **5-A**

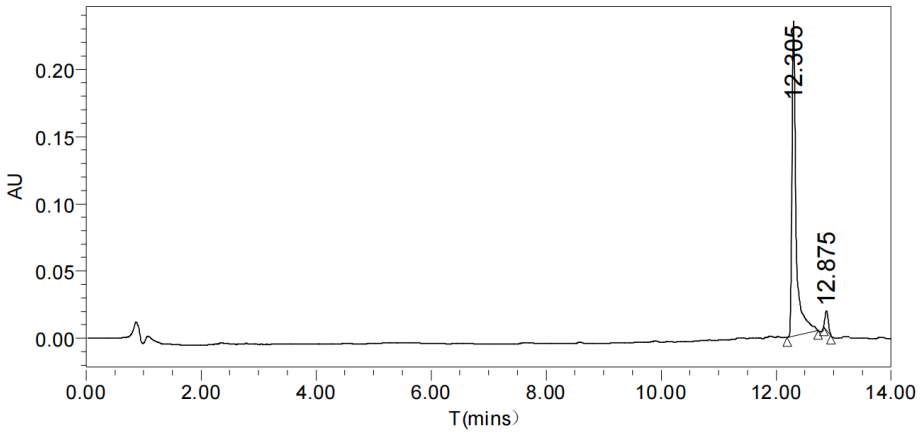

Result

	Ret.Time	Area	Rel.Area(%)
1	12.305	1170397	95.46
2	12.875	55665	4.54

The purity data of the compound **5-B**

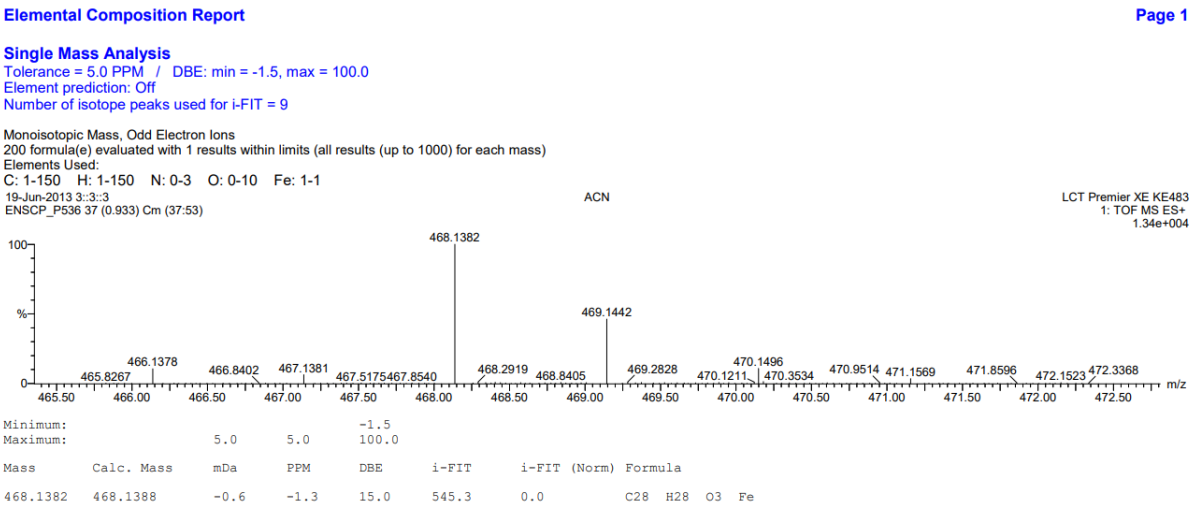

HRMS of compound **4**

Elemental Composition Report **Page 1**

Single Mass Analysis
Tolerance = 5.0 PPM / DBE: min = -1.5, max = 100.0
Element prediction: Off
Number of isotope peaks used for i-FIT = 9

Monoisotopic Mass, Odd Electron Ions
208 formula(e) evaluated with 1 results within limits (all results (up to 1000) for each mass)
Elements Used:
C: 1-150 H: 1-150 N: 0-3 O: 0-10 Fe: 1-1

19-Jun-2013 3::6::1 ACN LCT Premier XE KE483
ENSCP_P537 37 (0.932) Cm (30:40) 1: TOF MS ES+
1.03e+004

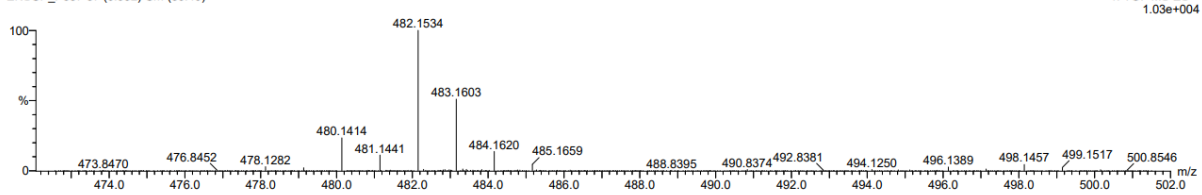

Minimum:				-1.5			
Maximum:		5.0	5.0	100.0			
Mass	Calc. Mass	mDa	PPM	DBE	i-FIT	i-FIT (Norm)	Formula
482.1534	482.1544	-1.0	-2.1	15.0	679.0	0.0	C29 H30 O3 Fe

HRMS of compound **5**

[Mass Spectrum]
Data : PIGEON-P188-CI+NH3--R20 Date : 24-Oct-2007 15:14
Sample: -
Note : -
Inlet : Direct Ion Mode : DCI+
Spectrum Type : Normal Ion CEF-Linear]
RT : 4.80 min Scan# : (41,45)
BP : m/z 497.1432 Int. : 91.93
Output m/z range : 512.4629 to 516.3205 Cut Level : 0.00 %

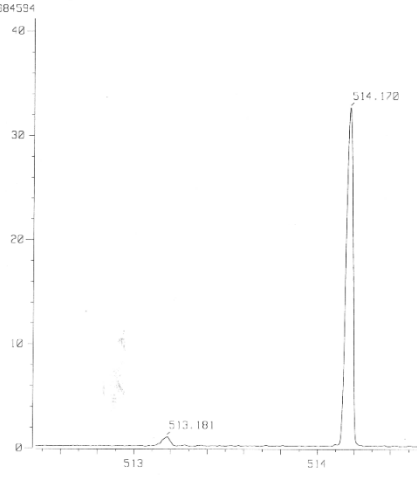

[Elemental Composition]
Data : PIGEON-P188-CI+NH3-HR001 Date : 24-Oct-2007 15:14
Sample: -
Note : -
Inlet : Direct Ion Mode : DCI+
RT : 4.80 min Scan#: (41,45)
Elements : C 29/29, H 50/15, O 4/4, N 1/0, Fe 1/1
Mass Tolerance : 20mmu
Unsaturation (U.S.) : 0.0 - 50.0

Observed m/z	Int%	Err[ppm / mmu]	U.S.	Composition
497.1430	100.0	+3.0 / +1.5	16.0	C 29 H 29 O 4 Fe
498.1455	37.7	-7.7 / -3.8	15.5	C 29 H 30 O 4 Fe
514.1699	32.7	+3.6 / +1.8	15.0	C 29 H 32 O 4 N Fe
515.1703	12.2	-10.8 / -5.5	14.5	C 29 H 33 O 4 N Fe

HRMS of compound **7**

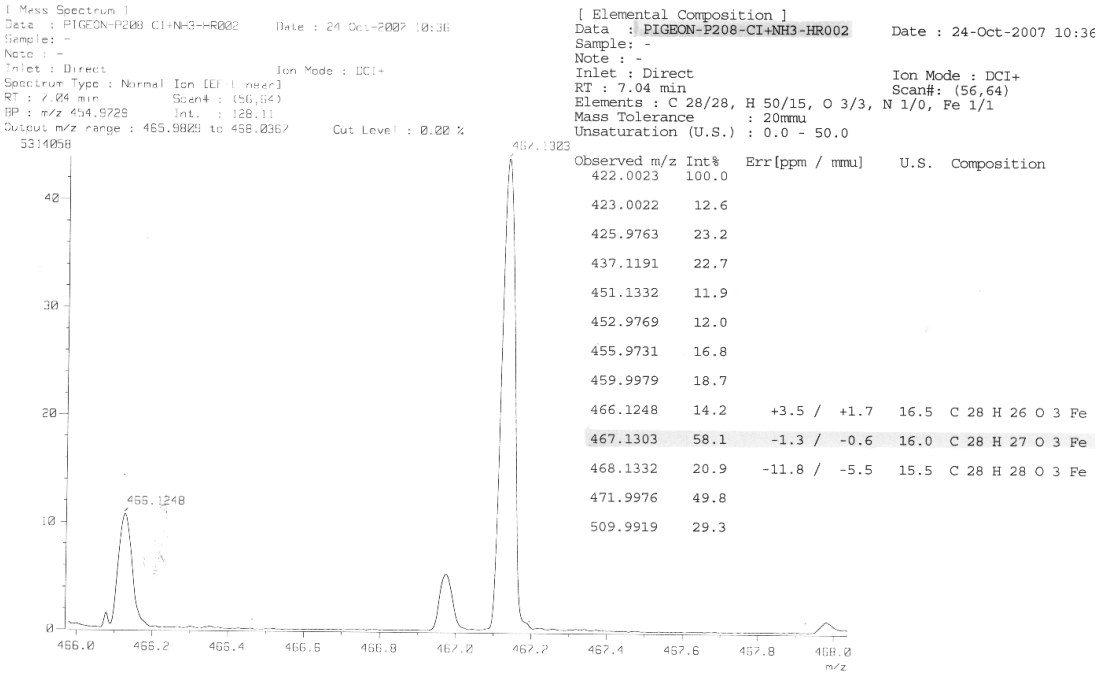

HRMS of compound **9**

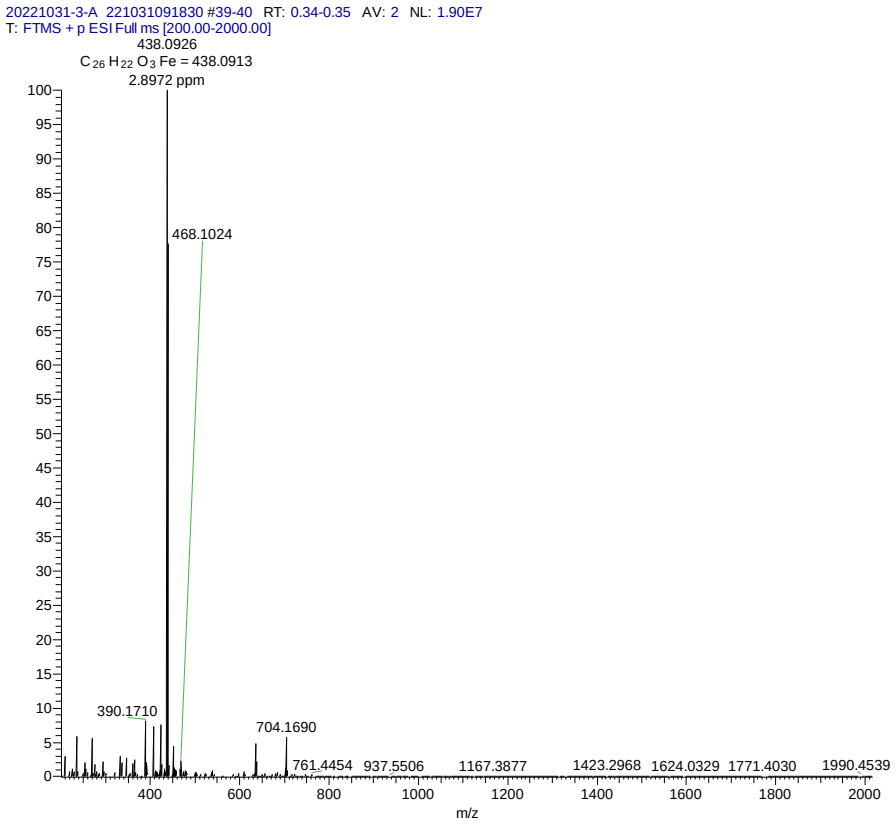

HRMS of the compound **3-A**

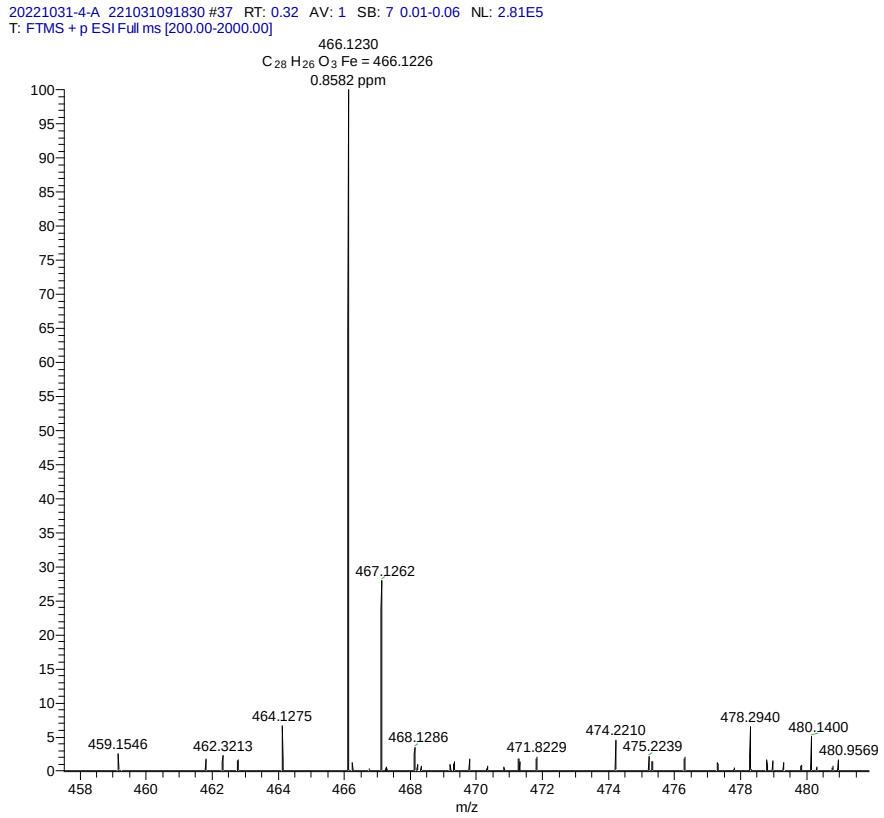

HRMS of the compound **4-A**

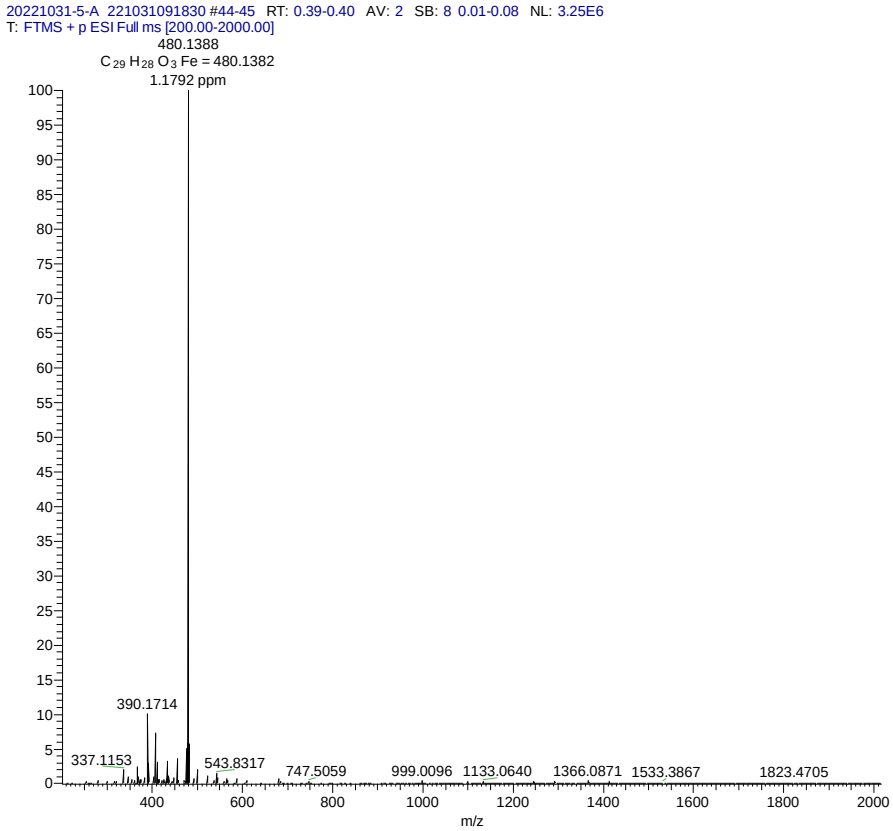

HRMS of the compound **5-A**

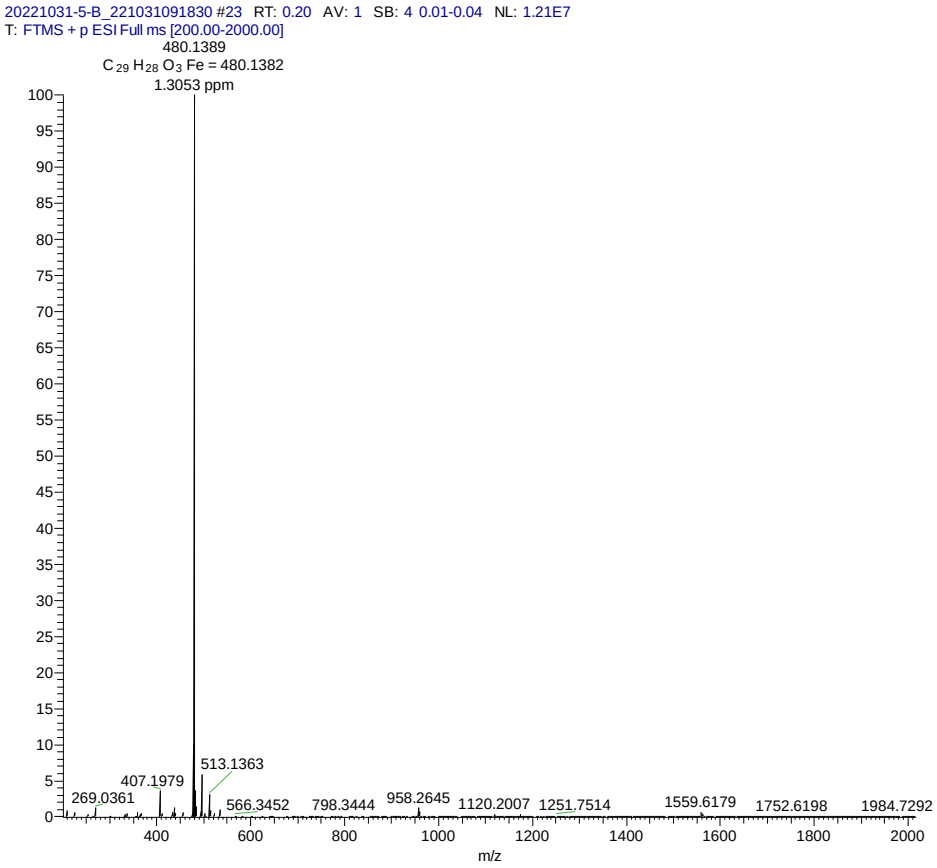

HRMS of the compound **5-B**